DRYING OF GRANULAR CERAMIC FILMS

by

Raymond Chi Hing Chiu

B.S. Chem. Eng. and Mat. Sci. & Eng., U.C. Berkeley
(1987)

SUBMITTED TO THE DEPARTMENT OF
MATERIALS SCIENCE AND ENGINEERING
IN PARTIAL FULFILLMENT OF REQUIREMENTS
FOR THE DEGREE OF

DOCTOR OF PHILOSOPHY
IN CERAMICS ENGINEERING

at the

MASSACHUSETTS INSTITUTE OF TECHNOLOGY

September 1991

Signature of Author.....
Department of Materials Science and Engineering
August 9, 1991

Certified by.....
Michael J. Cima
Associate Professor, Materials Science and Engineering
Thesis Supervisor

Accepted by.....
Linn W. Hobbs
Professor of Materials Science
Chairman, Departmental Committee on Graduate Students

DRYING OF GRANULAR CERAMIC FILMS

Raymond C. Chiu

Submitted to the Department of Material Science and Engineering
on Aug. 9, 1991
in partial fulfillment of the requirements for the degree of
Doctor of Philosophy in Ceramics

ABSTRACT

The drying behavior of binder-free granular ceramic films was studied as a physical model to gain a fundamental understanding of the origin of drying stress and to identify the processing variables affecting the cracking behavior. The green films used in this study were made from 20 vol% aqueous dispersions of α-alumina and α-quartz. The average particle sizes of the alumina powders were 0.2 μm (AKP50), 0.35 μm (AKP30 and Reynolds classified), and 0.68 μm (AKP15). The silica powders had average particles sizes of 0.8 and 1.1 μm. The particulate dispersions were stabilized by adjusting the pH to 3.5 for alumina and 10 for silica. Films were cast onto glass, silicon, teflon, and a pool of mercury to study the effect of substrate constraint.

Direct observations of the drying behavior of the green films were performed using macrophotography, optical microscopy, and environmental scanning electron microscopy. A region of uniform saturation was observed to occur during drying due to the capillary redistribution process. The length scale for this region was estimated to be 1 cm under the external drying conditions used. Thickness variations were observed in the dried green films. This variation can be reduced by lowering the contact angle between the supersaturated slip and the substrate and/or allowing the granular particles to settle prior to drying. Cracks were observed to form in films that were produced above a critical thickness. A film produced on glass from 0.35 μm alumina (AKP30) had a critical cracking thickness (CCT) of 60 μm. Films produced on a pool of mercury had CCT > 2 mm.

The processing variables thought to be important to drying were particle size, liquid surface tension, the drying rate (controlled by the air velocity during convective drying), dispersion stability (pH), and sedimentation time. The significance of these variables was evaluated for the first time using a statistical experimental design methodology. A 2^{5-1} fraction factorial design was used. The effects of the variables on the CCTs for films cast onto glass substrates were used as a measure of the tendency towards cracking. The variables identified to be statistically significant were particle size, dispersion stability, and sedimentation time. Although a higher CCT can

be obtained by floccing the dispersion prior to drying, the dried green density is lowered from 62 to 54 % of theoretical.

Drying stresses were measured *in-situ* by a substrate deflection method using an optical interference technique. For films having dimensions less than 1 x 1 cm^2, uniform saturation can be assumed in the film during drying. The stress which developed at various saturations during drying was determined by simultaneous stress and weight measurements. The maximum stress occurred near 100% saturation and was approximately 2 MPa and 1.1 MPa for films produced from 0.35 μm and 0.68 μm particles, respectively. The maximum stress was also lowered from 2 MPa to 0.9 MPa for films produced from 0.35 μm particles when 0.005 wt% surfactant was added to the slip to lower the liquid surface tension from 72 to 32 dyne/cm. A residual stress was found in films produced from AKP15 and AKP30 alumina powders. These measurements represent the first evidence that the drying stress in a granular ceramic body is due to the capillary tension in the pore liquid.

The shrinkage behavior during drying can be assessed from the relative magnitude of the drying stress and the disjoining forces separating dispersed particles. Since the drying stresses are two orders of magnitude higher than the compliance of a model colloid system, all the shrinkages should occur prior to the time when the pores have emptied.

Estimates of the green strengths of the films were also obtained in this study. The calculations for the fracture resistance values were based on a linear elastic fracture mechanics model. The fracture resistance values are approximately 0.02 and 0.007 MPa-$m^{1/2}$ for films produced from alumina and silica, respectively. This result confirms that the green strength of binder-free granular bodies are derived from the interfacial energies between the granular particles.

Thesis Supervisor: Michael J. Cima
Title: Norton Associate Professor of Ceramics

TABLE OF CONTENTS

List of Figures Page #

List of Tables Page #

Acknowledgments

I would like to thank a few people who have made may study at M.I.T. both productive and memorable. First of all, I like to thank my thesis advisor, Professor Michael Cima, for his supervision and guidance throughout my thesis research. I would also like to thank: Professor Don Sadoway and Professor H. Kent Bowen for their time spent as memebers on my thesis committee, Professor A. Argon and Professor S. Brown for helping me with the questions I had on mechanics and his suggestions for experiments, Dr. Pober for his practical insights on my research, Dr. Wendell Rhine for his expertise in chemistry, John Centorino for his assistance in the laboratory, Mike Frongillo for his help with the TEM, and Jared Wuench for writing the computer program to count the optical fringes.

Many individuals have made the quality of life bearable for me at M.I.T. My sincere thanks go to Dr. Dick Pober for the parties and sailing lessons, Dr. Wendell Rhine for his humor, popcorn, and Bass, John Centorino and Gerry Powers for their ill-delivered but witty jokes during tea time, Lenny Rigione for teaching me his python attitude, Pat Kearny for the buffalo wings, Kip Bishop and Richard Higgins for the chair races, and the guys at the M.I.T. Rugby Football Clubs for two wonderful seasons of fun and bruises. Special thanks also go to Jennifer Lewis, Simone Petersen, Jack Smith, George Karthas, Alan Chao, Ann Hardy, Neville Sonnenberg, Eve Downing, Barabara Layne, and Linda Sayegh for their encouragements during the preparation of this thesis.

Finally, I thank my fiance, Stephanie, and my family for their patience, love, and encouragements.

CHAPTER 1

INTRODUCTION

Most ceramic processes involve the consolidation of raw materials in powder form into a desired green shape followed by sintering to produce the finished component. The structure and property of the component are sensitive to each of the processing steps. In recent years, much of the effort on advance forming technology has involved colloidal powder processes, e.g. pressure filtration, centrifugal casting, injection molding, tape casting, and slip casting. The benefits of processing powder in its dispersed state lie in the ability to manipulate the interparticle forces. Through surfactant and dispersion additions one can gain control over the packing uniformity and green density, which are essential to the subsequent performance of the product. The use of liquid vehicle, however, is not without difficulties. Although required for forming, the liquid must be removed prior to firing, and the drying process often causes problems with dimensional control, segregation, and cracking. The most common approach is to strengthen the greenbody by addition of organic binders which are fugitive and decompose at elevated temperatures. As binders cause other problems, such as carbon contamination [1] and increased cycle-time, it would be beneficial to understand the source of drying defects so as to minimize the need for organic additives.

The recent literature on drying in ceramics primarily concerns the processing of sol-gel bodies. During drying, these bodies undergo large amounts of strain, as much as 80%, which is associated with the excessive capillary stress produced by nanometer-scale porosity. Large strains are not observed during drying of granular bodies composed of micrometer-sized particles. Rather, linear strains of less than 2% are observed in bodies prepared from well dispersed 0.4 μm alumina [2]. Differences between sol-gel bodies and granular bodies are also observed with respect to drying kinetics. Although the drying stress model based on viscoelasticity has been developed in the past years [3], their applicability to granular ceramic bodies is still in question. The purpose of this study, therefore, is to identify the physical mechanisms leading to and the processing variables controlling the defect formation during the drying of binder-free granular bodies.

Scope of Thesis

The objective of this thesis is to identify the physical mechanism leading to shrinkage and the process variables affecting the cracking behavior of granular ceramic green bodies composed of submicrometer particles. The important processing parameters, as will be shown in this work, are particle size and size distribution, interaction potential between particles, green structure, properties of the liquid vehicle, and drying rate. The research is focused at binder-free thick films made from aqueous dispersions of alumina for the following reasons: (1) high purity alumina is commercially available at various sizes and can be readily dispersed in water by adjusting the pH of the dispersion; (2) thick films are easy to

form and, under appropriate conditions, can be dried with a uniform moisture distribution; (3) the constraint film geometry allows the use of an indirect method to monitor the stress developed during drying.

Garino [4] has observed drying cracks when a film was produced above a critical cracking thickness (CCT). CCT was found to be a good qualitative measure of the cracking tendency of films produced from different dispersion formulations. In the first series of experiments, a fractional factorial design methodology was applied to establish a series of experiments to evaluate the cracking tendency of films during drying against several processing variables using CCT as a measure of the response. The variables included in the experimental design study included powder particle size, wet sediment density, interaction potential between granular particles, liquid vehicle surface tension, and drying rate. Films were also produced on substrates of varying constraint (glass, teflon, and mercury).

The second series of experiments involve an in-situ measure of the stress developed in films during drying. Substrate curvature produced by stress in the film during drying was used to indirectly assess the amount of stress developed. The curvature was monitored by an optical interference technique. An analytical balance was also employed to simultaneously measure the weight loss that had occurred. Since a film can be dried without a moisture gradient under appropriate conditions, the simultaneous weight loss and stress measurement allowed the determination of stress at various saturations.

The measured stress was found to be related to the capillary pore pressure.

But a residual stress was found in some of the dried films. Fracture resistances of green films were estimated from the drying stress and the critical cracking thickness based on a relation derived from linear elastic fracture mechanics.

The last series of experiments were dedicated to investigating the origin of the residual stress in the dried films. Various slip formulations were prepared for this purpose. The dried powder surfaces were analyzed using fourier transform infra-red spectroscopy (FTIR), transmission electron microscopy (TEM), and electron spectroscopy for chemical analysis (ESCA). Electrokinetic sonic amplitude (ESA) measurements were also performed to characterize the dispersion stability of the slips.

Thesis Organization

Chapter 2 of this thesis is devoted exclusively to a review of drying literature in porous materials. The internal mechanisms of drying is presented in the first section. The second section deals with the prediction of moisture gradients in drying bodies. The last section describes the various models used to calculate drying stresses in porous bodies which include granulars, clays, and gels.

Critical cracking thickness measurement and qualitative results on the cracking behavior of granular films are described in chapter 3. In chapter 4, the experimental procedure for the *in-situ* stress measurements is described in detail. Fracture resistances of green films were determined and compared. Factors contributing to the strength of granular bodies are also discussed. The

experiments designed to investigate the residual stress in dried granular films are described in Chapter 5. Although the results were inconclusive, residual stress was believed to exist in all the granular films produced. The ones without residual stresses were believed to have cracked on a microscale that was too fine to detect experimentally. Finally, the major conclusions derived from this study and suggestions for future directions are given in chapter 6. References are numbered sequentually by chapter.

References

1. R.J. Higgins, "The Chemistry of Carbon Retention During Non-Oxidative Binder Removal from Ceramic Greenware"; Ph.D. Thesis. Dept. Mat. Sci. Eng., MIT, Oct., 1989.

2. E. Beylier, R.L. Pober, and M.J. Cima, "Centrifugal Casting of Ceramic Components"; pp. 529-36 in Ceramic Powder Science III, Ceramic Transactions, Vol. 12. Edited by G. Messing, S. Hirano, and H. Hausner. American Ceramic Society, Westerville, OH, 1990.

3. G.W. Scherer, "Theory of Drying," *J. Am. Ceram. Soc.* **73** [1] 3-14 (1990).

4. T.A. Garino, "Patterning, Drying, and Sintering of Particle Films on Rigid Substrates"; Ph.D. Thesis. Dept. Mat. Sci. Eng., MIT, March, 1987.

CHAPTER 2

BACKGROUND

2.1 Drying Characteristics

The process of air drying of granular solids under constant external conditions (i.e. temperature, air velocity, and humidity) can typically be observed in three stages. When the rate of weight loss during drying is plotted versus moisture content, a constant rate of drying is first observed. Following the critical moisture content the drying rate falls off rapidly in a linear fashion during the second stage. Finally, the drying rate diminishes in a nonlinear manner with an upward concaving curvature. These three stages are often called the constant rate period, the first and the second falling rate period, respectively. In Figure 2.1, a typical drying curve is shown. In the following sections, the controlling mechanisms which give raise to the occurrence of the three drying stages are discussed.

Constant Rate Period

In the first stage of the drying process, the situation is completely analogous to the evaporation of water from a free surface. The water first

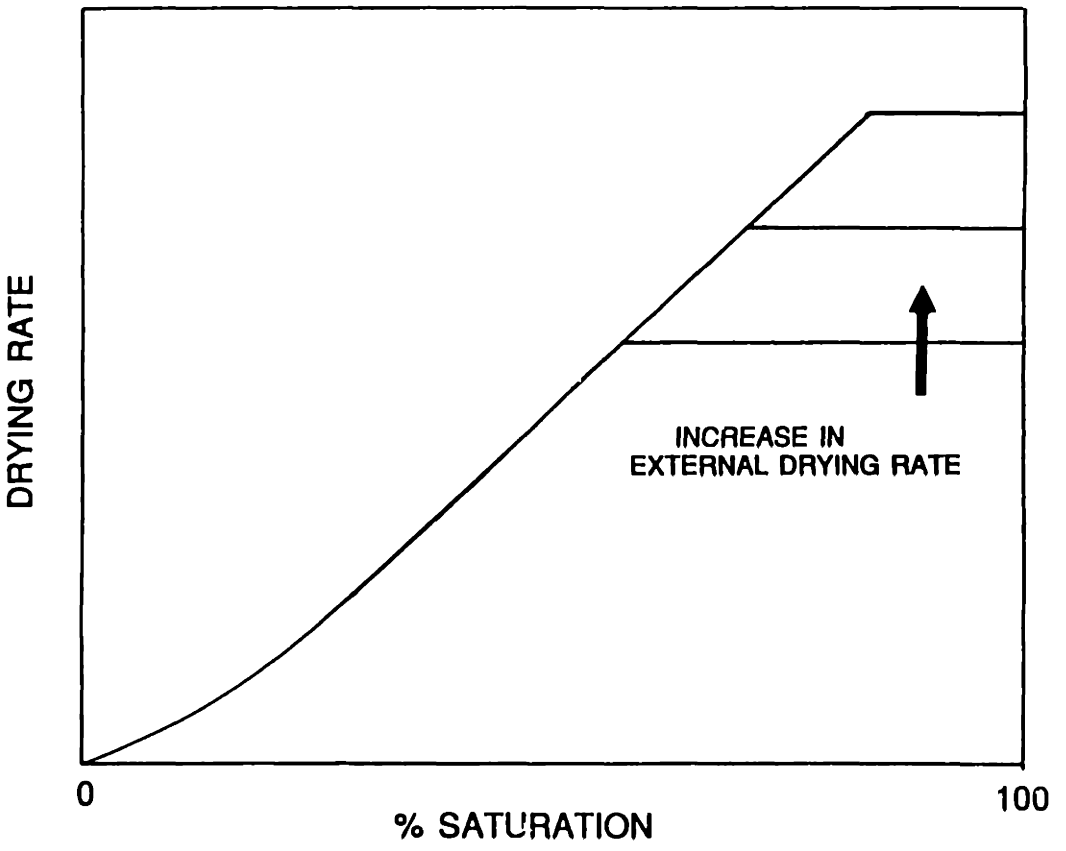

Figure 2.1. Typical drying curve of a granular body.

vaporizes from the surface, diffuses across a stagnant film, and finally transports away by mixing into the ambient air stream. The drying rate is solely dictated by external conditions. The drying rate, W can be expressed by the equation [1]:

$$W = h(P_s - P_a) \qquad \textbf{2.1}$$

where h is the mass transfer coefficient, P_s is the vapor pressure of the water at the liquid surface, and P_a is the partial pressure of water in the air stream. Changes in air velocity affect the thickness of the boundary layer for vapor transport and thus the mass transfer coefficient. As air velocity increases, the boundary layer thickness decreases thereby increasing both the mass transfer coefficient and the drying rate. An increase in the ambient temperature increases P_s, which increases the effective driving force for mass transfer, and increases the drying rate. Conversely, an increase in ambient air humidity increases P_a and decreases the drying rate.

As long as the drying rate is controlled by the diffusion across the boundary layer, the constant rate behavior is observed. Often, the constant rate period prevails well below 100% saturation. To account for this behavior, fluid must be drawn from within the granular solid to the surface as fast as evaporation can take place. This movement is often loosely termed "diffusion." In fact, the experimentally measured moisture distributions of a granular solid during drying do not correspond at all to those predicted by a diffusion model [2]. The diffusion coefficients calculated from experimental data are at least three orders of magnitude greater than those expected for liquids [2]. A more accurate picture for

the liquid transport is explained by viscous flow induced by interfacial forces.

Haines [3,4] had provided a clear picture of moisture movement in a granular solid. Taking the granular bed as composed of uniform nonporous spheres, three states of liquid distribution can exist. In the pendicular state, liquid exists discretely between the sphere contacts. In the funicular state, those isolated liquid lens are connected to one another in a continuous network. Finally, in the capillary state, all the pores are filled with liquid. In Figure 2.2, these situations are illustrated. Beyond the capillary state, further removal of liquid would result in air penetrating into the pores between the particles on the surface. Associated with each of these pores is a capillary suction pressure, P, such that,

$$P = \frac{\phi\gamma}{r\rho g} \qquad 2.2$$

where ϕ is a geometrical packing factor having values between 12.9 (rhombohedral close packing) and 4.82 (cubic packing), γ is the liquid/vapor surface tension, ρ is the liquid density, r is the radius of the spheres, and g is the gravitational acceleration. This pressure can be thought of as a resistance to penetration of the liquid/vapor meniscus by air into a pore during drying.

In the case of a randomly packed network which Haines considered, the surface of the bed has a distribution of pore sizes associated with the local packing behavior. Spheres packed locally in a rhombohedral fashion have smaller pores than those packed locally in a cubic array. Smaller pores have a larger capillary pressure or entry resistance than larger pores. Due to this difference, larger pores

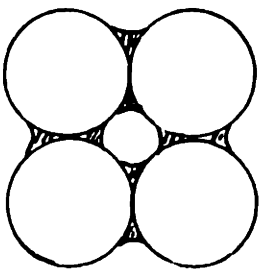

Pendicular

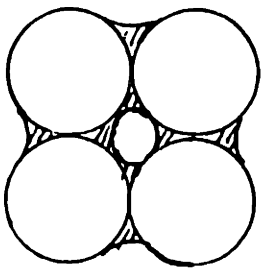

Funicular

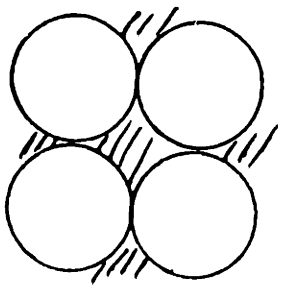

Capillary

Figure 2.2. Three stages of liquid distribution as described by Haines [4].

are opened up first. Since all pores are interconnected inside the granular bed, the liquid is in effect drawn from the larger pores to the smaller pores to provide for surface evaporation. The difference in capillary pressure can determine the height of liquid which a smaller pore can draw from a large one. A simple experiment conducted by Comings *et al.* [5] can help better visualize this behavior. A tapered capillary tube was filled with water and was allowed to evaporate from both ends. The meniscus at the smaller diameter end was found to remain stationary while the meniscus at the larger end receded progressively into the capillary tube. An idealized drawing of capillarity acting during drying in a granular bed is shown in Figure 2.3 [5]. Ceaglske and Hougen [6] provided further experimental evidence demonstrating capillary redistribution in a granular bed. When a layer of fine sand was placed upon a layer of coarse sand and drying was allowed on the fine sand surface, the coarse sand was found to dry faster than the fine sand. This movement of water toward a region of higher saturation was explained by the finer pores and thereby higher capillary pressure of the fine sand. Although this picture of internal moisture movement in a granular solid during drying had generally been accepted, there still exists no simple way to predict a moisture gradient. A more detailed discussion concerning moisture distribution will be covered in a later section.

First Falling Rate Period

In this stage, the rate of liquid transport provided by capillarity is no longer sufficient to supply the external evaporation rate at the surface. Therefore, the

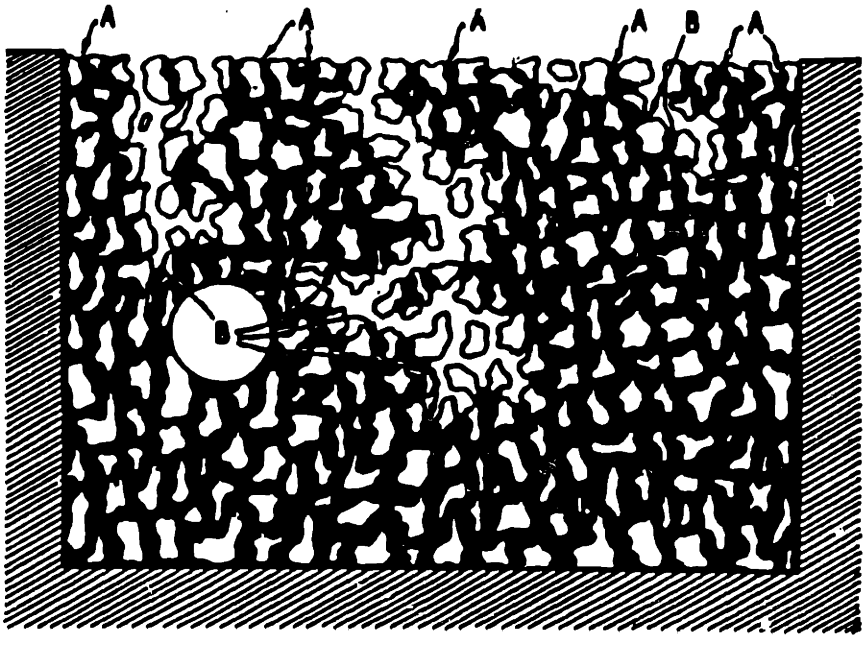

Figure 2.3. **Sherwood's idealized drawing of water movement by capillarity in a granular bed [5].**

drying rate is controlled by the rate at which liquid is wicked to the surface. The decreasing rate has been explained as being due to a decreasing fraction of the surface which is actually wet [6]. The slope of the falling rate depends on the thickness of the granular bed as well as external drying conditions (i.e. temperature, humidity, and air velocity). Such behavior suggests that different transport mechanisms may be contributing to the drying. A complete description of the drying behavior, therefore, requires the simultaneous consideration of all the transport phenomena occurring. This will be discussed in a later section.

Second Falling Rate Period

At this point in drying, the surface of the granular bed is near completely dried; liquid exists only as isolated pockets within the granular bed. The rate controlling step, therefore, is the molecular diffusion of the water vapor through the pores to the external surface. Liquid movement by viscous flow, however, may still be operational in transporting liquid to the vaporization zone within the granular bed.

The latter two drying stages often are not clearly distinguishable. To keep the capillarity driven mechanism operational, a continuous liquid path is required. In some cases, this continuous path of liquid can be disrupted even in the capillary state due to residual air bubbles or dissolved gases in the liquid. In reaction to the capillary pressure, an air bubble in the liquid can expand to a point where interruption of the capillary state can occur. Similarly, dissolved gases can come out of solution to create gas bubbles. In these cases, the rate of drying is limited

by the vaporization process within the pores.

2.2 Moisture Distribution

The prediction of moisture distribution during drying has been pursued by various investigators. Their approaches can be categorized into three groups: diffusion theory [7], capillary flow theory [6], and the application of irreversible thermodynamics [8]. Of these three approaches, only the capillary approach is consistent with the fundamental process that occurs in drying. But this approach requires experimentally determined suction pressure-saturation relationships and can be applied only at the early stages in drying. Whitaker [9] took the rigorous approach by considering the simultaneously occurring transport processes that occur during drying. Although his solutions provided accurate temperature, saturation, and pressure profiles, they required the knowledge of many physical constants and effective transport coefficients, which had to be determined experimentally. More recently, Shaw [10,11] investigated the drying process as an immiscible displacement process and used invasion percolation simulations to investigate moisture distributions in a porous medium. In the following sections, the capillary approach is described in detail, and the elegant experiment and simulations performed by Shaw are also discussed.

Suction Potential

The concept of using suction potential to determine moisture gradients in a

granular solid was first demonstrated by Ceaglske and Hougen [6]. Following a similar experimental method described by Haines, Ceaglske and Hougen measured suction potential versus saturation in a bed of sand (Figure 2.4). Their procedure for determining moisture saturation is outlined below. For a given saturation of S_1 on the surface, the suction is P_1 cm. For a distance l cm below the surface, the saturation can be determined by measuring the value S_2 from the graph at $P_1 - l$ cm. If the thickness is beyond the entry suction pressure, P_A, 100% saturation can be assumed. Similarly, as long as the surface saturation is known and has not reached the funicular state, the saturation at various depths can be determined. In Figure 2.5, the moisture distribution in 2.54 cm thick sand bed as calculated from the above procedure is shown. The average saturation values were obtained by integration. In Figure 2.6, the experimentally determined distribution in the sand bed is shown. In Figure 2.7, the moisture distributions are calculated from diffusion equations for the constant rate period and a constant drying rate. Note that the actual experimental curves are initially convex, but gradually becoming concave which is consistent with the behavior of capillary redistribution but not with the behavior of diffusion.

Pearse *et al.* [12,13] extended Ceaglske and Hougen's work to include the importance of frictional forces resisting the capillary driven flow in fine particle size granular beds. The suction potential P_1 at the surface is therefore, $P_1 = P_2 + h + H$, where P_2 is the suction pressure at depth h, and H is the frictional resistance of the bed over the distance h. H can be estimated using the Kozeny equation. Sample calculations by Pearse *et al.* suggested for particles less than 10

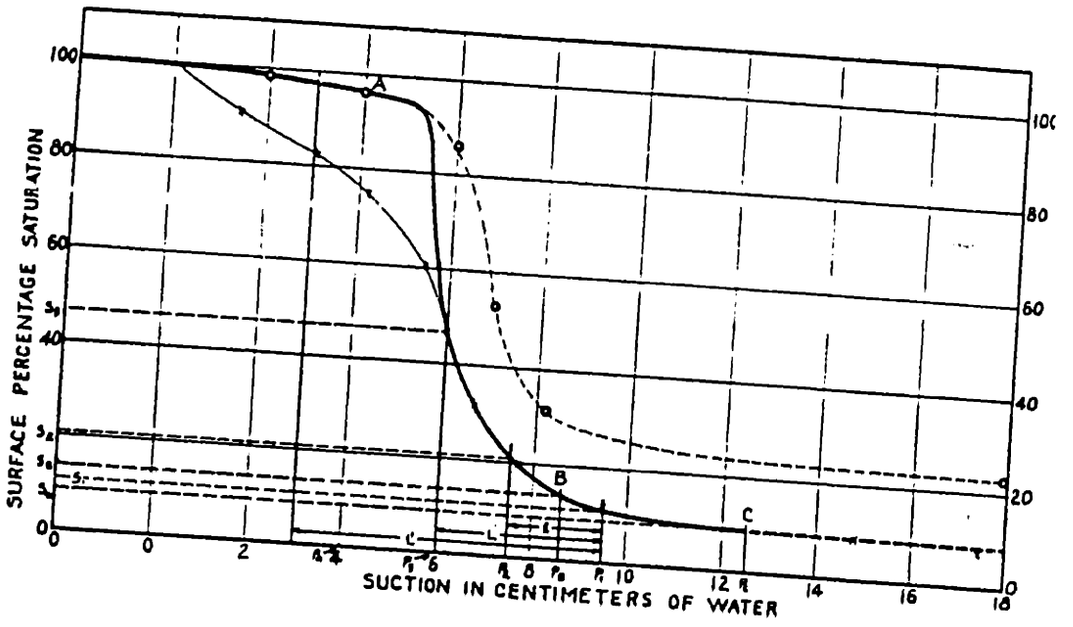

Figure 2.4. **Experimentally determined capillary suction pressure curve for a 5 cm thick sand bed [6].**

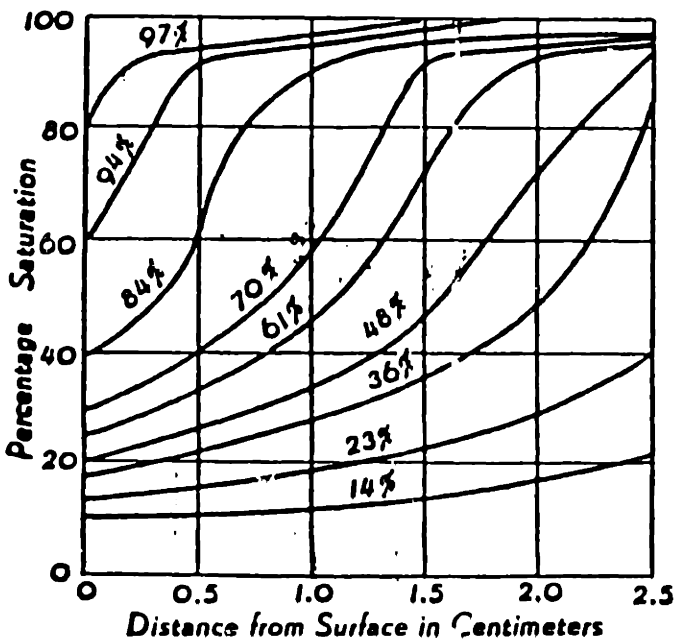

Figure 2.5. **Water distribution in a 2.54 cm thick sand bed calculated from capillary suction pressure [6].**

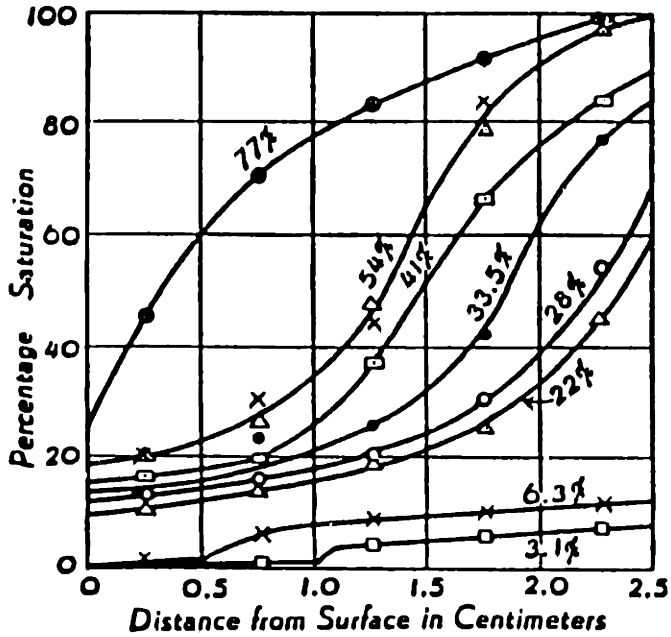

Figure 2.6. **Experimentally determined water distribution in a 2.54 cm sand bed [6].**

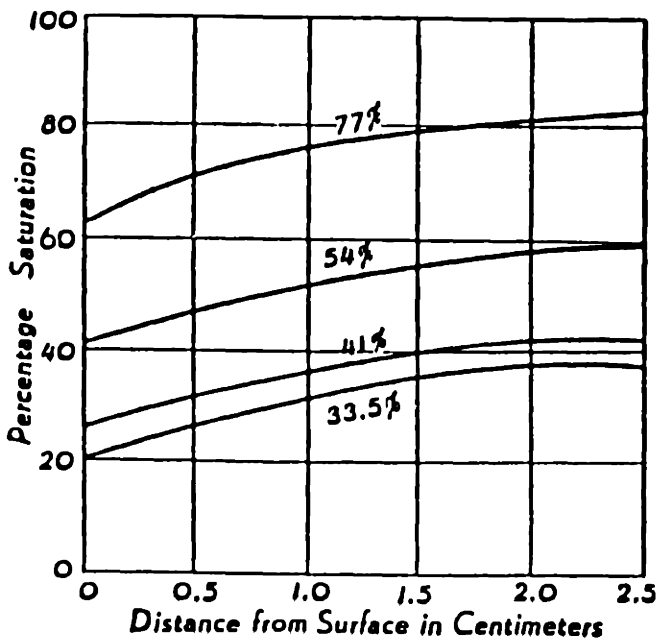

Figure 2.7. Water distribution calculated from diffusion equations for a 2.54 cm thick sand bed [6].

μm in radius, gravitational forces become negligible and frictional forces are of increasing importance. To demonstrate this, they performed drying experiments using glass spheres and silica flours having particle sizes 60, 23.5, 7.5 and 2.5 μm in radius, respectively. For powder beds approximately 5 cm deep, the drying curves are shown in Figure 2.8. Note that the drying rate falls off much earlier for the two fine particle size silica and that for 2.5 μm drops off near 100% saturation. The suction potentials for these powder beds were also measured to determine moisture distributions during drying. In the case of the fine particle size silica, suction did not show as rapid an increase as with coarser material, but there was a gradual build up during which the particle bed shrank uniformly. Thereafter, suction pressure developed rapidly to greater than 900 cm of water and remained substantially constant. The point at which shrinkage ceased also corresponds to the point where the constant rate period ended. Shown in Figure 2.9 is the experimentally determined moisture distribution curves for the fine particle size silica. Note that the shape of the curves actually resembles those derived from a diffusion mechanism.

Clearly, moisture distribution in coarse granular beds can be determined once the suction potential characteristic of that bed is determined. For fine particles, on the order of 1 μm or less which is the range of particle size of interest to ceramic processes, however, suction potential curves are very difficult if not impossible to obtain experimentally. Therefore, in practice, moisture distributions are still predicted analytically from a diffusion behavior approach even though the physical situation is clearly incorrect.

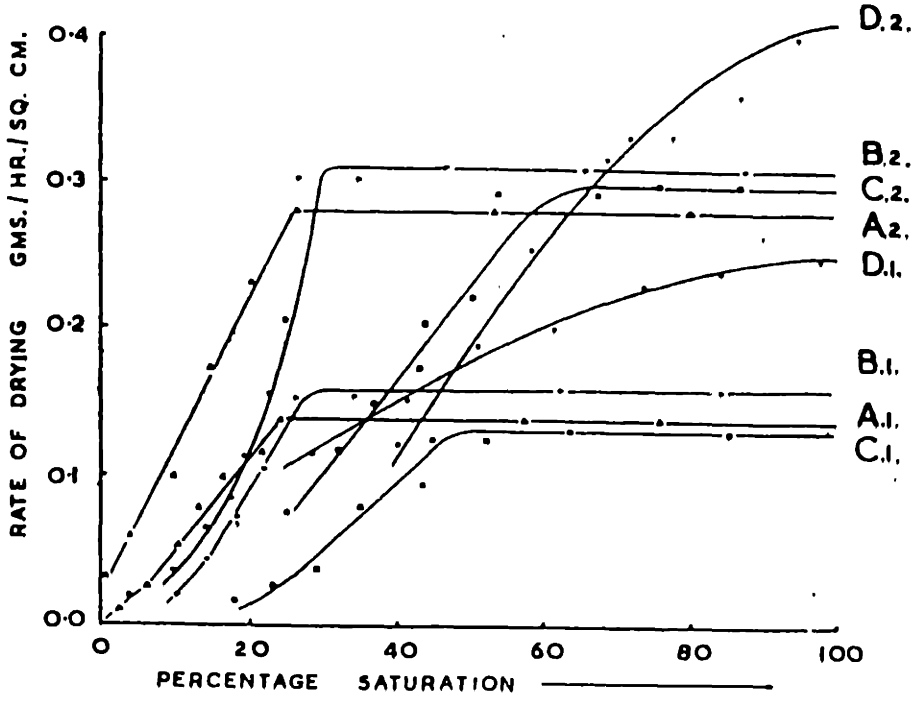

Figure 2.8. Drying curves of various size silica powders: 60 μm (A), 23.5 μm (B), 7.5 μm (C), 2.5 μm (D). The subscripts refer to fast (2) and slow (1) external drying conditions [12].

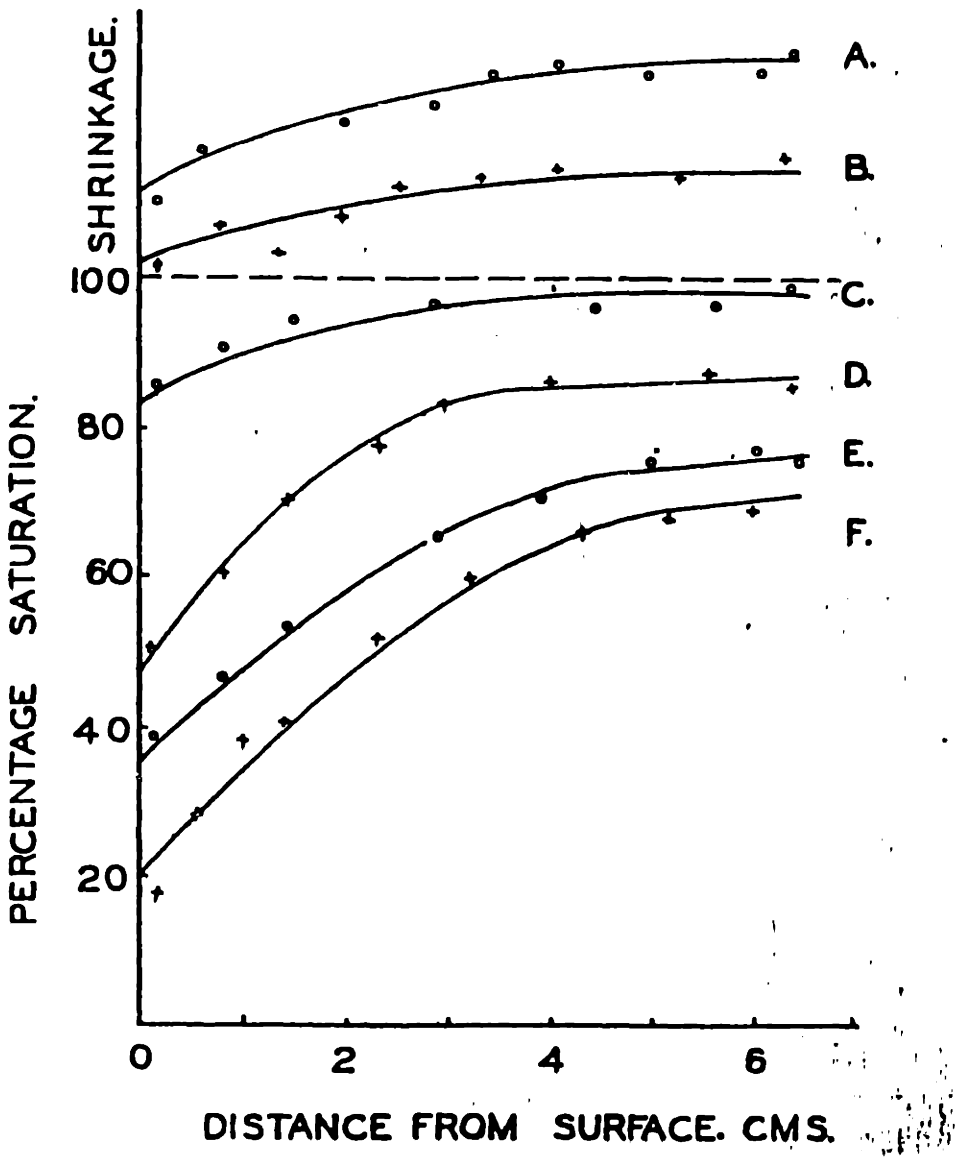

Figure 2.9. Experimentally determined moisture distributions in a 6.5 cm bed of 2.5 μm silica during drying [13].

Invasion Percolation Model

Recently, Shaw [10,11] took a very different approach to the drying problem in granular solids. In his drying model, the water in the porous network is displaced by a less viscous phase, air. Such a problem is called immiscible displacement and is commonly studied in oil recovery processes. The general approach to such model was developed by Wilkinson *et al.* [14,15] as an invasion percolation process.

Similar to conventional percolation [16], a random number representing a probability of occupation is assigned to each site in the immiscible displacement model array. Unlike its parent, in invasion percolation, the sites can only be filled around the edge (2-dimensional) or the surface (3-dimensional) of a single growing cluster. Thus, the cluster grows in the direction of least resistance very similar to the process of pore drainage in drying as described by Haines. This cluster can start from an edge in the 2-D case or from a surface in the 3-D case. Figure 2.10 shows a computer simulation image of a drying front generated by Shaw. Shaw also performed some elegant experiments to visually observe this viscous fingering behavior during drying. By packing silica spheres in water between two pieces of tightly spaced glass and allowing drying to occur only from one edge, he was able to replicate his simulation experimentally. Since silica's index of refraction closely matches that of water, the silica sandwich appears transparent when fully saturated and opaque when drained. In Figure 2.11, images of a real drying experiment are shown.

Figure 2.10. Shaw's 2-D invasion percolation simulation of pore drainage in a granular bed during drying [10].

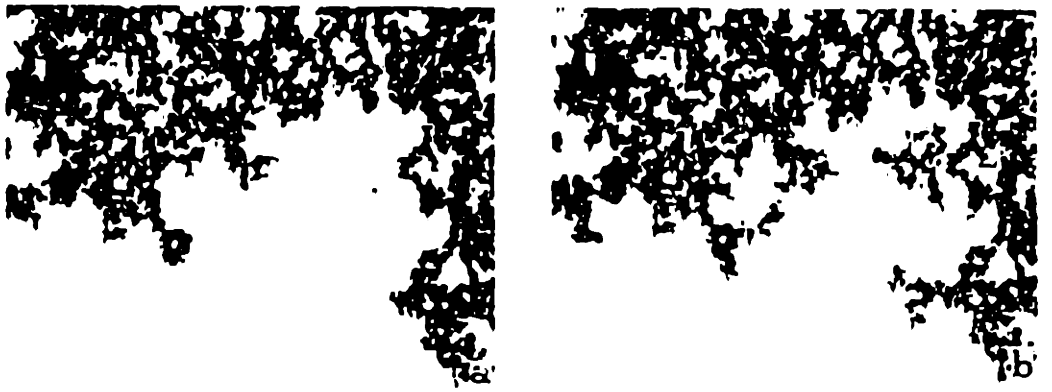

Figure 2.11. Images of drying front observed in the drying of a thin layer of silica spheres. The image on the right was taken approximately 5 sec. after that on the left. The width of each image is 0.5 mm [10].

Shaw suggested that in a partially saturated granular bed, liquid movement can occur by either fluid flow or vapor transport. As long as a continuous path of liquid to the exterior surface exists, the flow mechanism is likely the dominating transport mechanism. A continuum path for fluid flow at as low as 10% saturation can be maintained as the overlapping pendular rings retain particle contacts.

According to Darcy's law, a pressure drop across the drying front to the solid surface is associated with this fluid flow. This correlates to a decrease in the magnitude of the capillary pressure from the exterior surface to the drying front. The effect of a pressure gradient was investigated by Wilkinson. It was treated by biasing the probability that a meniscus can pass through a restriction in the porosity so that the probability was increased as the magnitude of the capillary pressure was increased. Although the calculation of this pressure profile is not done, Shaw assumed a linear pressure gradient across a drying front in his calculations. This resulted in stabilization of the drying front. Figure 2.12 illustrated the effect of applying a gradient. Shaw concluded that a fast drying rate, which would result in a large pressure gradient during drying, can induce an abrupt transition from fully saturated porosity to drained porosity or a steep moisture gradient. If the drying rate were slow, the interface would be more diffuse.

Clearly, the drawback to Shaw's model concerns the significance of a 2-D simulation in describing a real 3-D situation. For example, in the 2-D case, the percolation threshold is much higher than that of a 3-D case. Figure 2.13 [14] illustrates the difference in invader fraction (fraction drained) at the percolation

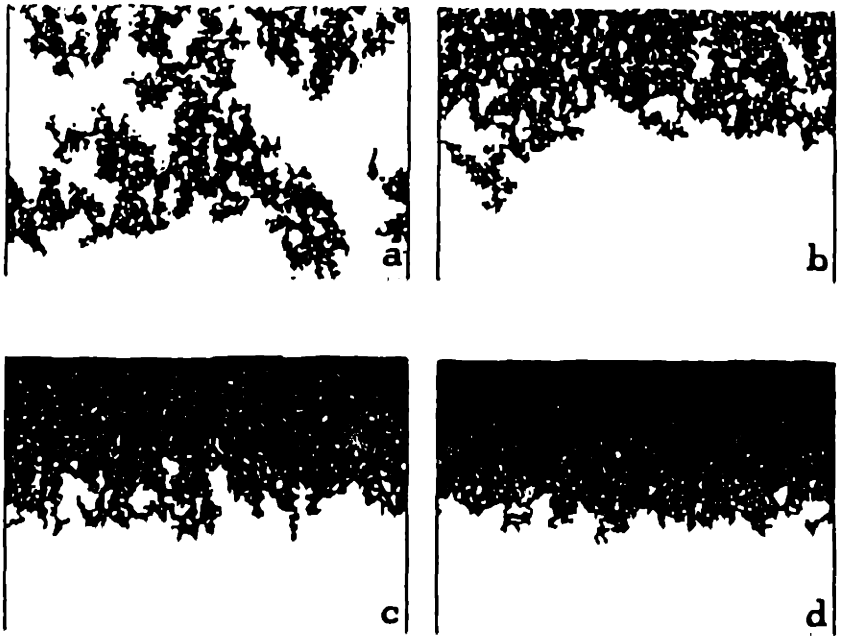

Figure 2.12. The effect of linear pressure gradient on the invasion percolation simulations: (a) no pressure gradient, (b)-(d) increasing pressure gradient [11].

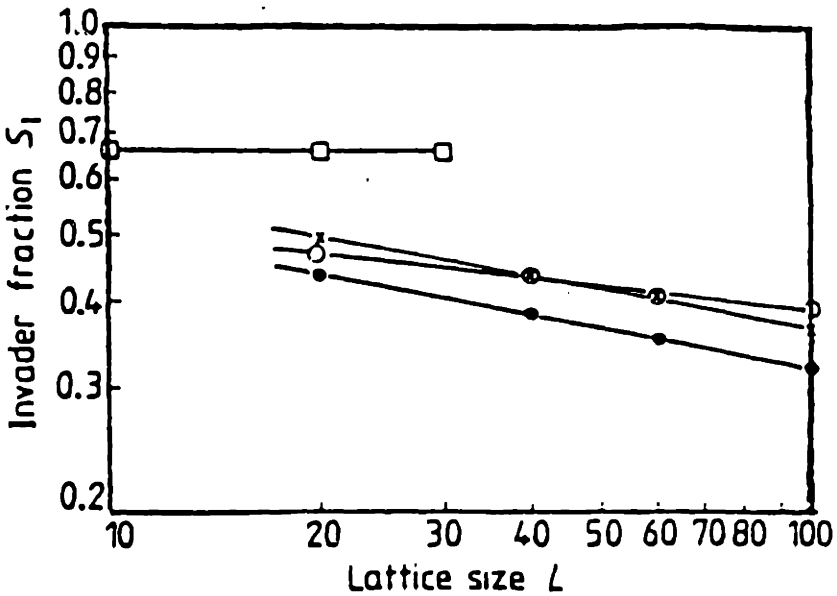

Figure 2.13. The difference in invader fraction or fraction emptied at the percolation threshold between 2-D and 3-D lattices: □, simple cubic; X, honeycomb; ●, square; ○, triangular [14].

threshold as a function of lattice size between a 3-D and 2-D cases. Note that the fraction of drained porosity needed to span the lattice is much lower than that of the 2-D lattices. This also suggests that a stable front is less likely to occur in a 3-D system or that the moisture gradient would be more diffuse than that predicted by a 2-D model. Also, large inhomogeneities in the packing can often occur in real systems which may drastically affect the moisture distribution. As with conventional percolation models, 3-D simulations require massive computation time and are not feasible. Nevertheless, this approach paved a new direction that may be capable of predicting moisture distributions in materials of interest.

2.3 Drying Stress

Shrinkage Behavior

Shrinkage is typically observed during the drying of ceramic green components. For particulate systems such as clay, "inert" granular ceramics, and colloidal gels, the shrinkage is attributed to the elimination of the repulsion layer between dispersed particles in the green state. In clay, the complex chemistry gives rise to repulsive forces from various origins [17,18]: electrostatic, osmotic, and adsorption. Between inert granular ceramic particles, the repulsive force is typically electrostatic and/or steric in nature. In electrostatic repulsion [19], the ceramic particles acquire a net surface charge due to dissociation of surface groups and/or specific adsorption of ions in the electrolyte. In steric repulsion [20], long chain organic amphophilic molecules are absorbed on the particle surface. The

absorption effectively increases the interaction distance between two particles by a thickness approximated by the length of the organic molecule. This repulsive force is entropic in nature; entropy is lost when the surface organic molecules of particles become entangled as in flocculation. When an organic dispersant is used to disperse inert granular particles, both electrostatic and steric repulsive interactions are present and making it difficult to distinguish between the separate contributions. In all cases, the repulsive forces counteract the short range van der Waals attraction between particles. For simple electrostatic repulsion, classical DLVO theory [21] can be used to estimate the magnitude of these forces between the particles as a function of particle separation.

As drying occurs, the capillary redistribution pressure associated with the fine pores will draw liquid from the interior to the surface, thereby drawing the liquid in tension. Associated with the liquid tension is a compressive force around the pore. In effect, the capillary forces act to shrink the green body during drying. If the magnitude of the capillary force was larger than the repulsive forces between dispersed particles, the particles would be forced to touch before pores would empty. This situation is illustrated in Figure 2.14 by Ford [22] for the drying of clay. In fact, a linear shrinkage behavior is typically observed in clay [23] and sol-gel [24] bodies during the constant rate period, and the amount of net shrinkage is proportional to the liquid surface tension [25].

In general, differential shrinkages are responsible for warping and cracking in a green body during drying. The development of this differential stress can be attributed to (1) nonuniform moisture distribution, (2) nonuniform external drying

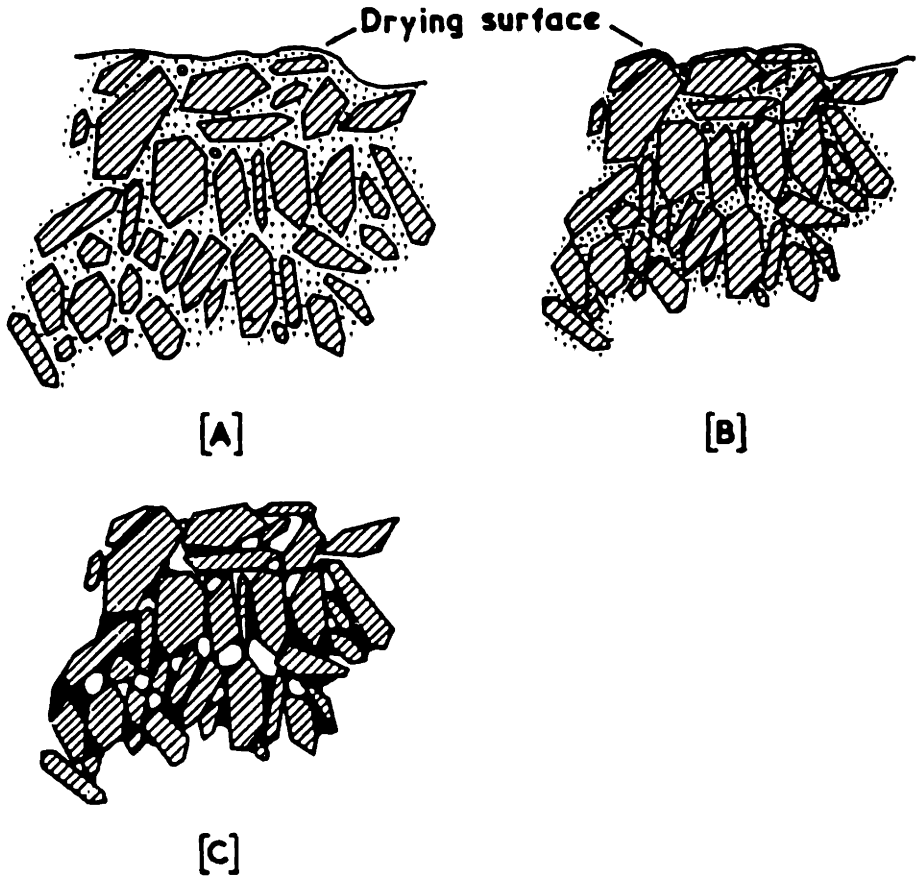

Figure 2.14. Shrinkages between clay particles during drying [22].

conditions, (3) anisotropy in shrinkage due to nonuniform distribution of granular particles or orientation of particles during shaping, and (4) external mechanical constraint [22]. Moisture gradient set up within an article during drying is the most common cause of cracking or warping. To avoid a sharp moisture gradient, the external drying conditions are lowered. In commercial drying operations, large variations in air flow rate, air temperature and humidity around an article can result in nonuniform drying rate around a green shape. Consequently, nonuniform shrinkages along the surface can lead to part failure. In casting nonequiaxial granular particles such as clay, ceramic platlets and whiskers, the forming process may orient the particles in a preferred orientation. Therefore, the shrinkage that occurs in the component may not be isotropic. Nonuniform shrinkage can also occur when the frictional forces at the resting contact surface mechanically restrain that surface to shrink. Before demolding, the casting mold can also provide constraints to shrinkage due to design and/or sticking.

Stress Models

Theoretical prediction of drying stress in a green body typically is approached in a manner analogous to that which thermal stress is developed from a temperature gradient in a material [26-28]. Provided the moisture distribution can be solved analytically, the drying stress can be calculated using a moisture expansion coefficient which has to be determined experimentally. In the drying of clay, Cooper [29] treated internal moisture movement solely as a diffusion process. Therefore, the moisture distribution can be calculated from Fick's laws. Assuming

a constant diffusion coefficient, the steady-state solution to the diffusion equation for a finite slab yields,

$$c(w,t) - \hat{c}(t) = \frac{1}{3}\left(\frac{jw}{D}\right) \qquad 2.3$$

where $c(w,t)$ and $\hat{c}(t)$ are the moisture concentration and the average concentration, respectively, w is the width of the slab, j is the surface evaporation rate, and D is the diffusion coefficient. Applying thermal stress theory, Cooper arrived at an approximate expression relating drying stress to surface evaporation rate, sample geometry, and diffusion coefficient,

$$\frac{\sigma(w,t)}{A(w,t)} \approx \frac{jw}{9D} \qquad 2.4$$

where $A = E/(1-\nu)$, E is the Young's modulus, and ν is Poisson's ratio. Cooper suggested that no chance of cracking can occur for σ/A ratio less than 0.1. Therefore, a safe drying rate can be determined by,

$$j < \frac{D}{W} \qquad 2.5$$

Qualitatively, Cooper's model seemed to be consistent with experimental observations. A thicker slab or a smaller diffusion coefficient requires a slower drying rate to avoid large moisture gradients. However, the basic assumption that liquid diffusion was the predominate moisture movement mechanism was incorrect.

Indeed, Cooper pointed out a discrepancy between the value of diffusion coefficient of water calculated from drying experiments and that of the expected value; the former was two orders of magnitude higher. Closer approximation to the real situation can be obtain from more numerically rigorous approaches using concentration dependent diffusion coefficients or experimentally obtained pressure-saturation relations as described earlier.

Recently, Scherer [30,31] proposed a drying stress model for sol-gel bodies. According to Scherer, a pressure gradient responsible for the capillary flow exerts a compressive stress in the surrounding network causing it to shrink. Therefore, differential strain exists in a drying green body. The stress gradient can be determined from the pressure distribution during drying. This situation is illustrated in Figure 2.15 [31]. If a slab of gel is cut into plates, each slice will shrink a different amount according to the local liquid pressure. But since they are bounded together, they must shrink the same amount. Therefore, the surface is stretched and the interior is compressed. This differential strain is what give rise to a tensile stress which approximately equal to

$$\sigma = P - \langle P \rangle \qquad 2.6$$

where <P> is the average pressure. Therefore, once the pressure gradient is determined, the drying stress can be obtained.

Assuming that all the pores remain filled as in the case during the constant rate period in drying gels, the strain rate can be related to the evaporation rate by conservation of matter:

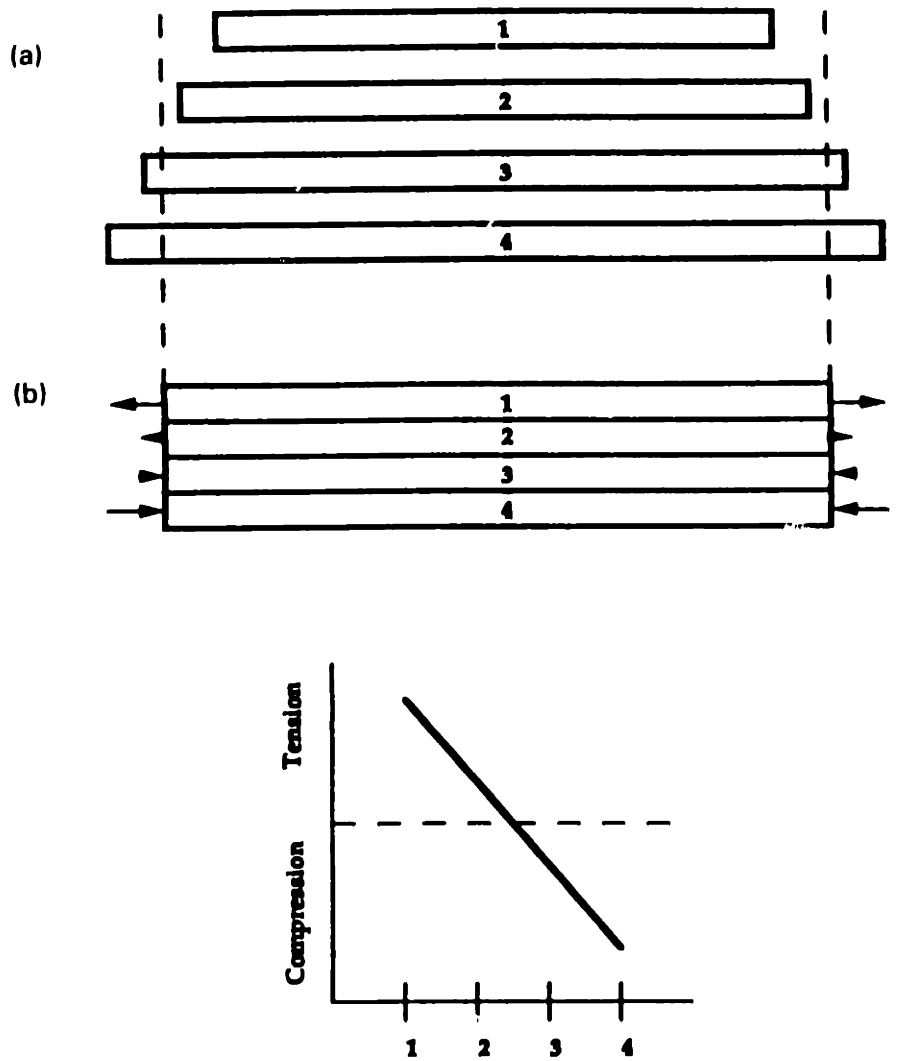

Figure 2.15. Schematic illustration of origin of drying stress [31].

$$\dot{\varepsilon} = -J = -\nabla \cdot \left(\frac{D}{\eta_L} \nabla P \right) \qquad 2.7$$

where ε is the volumetric strain rate, D is the permeability and η_L is the liquid viscosity. The constitutive equation derived by Biot [32,33] for saturated porous media was used to relate the network strain rate to the tension of the liquid. Taking a simple case of an elastic network and imposing a boundary condition of constant evaporation rate V_E at the surface for a plate geometry, Equation 2.7 becomes,

$$\frac{\partial^2 P}{\partial u^2} - \frac{\partial P}{\partial \theta} = (1-\beta_E) \left(\frac{L^2 \eta_L}{D} \right) \left(\frac{\dot{V}_E}{L} \right) \qquad 2.8$$

In this equation, L is the half-thickness of the plate, $u = z/L$ is the coordinate normal to the drying surface, the dimensionless time $\theta = t/\tau$, and

$$\tau \equiv \frac{\beta_E \eta_L L^2}{D K_P} \qquad 2.9$$

The constant β_E is given by

$$\beta_E = \frac{K_P}{K_P + \frac{4}{3} G_P} \qquad 2.10$$

where K_P and G_P are the bulk and shear moduli of the solid network, respectively. Further assuming that shrinkages are negligible in an elastic network and properties are constant, analytical solutions to Equation 2.8 can be obtained. Under mild evaporation rates, typical results are shown in Figure 2.16. In Figure 2.16a, note that the pressure at the surface reaches the maximum capillary tension at the critical point marked by θ_R. Between $\theta_R/3$ and θ_R, the shape of the pressure distribution is approximately constant. Since the drying stress is the difference between the average stress and the local stress (Equation 2.6), the corresponding stress distribution is approximately constant as shown in Figure 2.16b. Beyond the critical point, the pressure distribution vanishes (Figure 2.16e). Accordingly, the stress gradient decays as shown in Figure 2.15f. As shown in Figures 2.16, the maximum stress occurs when the pressure distribution is parabolic, in this case the stress is approximately,

$$\sigma_x = \left(\frac{L\eta_L \dot{V}_E}{2D}\right)\left(\frac{z^2}{L^2} - \frac{1}{3}\right) \qquad \textbf{2.11}$$

The stress is proportional to both the plate thickness and the drying rate and inversely proportional to the permeability. These results are qualitatively consistent since the stress should be increased by those factors which increase the pressure gradient. At extremely fast drying rates, this model predicts that the pressure gradient can be so steep that the liquid near the plate surface reaches the maximum while the bulk of liquid pressure is still zero. Therefore, the stress at

the plate surface is approximately equal to the capillary tension under extreme conditions. One has to recall that the results derived by Scherer here only apply when the pores remain filled and the mechanical properties remain constant. As soon as the pores start to empty, the permeability will vary. Therefore, while Scherer's model can provide quantitative results, its use is limited by the many unknown physical and mechanical property of the porous medium.

In summary, the existing models used to estimate drying stresses in porous granular bodies vary in complexity. While the simple ones are physically inaccurate and are applicable only to a limited range of the drying process, the comprehensive ones requires the knowledge of many physical constants associated with the porous medium which are unavailable. Commercially, these properties are determined empirically for the specific porous material and drying process of interest. Furthermore, unlike the drying of clay and sol-gel bodies where large amounts of shrinkages are observed, only a small amount of shrinkage, on the order of 1%, is observed during drying of granular ceramic bodies composed of submicrometer size particles. Therefore, it is not clear whether the existing drying stress models are applicable.

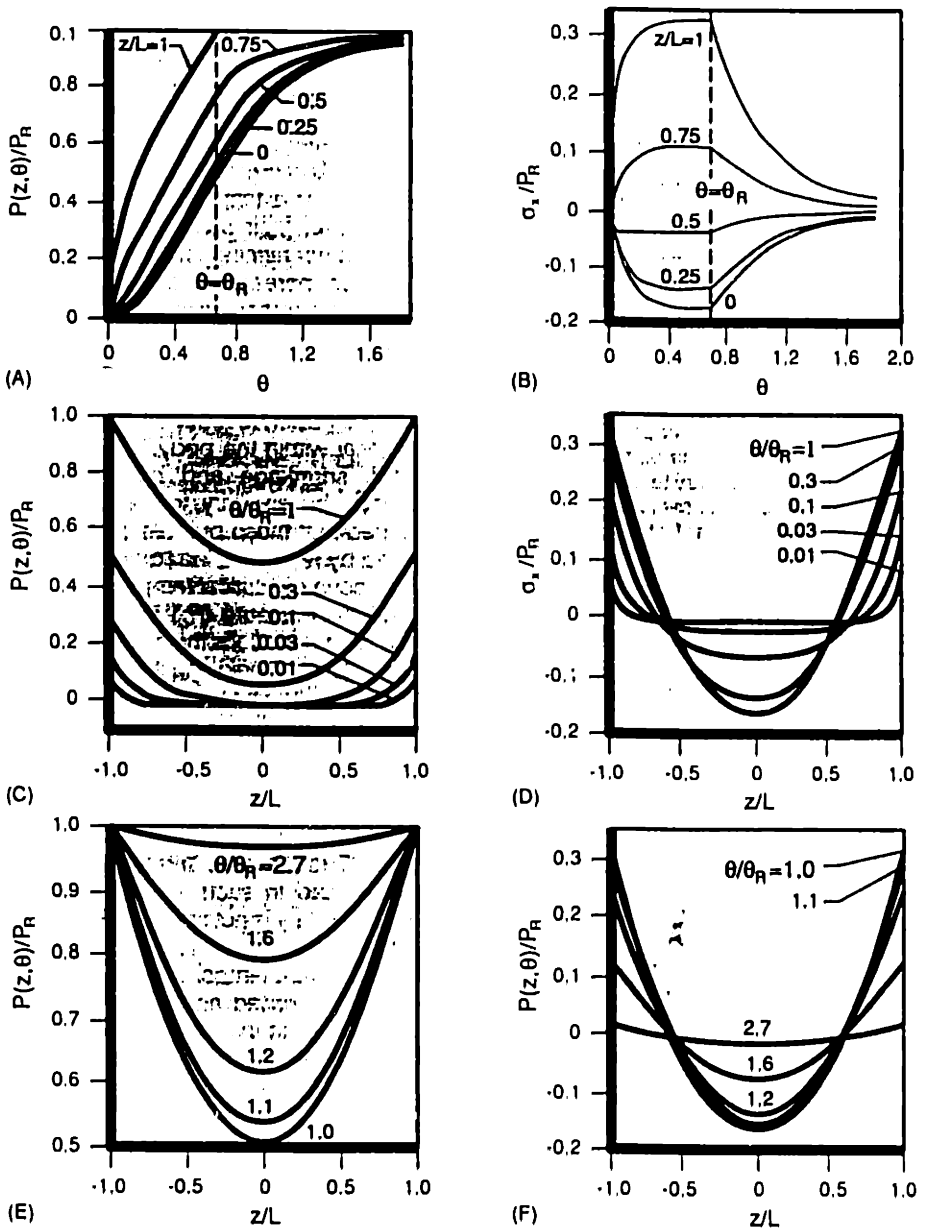

Figure 2.16. Drying behavior of a flat plate calculated by Scherer [30]: (A) normalized pressure (P/P_R) in liquid versus reduced time (θ) between exterior surface at $z/L = 1$ and midplane at $z/L = 0$; (B) normalized stress (σ_x/P_R) versus reduced time at the same locations as in (A); (C) pressure distribution at several times during the constant rate period ($\theta < \theta_R$); (D) normalized stress distribution at same times as in (C); (E) normalized pressure distribution at several times during the falling rate period ($\theta > \theta_R$); (F) normalized stress distribution at same times as in (E).

References

1. T.K. Sherwood, "The Air Drying of Solids," *Trans. AICHE* **32** [150] 150-168 (1936).

2. O.A. Hougen, H.J. McCauley, and W.R. Marshall, Jr., "Limitations of Diffusion Equations in Drying," *Trans. AICHE* **36** 183-209 (1940).

3. W.B. Haines, "Studies in the Physical Properties of Soils: IV. A Further Contribution to the Theory of Capillary Phenomena in Soil," *J. Agric. Sci.* **17** 265-290 (1927).

4. W.B. Haines, "Studies in the Physical Properties of Soils: V. The Hysteresis Effect in Capillary Properties, and the Modes of Moisture Distributions Associated Therewith," *J. Agric. Sci.* **20** 97-116 (1930).

5. E.W. Comings and T.K. Sherwood, "The Drying of Solids. VII Moisture Movement by Capillary in Drying Granular Materials," *Ind. Eng. Chem.* **26** 1096-1098 (1934).

6. N.H. Ceaglske and O. A. Hougen, "The Drying of Granular Solids," *Tran. Am. Inst. Chem. Eng.*, **29** [7] 805-13 (1937).

7. T.K. Sherwood, "Application of the Theoretical Diffusion Equations to the Drying of Solids," *Trans. AIME* **27**, 190-202 (1931).

8. A.V. Luikov, "Systems of Differential Equations of Heat and Mass Transfer in Capillary-Porous Bodies," *Int. J. Heat Mass Transfer* **18**, 1-14 (1975).

9. S. Whitaker, "Heat and Mass Transfer in Granular Porous Media," 23-61 in **Advances in Drying, Vol 1.** Edited by A.S. Mujumdar, Hemisphere Publishing Corp. New York, (1980).

10. T.M. Shaw, "Movement of a Drying Front in a Porous Material," Better Ceramics through Chemistry, edited by C.J. Brinker, D.E. Clark, and D.R. Ulrich, MRS Symposium Proceedings **73** North-Holland, Amsterdam (1986).

11. T.M. Shaw, "Drying as an Immiscible Displacement Process with Fluid Counterflow," Phys. Rev. Lett. **59** [15] 1671-1674 (1987).

12. J.F. Pearse, T.R. Oliver, and D.M. Newitt, "The Mechanism of the Drying of Solids: Part I. The Forces Giving Rise to Movement of Water in Granular Beds, During Drying," *Trans. Inst. of Chem. Eng.* **27**, 1-8 (1949).

13. T.R. Oliver and D.M. Newitt, "The Mechanism of the Drying of Solids: Part II. The Measurement of Suction Potentials and Moisture Distribution in Drying Granular Solids," *Trans. Inst. of Chem. Eng.* **27**, 9-18 (1949).

14. D. Wilkinson and J. Willemsen, "Invasion Percolation: A New Form of Percolation Theory," J. Phys. A **16** 3365-3376 (1983).

15. D. Wilkinson, "Percolation Effects in Immiscible Displacement," Phys. Rev. A **34** [2] 1380-1391 (1986).

16. R. Zallen, Chptr 4 in **Physics of Amorphous Solids**, Wiley, New York, 1983.

17. W.G. Lawrence, "The Structure of Water and Its Role in Clay-Water Systems"; pp. 193-210 in **Ceramic Processing Before Firing** edited by G.Y. Onoda, Jr. and L.L. Hench, John Wiley and Sons, New York, 1978.

18. J.N. Israelachvili and P.M. MuGuiggan, "Forces Between Surfaces in Liquids," *Science*, **241** 795-800 (1988).

19. R.J. Hunter, Chptr 6 in **Foundations of Colloid Science, Vol. I**, Oxford, New York, 1987.

20. R.J. Hunter, Chptr 8 in **Foundations of Colloid Science, Vol. I**, Oxford, New York, 1987.

21. R.J. Hunter, Chptr 7 in **Foundations of Colloid Science, Vol. I**, Oxford, New York, 1987.

22. R.W. Ford, **Institute of Ceramics Textbook Series: 3. Drying**, MacLaren and Sons Ltd., London, 1964.

23. H. H. Macey, "Clay-Water Relationships and the Internal Mechanism of Drying," Trans. Brit. Ceram. Soc. **41** [73] 73-121 (1941).

24. T. Kawaguchi, J. Iura, N. Taneda, H. Hishikura, and Y. Kobubu, *J. Noncryst. Solids*, **82** 50-56 (1986).

25. W.D. Kingery and J. Francl, *J. Am. Ceram. Soc.*, **37** [12] 596-602 (1954).

26. R.W. Lewis, M. Strada, and G. Comini, "Drying Induced Stresses in Porous Bodies," *Int. J. Numerical Methods in Eng.*, **11** 1175-1184 (1977).

27. P. Viollaz and C. Suarez, "Drying of Shrinkage Bodies," *J. AICHE* **31** [9] 1566-1568 (1985).

28. R.W. Lewis, K. Morgan, and H.R. Thomas, "The Nonlinear Modelling of

Drying-Induced Stresses in Porous Bodies"; pp233-264 in **Advances in Drying: Vol 2**, edited by A.S. Mujumdar, Hemisphere, New York, 1983.

29. A.R. Cooper, "Quantitative Theory of Cracking and Warping During the Drying of Clay Bodies"; pp.261-276 in **Ceramic Processing Before Firing** edited by G.Y. Onoda, Jr. and L.L. Hench, John Wiley and Sons, New York, 1978.

30. G.W. Scherer, "Theory of Drying," *J. Am. Ceram. Soc.* **73** [1] 3-14 (1990).

31. C.J. Brinker and G.W. Scherer, **The Physics and Chemistry of Sol-Gel Processing**; pp.453-513. Academic Press, New York, 1990.

32. M.A. Biot, "Generalized Theory of Acoustic Propagation in Porous Dissipative Media," *J. Acoust. Soc. A.* **34** [9] 1254-1264 (1962).

33. M.A. Biot, "Mechanics of Deformation and Acoustic Propagation in Porous Media," *J. Appl. Phys.*, **33** [4] 1482-1498 (1962).

CHAPTER 3

CRACKING BEHAVIOR OF GRANULAR CERAMIC FILMS

3.1 Introduction

Ceramic thick films, where thicknesses range from tens to hundreds of micrometers are generally produced from dispersions of granular ceramic particles. In these thick films, cracking occurs during the drying process. To prevent cracking, organic binders are typically added. However, binders are known to cause many other problems, such as carbon contamination and increased cycle-time, and it would be of great benefit to understand the source of drying defects so as to minimize the need for organic additives.

In this study, the cracking behavior of granular ceramic films produced from aqueous dispersions of alumina and silica was studied. Attempts were made to understand the strain development with respect to dispersion formulation and drying conditions. The important variables which affect the cracking behavior were identified with the aid of statistical fractional factorial design. The variables studied included particle size, effect of sedimentation, dispersion stability, surface tension, and air velocity during convective drying. The tendency toward cracking is measured by the critical cracking thickness (CCT) as described by Garino [1].

Drying experiments were also performed *in-situ* in an environmental scanning microscope (ESEM) at ElectroScan Co. (Wilmington, MA).

3.2 Experimental Procedure

The granular ceramic films used in this study were made from aqueous dispersions of α-alumina (20 vol%) and α-quartz (22 vol%). Two different alumina sources were used in the study, Sumitomo and Reynolds. The Sumitomo alumina powders have a narrow particle size distribution as received and are available in three different average particle sizes: 0.65 μm (AKP-15, lot# HL-8X01), 0.4 μm (AKP-30, lot# HE-0101), and 0.2 (AKP-50, lot# HD-8501). As received, the Reynolds alumina powder (RC172DBM, lot# N-1454) has an average particle size of 1 μm. Narrow particle size distribution Reynolds powder having average particle size of 0.4 μm was obtained through centrifugal classification [1]. Similarly, the silica powder (Grade 5x, Tatsumori Co., lot# 9K3115) had to be classified to obtain average particle sizes of 0.8 μm and 1.1 μm. The alumina suspensions were stabilized by adjusting the pH of the dispersions to approximately 3.5 with nitric acid followed by ultrasonication and readjustment of the pH to 3.5 the next day. In the case of silica, the dispersions were stabilized at pH 10. The films were cast onto 2.5 x 7 cm glass slides by uniformly spreading the dispersions with a glass rod.

To change the surface tension of the slips, a surfactant (Brij 30SP) was added to the deionized water. Aqueous surfactant solution surface tensions were

measured with a Wilhemy plate tensiometer. The contact angles were measured by a light reflection method described by Ford and Patterson [2].

Drying was done in a controllable convective drying environment. The apparatus consisted of a flow distributor and tunnel as shown in Figure 3.1. The flow distributor was packed with glass beads to produce a uniform air velocity profile over the drying film. The tunnel ensured controllable air velocity and humidity conditions. The apparatus was constructed from acrylic plates which allowed visual observation of the drying film. A 35 mm camera or a video camera was mounted in a such way that the film could be monitored in a plane view during drying.

The thickness of the dried films was determined by a focusing method using an optical microscope. The dried films were mechanically removed and their green densities and average pore sizes were measured with a Micromeritics Autopore II mercury porosimeter. Statistical variation of the green density measurements appears to be of the order of 0.5-1.0% of theoretical density.

The process variables chosen for statistical study were the particle size, sedimentation time, dispersion stability (pH), surface tension, and air velocity for convective drying. A two level fractional factorial approach was used. This amounted to 16 runs for five variables. Table 3.1 shows the matrix of experiments and the combination of the five process variables for each experiment. High and low levels of a variable are represented by a "+" or "-" sign, respectively.

For the particle size, 0.4 μm and 0.2 μm average particle size Sumitomo alumina powders were used as high and low levels, respectively. The effect of

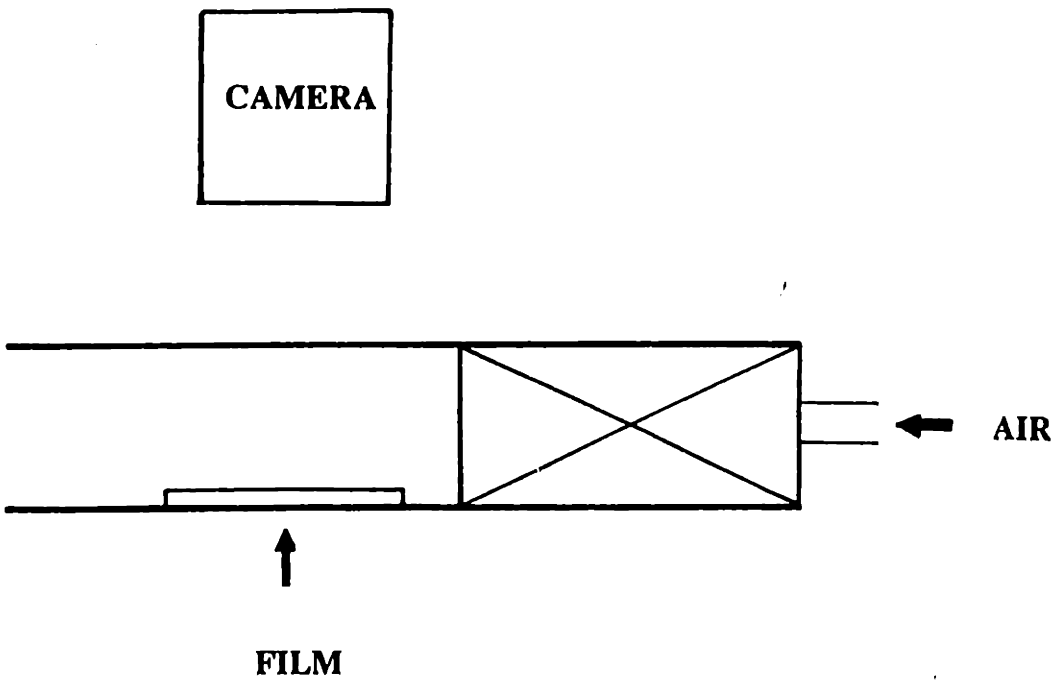

Figure 3.1. Schematic of the flow distributor used to control external drying conditions for a drying film experiment.

Table 3.1. Matrix of experiments for a 2^{5-1} fractional factorial design.

Design					
Run	**A**	**B**	**C**	**D**	**E**
1	-	-	-	-	+
2	-	-	-	+	-
3	-	-	+	-	-
4	-	-	+	+	+
5	-	+	-	-	-
6	-	+	-	+	+
7	-	+	+	-	+
8	-	+	+	+	-
9	+	-	-	-	-
10	+	-	-	+	+
11	+	-	+	-	+
12	+	-	+	+	-
13	+	+	-	-	+
14	+	+	-	+	-
15	+	+	+	-	-
16	+	+	+	+	+

sedimentation time was chosen at high level of four times the theoretical sedimentation time based on Stokes' law for a given film thickness. Zero sedimentation time was chosen as the low level. The low level of dispersion stability was achieved through slow, complete flocculation of a cast film. This was accomplished by increasing the pH of the supersaturated green film from 3.5 to approximately 8 with ammonia gas prior to drying. At the high level, the films were not flocced. Using the surfactant Brij 30SP, the surface tension of the DI water used for the slips were changed from a high level of 72 dyne/cm to a low level of 32 dyne/cm with 0.005 wt% surfactant addition. In convective drying, the drying rate can be varied by changing the air velocity. For the current setup, the convenient range for air velocity is between 3 - 6 cm/sec. Therefore, the high and low levels of air velocity used in convective drying were set at 3 and 6 cm/sec at 0% relative humidity, respectively. The levels used for each variable are summarized in Table 3.2.

Finally, to study the constraining effect of the substrate, films were also cast over a teflon plate and a pool of mercury. In the mercury case, drying was performed without force convection.

3.3 Results

Shown in Figure 3.2 is a sequence of photographs taken of a drying alumina film at different times. The markers at the tops of the photographs are 1 mm apart. A drying front can be seen advancing from the right to the left of the

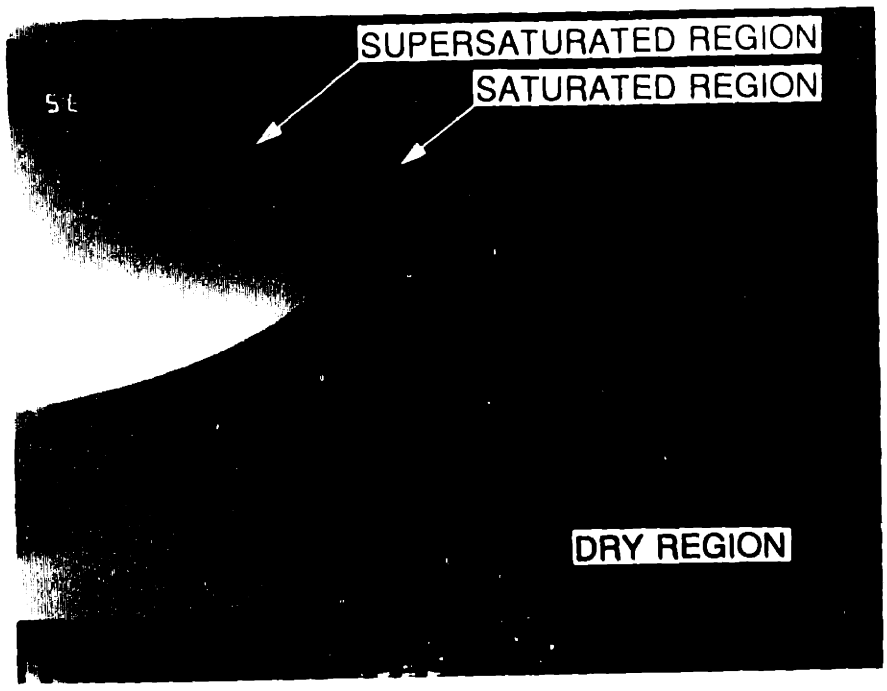

(a)

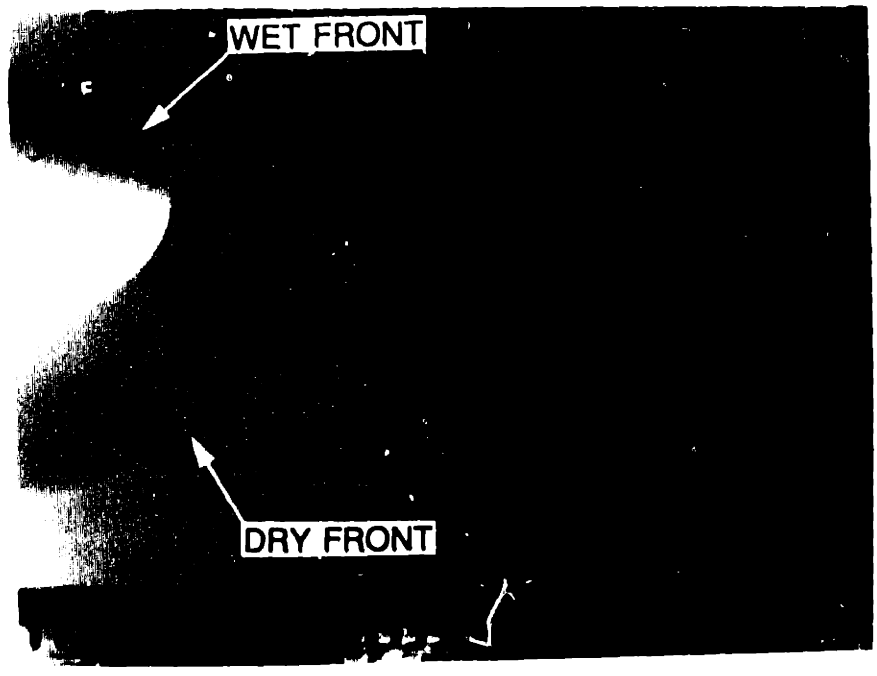

(b)

Figure 3.2. Pair of photographs taken seven minutes apart of a drying film.

Table 3.2. Variables and levels used in the study.

Variable		-	+
A	Particle diameter	0.2 μm	0.4 μm
B	Sedimentation time (normalized)	0	4
C	Dispersion stability (pH)	8	3.5
D	Liquid surface tension	32 dyne-cm	73 dyne-cm
E	Dry air flow rate	2.0 cm/s	6.7 cm/s

photographs. Three regions can be identified in this film. Farthest to the left, the film is still fluid and supersaturated; to the far right, the film is dry. A region of slightly different contrast can be observed between the two. Hereafter, we refer to the fluid, intermediate, and dry regions as supersaturated, saturated, and dry, respectively. These features were observed in nearly all the films dried in this study, with the exception of thicker films (nominal thickness > 150 μm) where the appearance of the saturated region was less pronounced. Under the optical microscope, the saturated region appeared translucent in the transmission mode. An optical micrograph showing the three regions during drying is shown in Figure 3.3. Using the 1000x objective under the optical microscope, a shrinkage of approximately 2% was observed between the saturated and the dried film.

Although the macroscopic cracks were found to occur perpendicular to the drying front and the crack tip in the saturated region, cracking was initiated from the dry region. Cracks were often observed to nucleate from trapped air bubbles in the granular film (Figures 3.4a-d). In some cases, however, cracking occurred in apparently defect free regions.

Drying experiments were also performed *in situ* in an environmental scanning electron microscope (ESEM) at ElectroScan Co. (Wilmington, MA). The sample chamber environment of the ESEM is approximately 8 torr of water vapor. Slow drying of the sample is achieved by initially chilling the sample to below the wet bulb temperature of water and then slowly increasing the temperature. The ESEM experiments were recorded with a video recorder. Crack tip was found to blunt and propagation occurred by a rupture type mechanism highly characteristic of a viscoelastic or viscoplastic material (Figure 3.5). This indicated that the saturated region was highly saturated with moisture. In Figure 3.6, the crack tip opening size for a dried film was found to be less than a particle diameter.

Shown in Figures 3.7a-d is a sequence of photos taken 1 min apart of a nominally 100 μm thick film produced from 0.4 μm particles. In Figures 3.8a-d and 3.9a-d, two sequences of photographs are shown for a 75 μm and 35 μm thick films produced from the same slip, respectively. Again, cracks were observed for thick films during drying and the cracks are perpendicular to the drying front. Note that the spacing between the cracks was quite uniform and is narrower for thinner films. From these photos, the movement of the drying fronts can be observed as a function of time. In Figure 3.10, the movement of the wet and dry

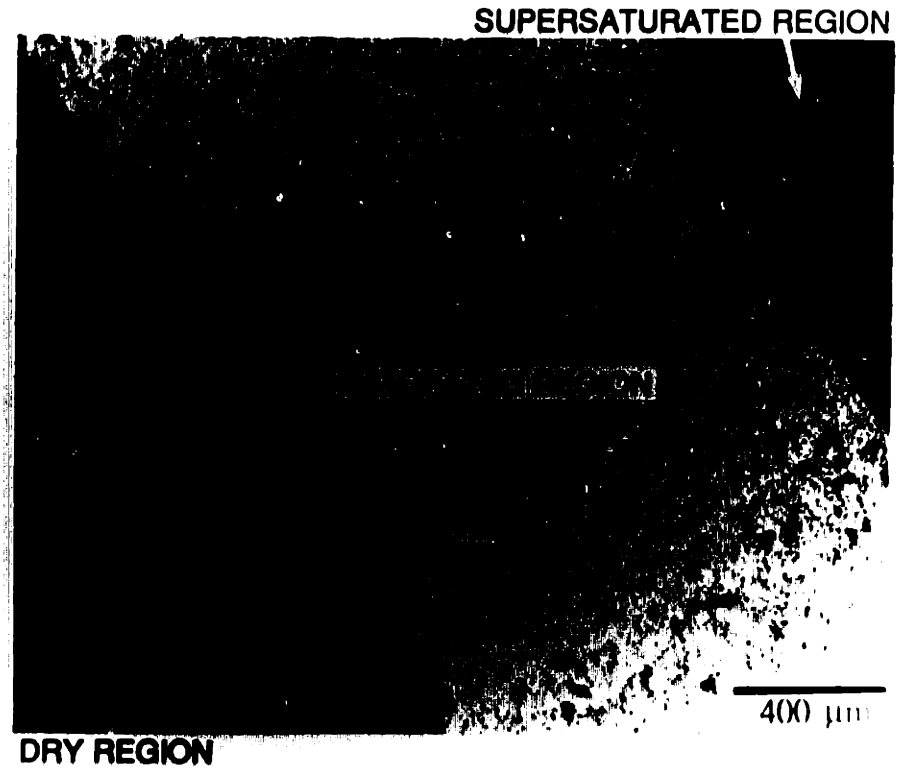

Figure 3.3. **Optical micrograph in transmission mode of a drying film. The supersaturated region is to the right, the dry region is to the left, and the translucent saturated region lies between the two.**

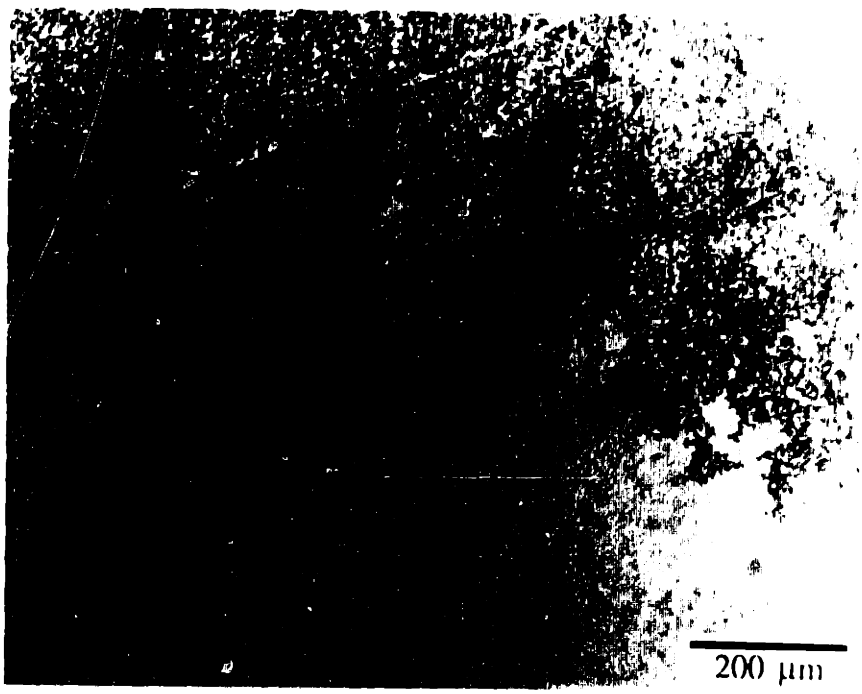

(a)

(b)

Figure 3.4. **Sequence of optical micrographs (a-d) showing a crack nucleating from a trapped air bubble in a drying film. The first three photos were taken under the combination of transmitted and reflected light while the last photo was taken in reflected light only.**

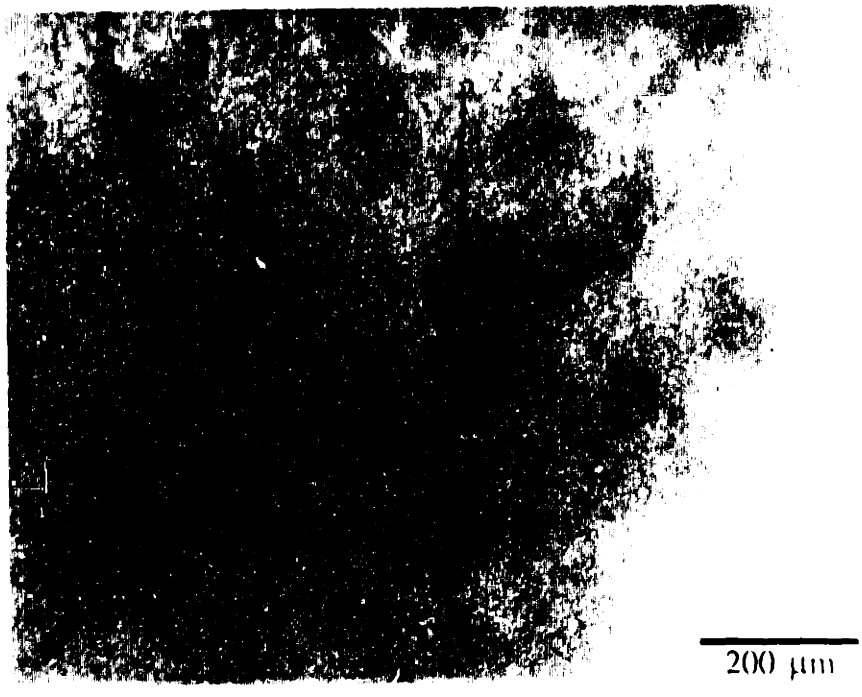

(c)

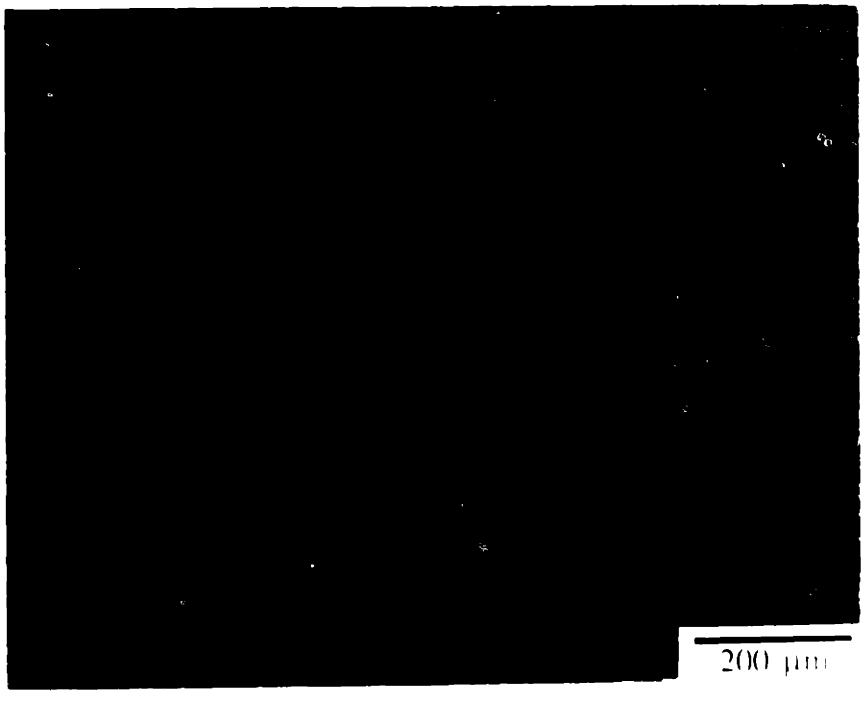

(d)

Figure 3.4 - cont.

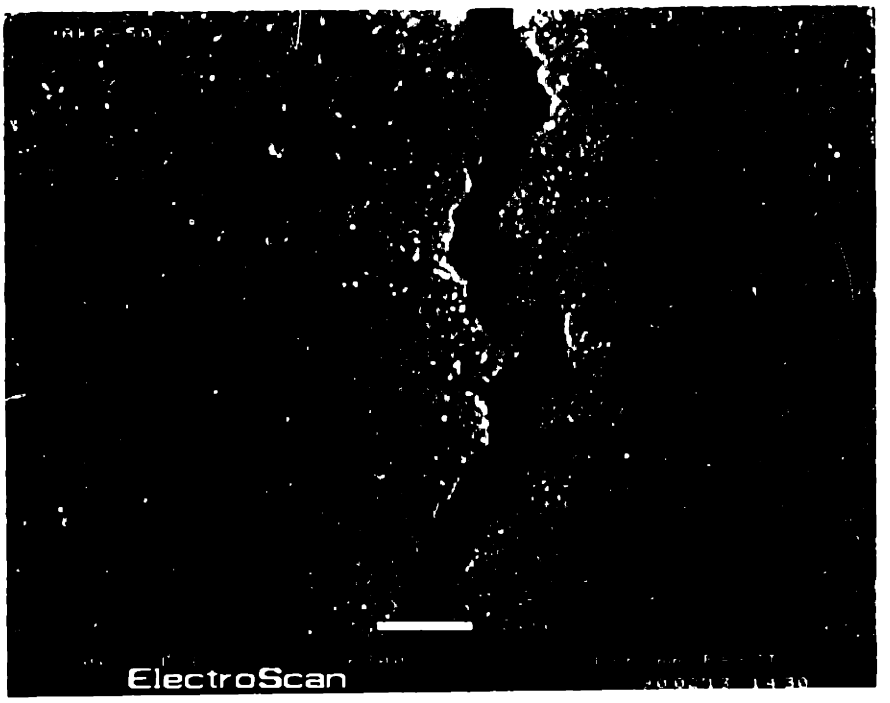

Figure 3.5. Environmental scanning electron micrograph taken of a film during drying. The crack morphology displayed plastic behavior.

Figure 3.6. Environmental scanning electron micrograph of a crack tip in a dried film.

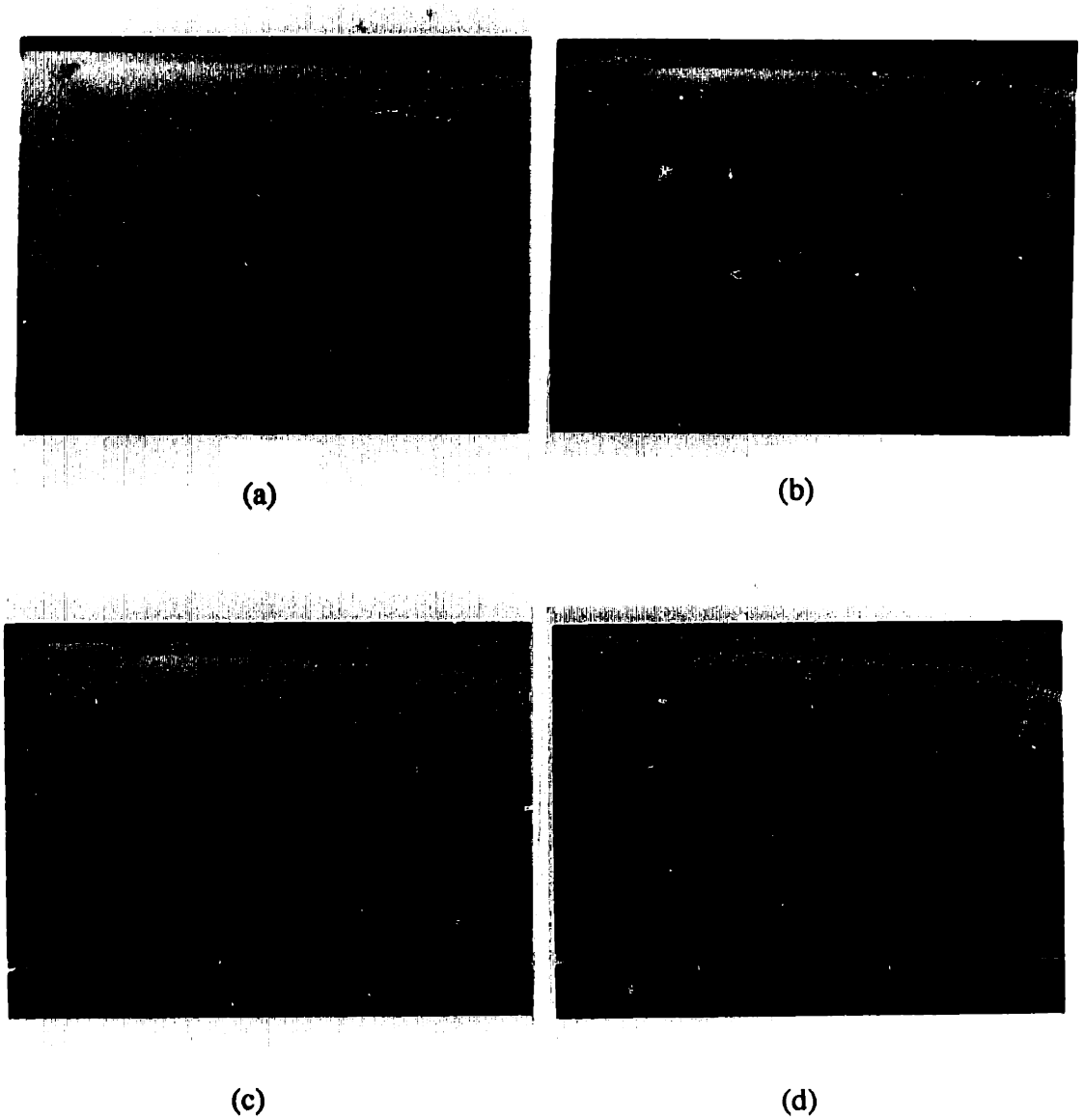

Figure 3.7. **A sequence of photographs taken of a drying film produced from 0.4 μm particle size alumina at 1 min intervals is shown from a-d. The nominal thickness of the film is 100 μm.**

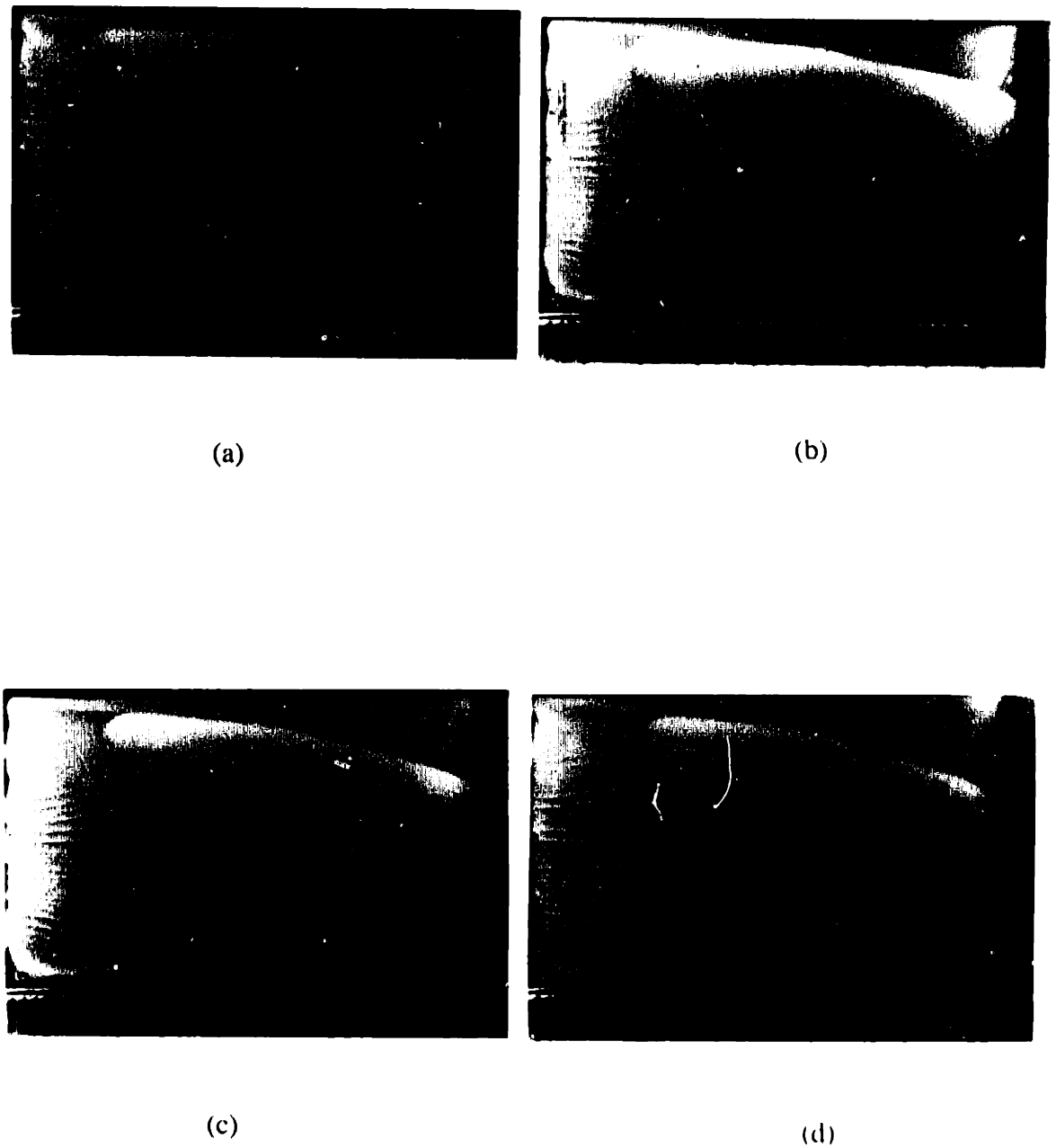

Figure 3.8. A sequence of photographs taken of a drying film produced from 0.4 μm particle size alumina a 1 min intervals (a-d). The nominal thickness of the film is 75 μm.

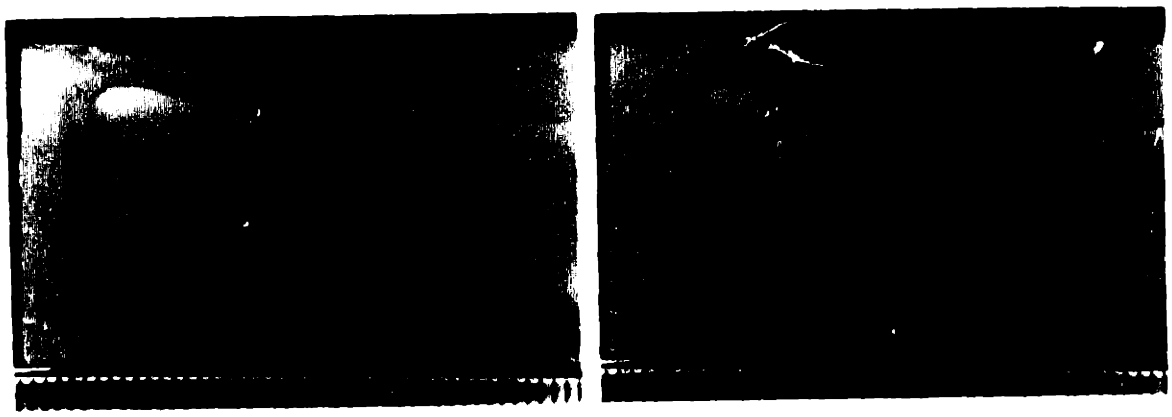

(a) (b)

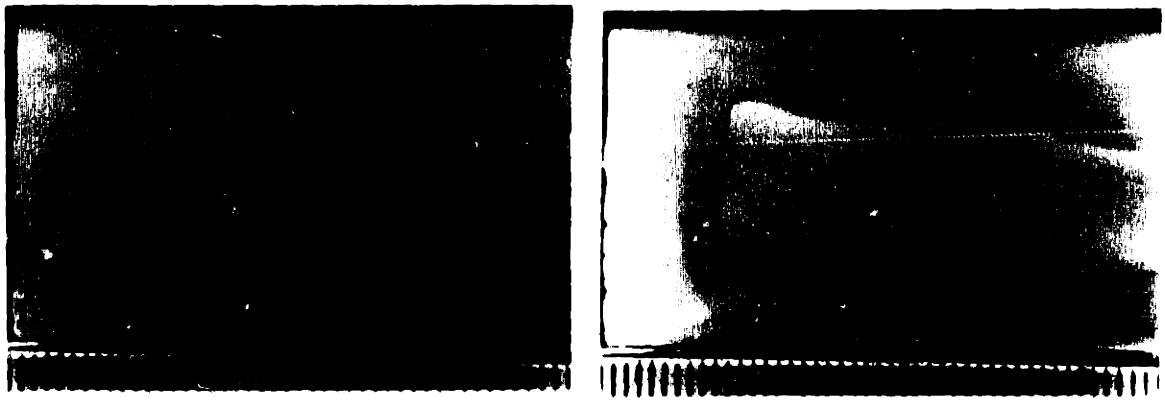

(c) (d)

Figure 3.9. A sequence of photographs taken of a drying film produced from 0.4 μm particle size alumina at 1 min intervals (a-d). The nominal thickness of the film is 35 μm. Unlike the ones shown in Figures 3.7 and 3.8, this film here is not cracked.

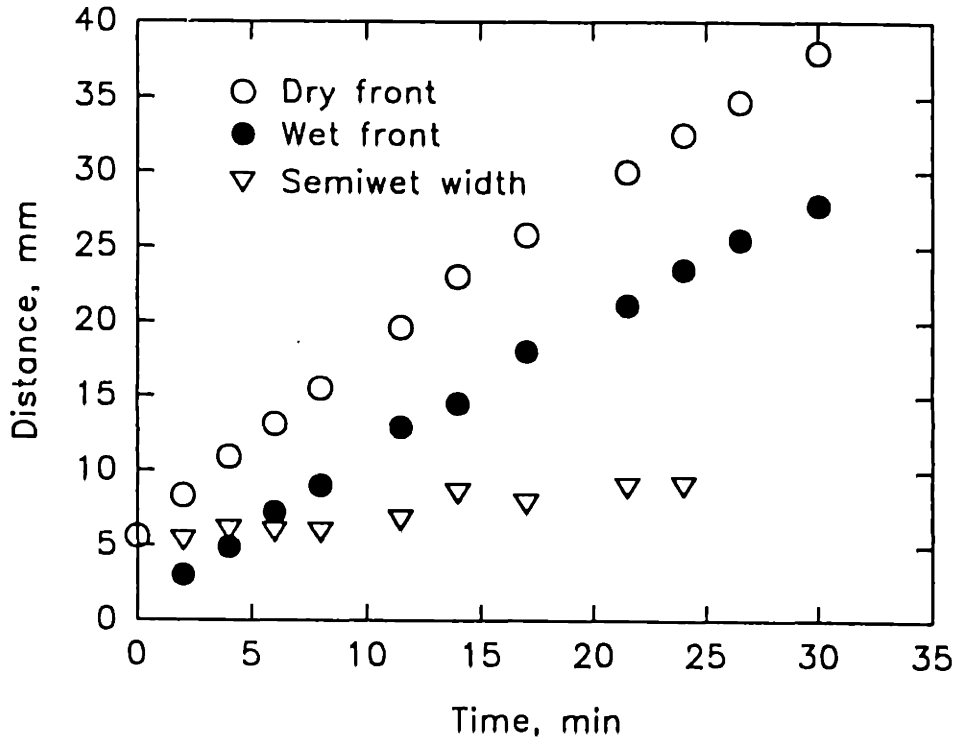

Figure 3.10. Position of the wet and dry front versus drying time for a nominally 100 μm thick film containing 0.4 μm particles. Distance was measured from the leading edge of the film for the fronts. The width of the saturated region was also plotted.

fronts were plot as a function of time for a nominally 100 μm thick film produced from 0.4 μm AKP30 alumina. Large thickness variation is found in this dried film as shown in Figure 3.11. Note that the saturated region is increasing in size as the film thickness increases.

Thickness profiles of films dried under various external drying conditions are shown in Figure 3.12. These films were cast from 0.4 μm particle size AKP30 alumina slips. With decreasing external drying rate (i.e., lower air velocity and humidity), the profiles increased in uniformity. At the highest and lowest drying rates, the films took approximately 1 h and 4 h to dry, respectively. Under identical drying conditions, higher uniformity was also achieved through properly treating the slip or the cast films prior to drying. This is demonstrated in Figure 3.13. At a relatively high drying rate, sedimentation prior to drying still produced a highly nonuniform film. Adding a surfactant to the slip and/or floccing the cast film prior to drying produced films of higher uniformity.

The results of the 16 experiments for the statistical experiment design are shown in Table 3.3. The average effect and the ranked estimated effects of the variables and the second order interactions between the variables are shown in Table 3.4. These estimated effects can be plotted on a normalized plot as shown in Figure 3.14. Graphically, the estimated effects that lie off the line that represents normal statistical variations in the data are the significant variables. These variables are labeled in Figure 3.14. They are particle size, particle size and double layer interaction effect, electrostatic repulsive layer, and sedimentation time.

The interpretation of these results is as follows. Eliminating the

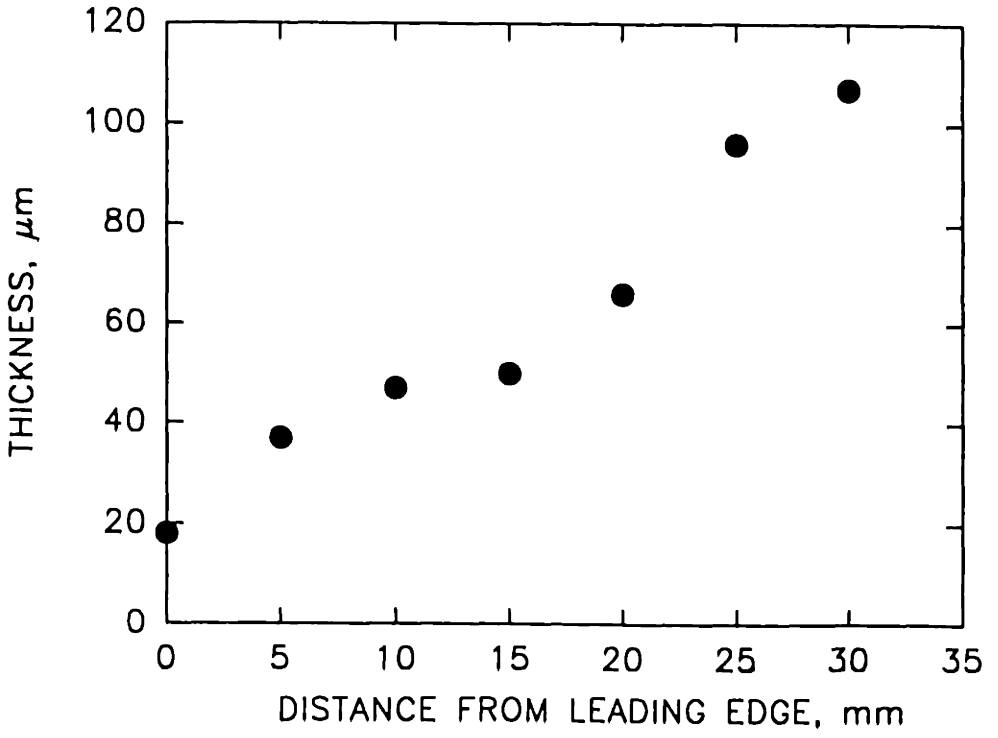

Figure 3.11. Thickness profile of the film shown in Figure 3.10.

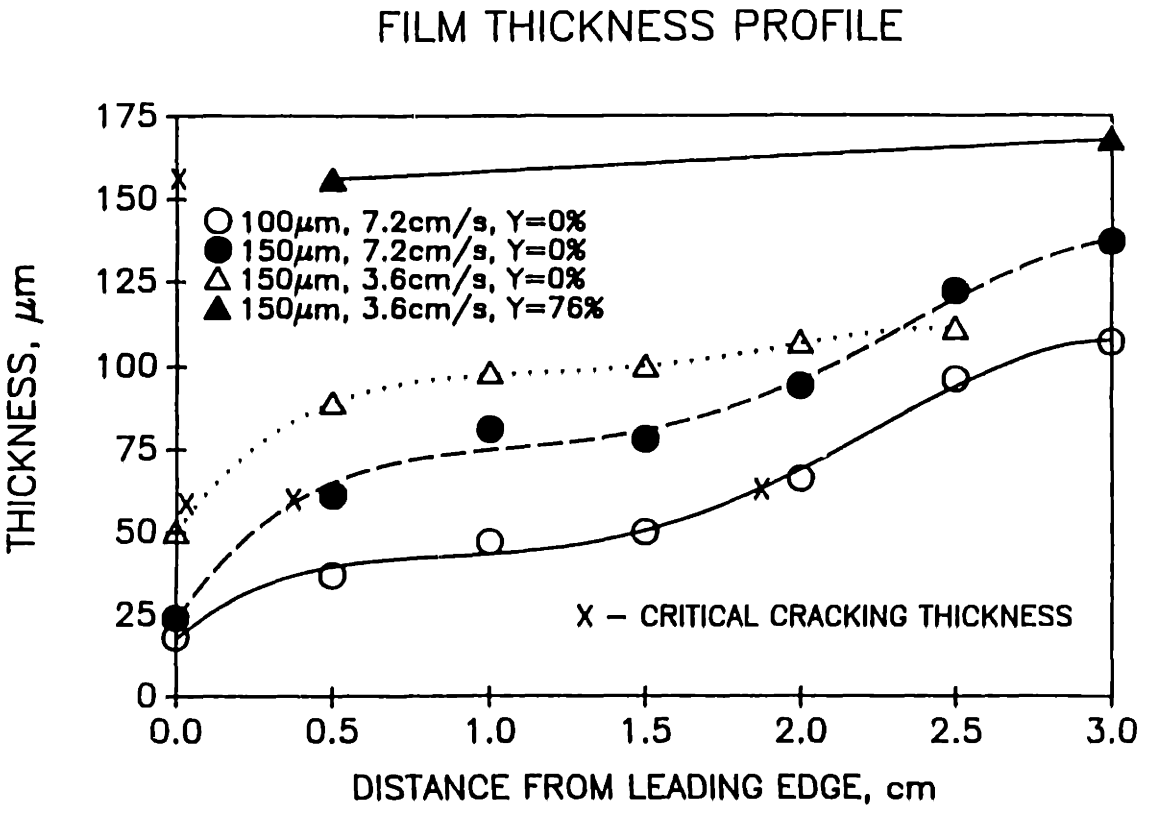

Figure 3.12. Thickness profile of films dried under various external conditions. The X indicates the critical cracking thickness.

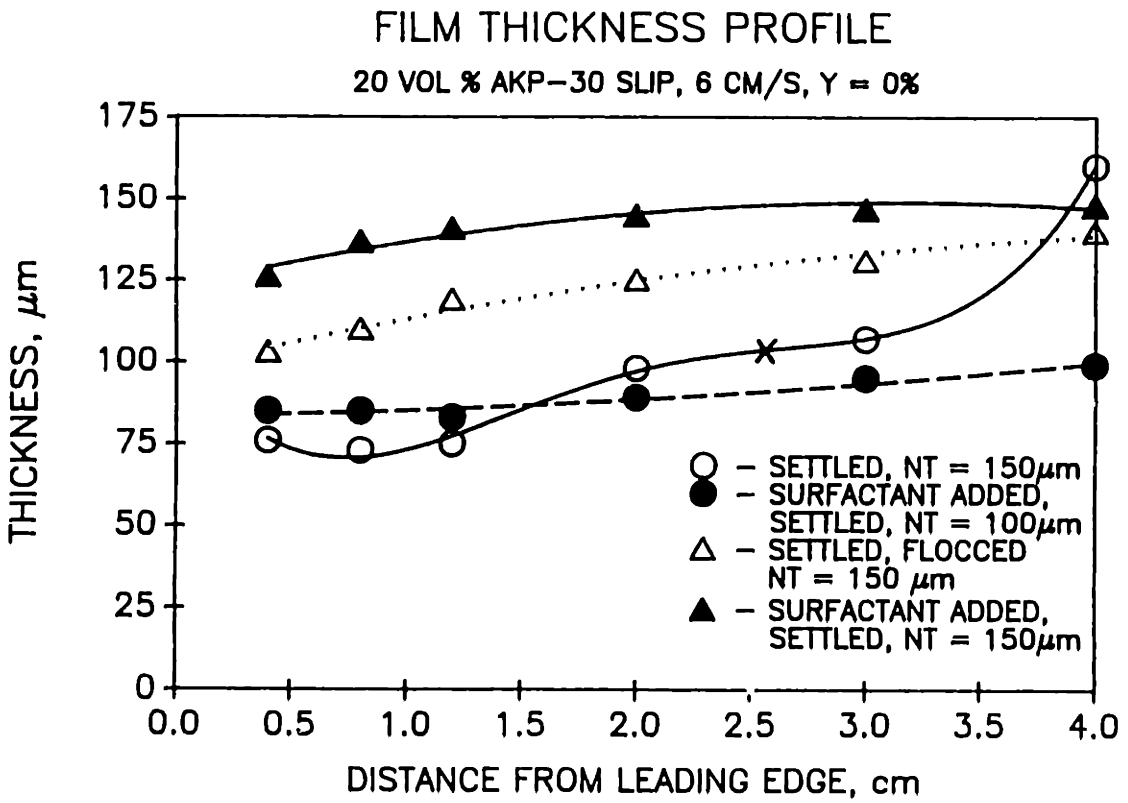

Figure 3.13. Effect of sedimentation prior to drying, lowering of surface tension, and flocculation prior to drying on the thickness uniformity of dried films.

Table 3.3. Results from the 2^{5-1} fractional factorial design study.

Design						
Run	**A**	**B**	**C**	**D**	**E**	**Response CCT, μm**
1	-	-	-	-	+	101
2	-	-	-	+	-	64
3	-	-	+	-	-	50
4	-	-	+	+	+	41
5	-	+	-	-	-	108
6	-	+	-	+	+	140
7	-	+	+	-	+	93
8	-	+	+	+	-	47
9	+	-	-	-	-	164
10	+	-	-	+	+	175
11	+	-	+	-	+	81
12	+	-	+	+	-	61
13	+	+	-	-	+	187
14	+	+	-	+	-	215
15	+	+	+	-	-	98
16	+	+	+	+	+	99

Table 3.4. Analysis of the responses for the 2^{5-1} design.

Estimate of Effects	
Average	107.75
A	27.25
B	15.625
C	-36.5
D	-2.5
E	6.875
AB	-0.875
AC	-13.75
AD	5
AE	-6.375
BC	-2.625
BD	4.375
BE	-0.5
CD	-6.75
CE	0.375
DE	1.625

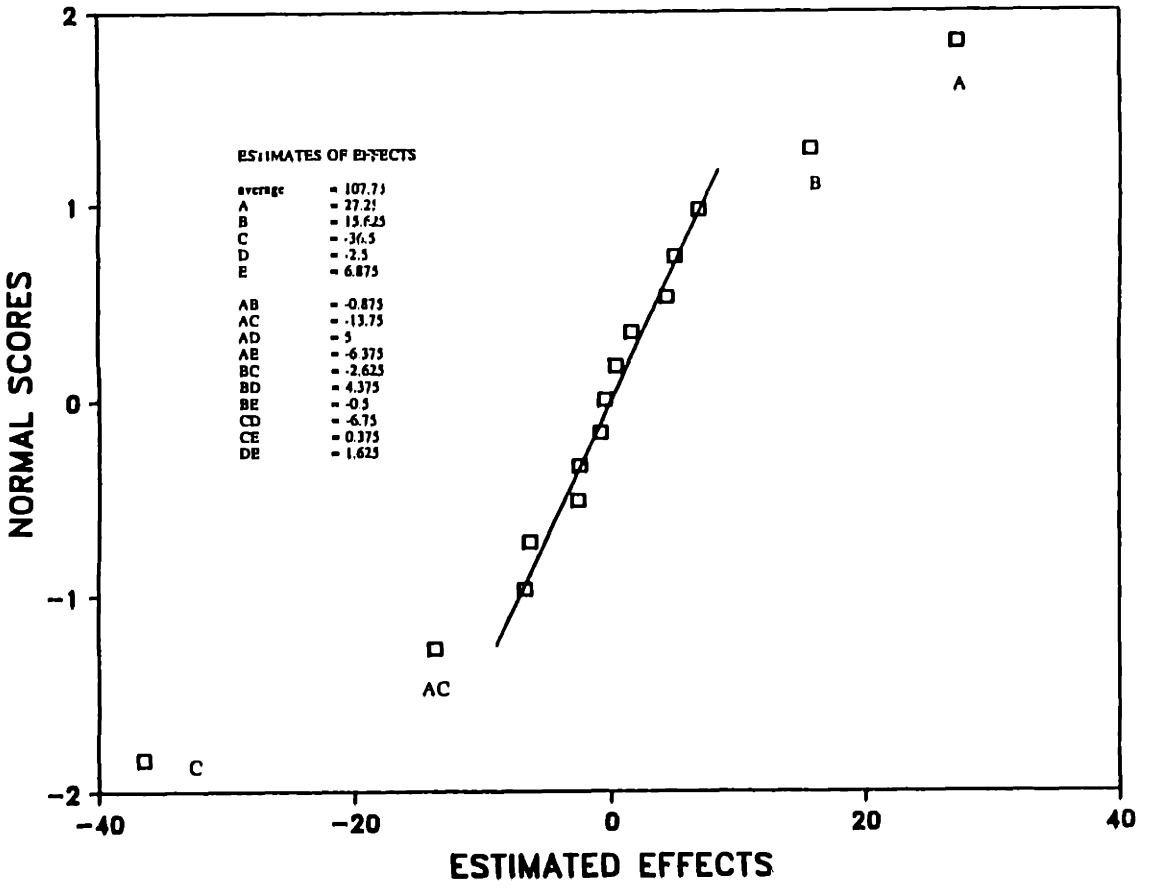

Figure 3.14. A normalized plot of the ranked estimated effects. The significant effects are labeled.

electrostatic double layer between particles or flocculating the wet green film before drying causes a large increase in CCT. A positive estimated effect in the particle size indicates films fabricated from a larger particle size slip are less susceptible to cracking. A negative interaction between the electrostatic double layer effect and the particle size indicates the electrostatic double layer effect is larger for smaller particles. Finally, a longer sedimentation time can also increase the CCT.

Care must be taken in identifying significant variables using statistical design. The sensitivity of each variable is limited to the levels chosen for that variable. For example, although the air velocity did not appear significant from the design experiments, a significant increase in the CCT from 60 μm under normal drying conditions to >175 μm was found for a film cast from an AKP-30 slip dried slowly over 48 h.

Green densities of films made from 0.4 μm particle size slips were measured and are summarized in Table 3.5. Films flocced prior to drying typically showed lower green density values than the ones that were not. Also, sedimentation led to higher green density in both flocced and unflocced films. Finally, the films cast on teflon did not crack but spalled and warped, concaving upward on the substrate. On a mercury pool, greater than 2 mm crack-free films were produced without warping. The green density of the films cast on mercury were 65% of theoretical.

3.4 Discussion

Table 3.5. Summary of green density data.

Conditions		Green Density % of Theoretical
Sedimentation	Flocculation	
no	no	59
no	yes	49
yes	no	61
yes	yes	53
no	no	65*

* film cast on a Hg pool.

The translucent appearance of the saturated region (Figure 3.5) under transmission mode in an optical microscope suggested that the granular film may still be completely saturated with liquid. In fact, in the adjacent "drier" region of the film, an increase in scattering made that region appear more opaque. This is expected since the indexes of refraction between water and alumina is more closely matched that those between air and alumina. In fact, the completely dried granular film cannot be observed under the optical microscope in the transmission mode.

The variation in film thickness in the dried films as shown in Figure 3.12 can be explained by the following. In the dispersed state at a low volume of solids, the ceramic particulate and the liquid vehicle behave rheologically as a continuum. The fluid region is supersaturated and makes contact with the

saturated region at a contact angle of approximately 20°. Slower drying reduces the gradient in film thickness, as does reducing the surface tension (Figure 3.13) of the liquid by addition of a surfactant. It is thought that heterogeneous distribution of particles on the substrate surface is largely the result of the liquid meniscus sweeping across the substrate during convective drying. Larger amounts of slurry are deposited on the trailing edge of the substrate, because the supersaturated region has a specific contact angle with the saturated region and the last bit of supersaturated slurry is always found near the trailing edge. Slowing the drying rate allows the particles to settle rather than be carried along by the liquid. Allowing time for the particles to settle prior to drying also had the same effect. A lower surface tension decreases the contact angle that the supersaturated region makes with the saturated region and therefore extends the supersaturated region toward the leading edge for a given volume of liquid. In the case of a flocced film, the large agglomerates settled quickly and thickness variation was even less pronounced.

Figure 3.10 indicates how the positions of the wet and the dry fronts change with time. The width of the saturated region increases with time. This phenomenon can be understood by considering the combined effects of the gradient in film thickness and the capillary suction of the saturated region. Capillary suction withdraws liquid from the supersaturated region much as a wick pulls liquid from a reservoir. Semisaturated granular bodies are known to evaporate at a constant drying flux because of the capillary migration of liquid to smaller pores near the surface of the body (see Chapter 2). Thus, a constant

drying flux can be assumed everywhere in the saturated region. The distance over which liquid is wicked away from the supersaturated region is limited by the balance between the suction pressure and the pressure drop due to flow of the liquid through the plane of the granular film. Integration of the pressure drop along the width of the saturated region can be performed by assuming that the pressure drop due to flow is governed by the Kozeny equation, and that the pressure at the supersaturated-saturated interface is atmospheric (P_0) and the pressure at the saturated-dry interface is entry suction pressure (P_s) of the granular film. Of course, the flow must be augmented to account for the constant drying flux out of the film. Assuming the saturated region is near full saturation, mass balance around an incremental element of length dx yields (see Figure 3.15),

$$\frac{du}{dx} = \frac{j}{h} \qquad \textbf{3.1}$$

where u is the fluid velocity, j is the drying flux, and h is the film thickness. Substituting the Kozeny equation for the fluid velocity, equation 3.1 becomes

$$\frac{d^2P}{dx^2} = \frac{150(1-\varepsilon)^2 l^2 j}{d^2 \varepsilon^3 h} \qquad \textbf{3.2}$$

where l is the length of the saturated region, ε is void fraction, and d is the granular particle size. The pressure distribution is solved using the boundary conditions $P = P_0$ at $x = 0$, and $P = P_s$ at $x = l$ to give

$$\frac{P-P_0}{P-P_s} = \frac{\lambda}{2}\left(\frac{x}{l}\right)^2 + \left(1-\frac{\lambda}{2}\right)\left(\frac{x}{l}\right) \qquad \textbf{3.3}$$

where

$$\lambda = \frac{150(1-\varepsilon)^2 l^2 j}{d^2\varepsilon^3(P_s-P_0)h} \qquad \textbf{3.4}$$

From an overall mass balance around the saturated region, $hu_0 = jl$, the following expression for the width of the saturated region is derived:

$$l = \sqrt{\frac{d^2\varepsilon^3\Delta P h}{75\eta(1-\varepsilon)^2 j}} \qquad \textbf{3.5}$$

The capillary pressure (ΔP) can be estimated by $2\phi/d$ where ϕ is a geometric factor based on particle packing [3].

From the air velocity and humidity, the external evaporation rate can be estimated from well established correlations [4]. A low estimate of the external evaporation rate can also be calculated from the velocity of the drying fronts. The rates calculated from the two methods are both on the order of 10^{-6} kg/m^2-s. Substituting the numerical values and physical constants, l for a 100 μm film produced from 0.4 μm size particles is on the order of 1 cm. The width of the saturated zone in the drying film shown in the photos in Figure 3.2 appears to be consistent with the calculated value. From our simple analysis, the length of the

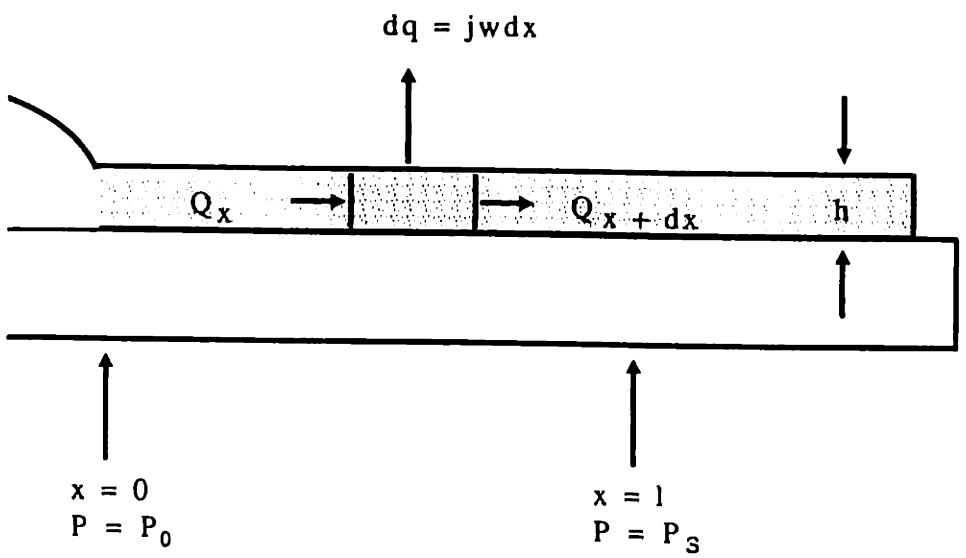

Figure 3.15. Schematic of the saturated region in a drying granular film.

saturated region should also scale with the thickness of the film to the 1/2 power. Examining Figures 3.10 and 3.11, by doubling the film thickness from 50 to 100 μm, the width of the saturated region increased from 0.6 to 0.9 cm, which is roughly a 0.6 power dependence on the film thickness. This simple analysis also allow the dimensions of a granular films in which a uniform saturation can maintained during drying to be predicted. This result will be further confirmed and made use of in the next chapter.

While the application of statistical experimental design methodology allows one to identify important parameters associated with a process, the results do not necessarily lead to a complete picture of the physics of the process. In the present study, the effect of the interaction potential, particle size, and sedimentation time were found to affect the cracking tendency during drying of binder-free alumina films. How these observations help us better understand the physical mechanisms leading to cracking in these films is discussed below.

Observations under the optical microscope indicated that the saturated region of a drying film was fully saturated. The fact that a small shrinkage (~2%) had occurred during drying suggested that the dispersed ceramic particles remained separated in the saturated state. This observation is also consistent with the drying shrinkages observed in centrifugally cast binder-free alumina components reported by Beylier *et al.* [5]. For 0.4 μm particles, a 2% strain means that the particles in the film are on the order of 8 nm apart. The thickness of the electrostatic repulsive layer between dispersed particles can be estimated by the inverse of the Debye-Huckel parameter, $\kappa = 3.288I^{0.5}$ $(nm)^{-1}$ where I is the ionic strength in mol/L

[6]. At a pH of 3.5, the Debye layer was estimated to be ~8 nm. Therefore, the strain observed is likely due to the collapse of the electrostatic repulsive layer by the capillary forces during drying. Using smaller size particles increases this strain since the ratio between the actual double layer thickness and the particle diameter is larger. Biaxial stress can develop in the film due to this shrinkage in two different ways. If a moisture gradient exist across the thickness of the drying film, different shrinkage can cause cracking to occur. This argument can also explain the occurrence of a critical cracking thickness. Even with uniform shrinkage, however, a tensile stress as high as the capillary pressure of the liquid can develop in the film due to the rigid constraint [7]. In this case, the stress developed in the film will be decreased for lower liquid surface tension and for larger particles, as dictated by the capillary origin. First, the possibility of the differential shrinkage case will be examined.

Typically, stress development during drying is attributed to the moisture gradient which develops in the green body [8]. Due to a net shrinkage between the wet and dried green body, a steep moisture gradient can induce detrimental differential stresses which lead to cracking during drying of the green body. To determine whether steep moisture gradients can develop in a green body during drying, one has to consider the free surface evaporation rate which is dictated by external drying conditions and the ability of the green body to redistribute liquid internally. If the redistribution rate of liquid moving to the surface to evaporate is at pace with the evaporation rate on the surface, the moisture gradient that develops during drying is typically diffuse. If the redistribution rate is slow

compared to the evaporation rate, a sharp moisture gradient or drying front can develop across the green body perpendicular to the direction of drying.

The driving forces responsible for the redistribution of liquid during drying are a result of the different capillary pressures associated with different pore sizes in the packed porous structure [9]. To determine the conditions permitting capillary forces to redistribute liquid to the surface for evaporation, one can make use of the relation derived by Lewis and Cima [10]:

$$\frac{h}{d} = \frac{\Delta\phi}{90(1-\varepsilon)^2}\frac{\gamma}{\upsilon G} \qquad 3.6$$

where υ is the kinematic viscosity, G is the mass flux for surface evaporation, h is the thickness of the green film, d is the particle diameter, γ is the surface tension, ε is the void fraction of the green body, and $\Delta\phi$ is a geometric factor based on differences in particle packing. For a randomly packed structure, $\Delta\phi$ and ε are estimated at 8 and 4, respectively. This relation is derived by equating the viscous pressure drop for flow across the thickness and the suction pressure provided by the difference in pore size of a randomly packed green body consisting of mono-sized spheres. Again, the viscous pressure drop is estimated by the Kozeny equation, and the suction pressure equation is based on the relation developed by Haines [3]. Graphically, one can make a plot of:

$$\log\frac{h}{d} = \log\frac{\gamma}{\upsilon G} - 1.8 \qquad 3.7$$

to define a region where capillary redistribution can act. This is shown in Figure 3.16. In the region to the right, capillary suction pressure is large enough to

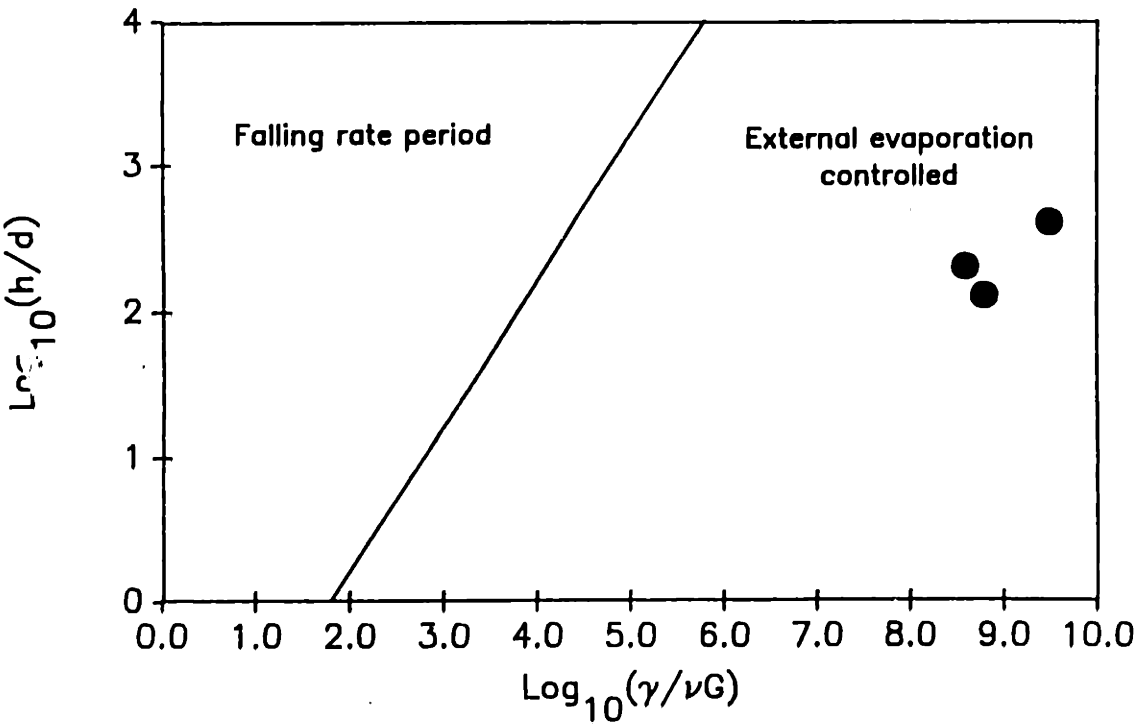

Figure 3.16. Plot of Equation 3.7 showing the regions of external drying-control for liquid movement in a porous compact. The filled circles represent the present experimental conditions.

maintain a flow to the surface of the green body for evaporation. To the left of the boundary, the surface evaporation rate is too high for the redistribution to keep pace with the external drying conditions. Therefore, the drying rate falls as all the surface pores penetrate into the green body, and consequently a sharp drying front develops.

With this analysis, the importance of capillary redistribution can be assessed for the external drying conditions used in this study. The surface evaporative flux was measured to be on the of 1×10^{-6} kg/m^{2}·s. The solid circles in Figure 3.16 correspond to present drying conditions. Clearly, capillary redistribution is dominant. A sharp drying front was not likely to have developed during drying.

Another approach to investigate the moisture distribution in a porous particulate body was taken by Shaw [11]. In that study, the drying process was modeled as an invasion percolation process. The results from Shaw's 2-D model suggest that the width of a drying front depends on the drying rate. At slow drying rates, a diffused drying front is expected; as the drying rate increases, a sharp front can become stable. Based on Shaw's results, the width of a drying front is approximately 2-3 orders of magnitude of the particle size for the drying conditions in this study. Extrapolating Shaw's results to a 3-D case, which is a better approximation of the present situation, the width of the drying front is expected to increase further [12]. Therefore, a drying front width that is approximately an order of magnitude wider than the film thickness is expected. Correspondingly, the moisture gradient which develops during drying should be diffused.

The argument for differential stress generated by moisture gradient during drying is also inconsistent with a couple of observations. First, if moisture gradient were important, the observed CCT would have been sensitive to the drying rate. Secondly, a moisture gradient is a self-constraining situation, therefore, regardless whether the film is dried on a rigid constraint or not, cracking should be equally likely to occur. The films cast on a mercury pool, however, was found to have extremely high CCTs of over 2 mm, suggesting that the stress is related to the constraint of the rigid substrate. The effect of sedimentation on lowering the tendency toward cracking is not clear from this model either.

Recently, Hu *et al.* [13] analyzed the mechanics of cracking of thin films on rigid substrates. Their theoretical estimates for elastic homogeneous systems indicate that there exist a critical cracking thickness above which a stressed film will crack. Consider a crack of length z extending through a thin film as shown in Figure 3.17b, the strain energy release rate is

$$G = \frac{1.2\pi\sigma^2 z}{E} \qquad \textbf{3.8}$$

where σ is the tensile stress and E is the Young's modulus of the film. By definition,

$$G = -\frac{\partial U}{\partial A} \qquad \textbf{3.9}$$

therefore, the difference in the strain energy of a fully cracked film and an uncracked film of width l can be derived as

But ΔU is also the strain energy difference between an element of thickness l in

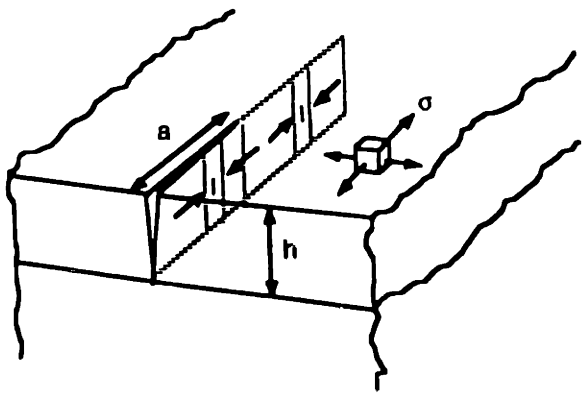

(a)

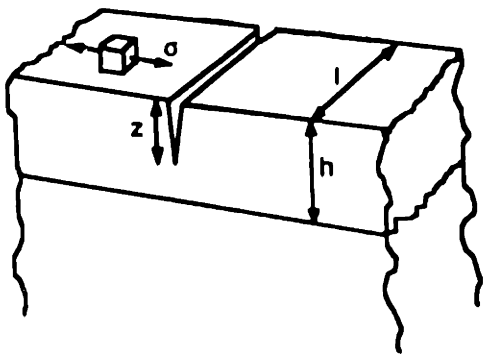

(b)

Figure 3.17. (a) A section of a crack extending through thin film; (b) a steady-state film crack [13].

$$\Delta U = l\int_0^h G dz = 0.6\pi a^2 \frac{lh^2}{E} \qquad 3.10$$

front of a crack growing along the film and a similar element in the crack wake (Figure 3.17a). The steady state energy release rate for a crack extension along the film is thus

$$G \equiv \frac{\Delta U}{hl} = 0.6\pi\sigma^2 \frac{h}{E} \qquad 3.11$$

Correspondingly, the stress intensity factor is

$$K_I \equiv (EG)^{1/2} = 1.4\sigma\sqrt{h}. \qquad 3.12$$

Therefore, as the thickness of a stress film is increased, cracking could occur when the stress intensity factor reached the critical value. In essence, cracking will not occur when the energy invested to form a crack in a thin film is larger than the energy gained in relieving the strain in the film. Now let's examine whether our observation of critical cracking thickness during drying of these granular films is consistent with this analysis.

Since a moisture gradient is not likely to exist across the thickness of a drying film, the biaxial stress that's developed in the film during drying should be proportional to the capillary pressure. The capillary pressure developed in a drying granular body is inversely proportional to the granular particle size; therefore, films produced from smaller granular particles would experience a larger stress than those produced from smaller ones. Correspondingly, the CCT for films produced from larger particles were higher. Also, the capillary tension that developed in a

drying film is independent of the drying rate; therefore, one would not expect the drying rate to affect the tendency toward cracking. Films that were flocced using ammonia gas had lower green density (53%) and larger average pore size (120 nm) that those that were not flocced prior to drying (62% and 68 nm, respectively). In that case, a lower tendency toward cracking was also observed, consistent with smaller capillary stress due to increase in porosity.

Interestingly, lowering of the surface tension which lowered the capillary pressure did not cause an increase in critical cracking thickness. But the strength of a semi-saturated film may also be a function of the surface tension of the liquid [14]. Since CCT is a measure of both the magnitude of stress the film experiences during drying and the strength of the film, lowering surface tension may have canceling effects on the CCT. The increase in critical cracking thickness by allowing the particles to settle prior to drying is still unclear. From the green density data, the settled films had slightly higher green densities; therefore, one would expect the average capillary pressure developed during drying to be even higher, which would produced a film having lower CCT. One possible explanation may be that by allowing the particles to settle prior to drying, a more uniformly packed film having smaller packing "defects" can be produced. Since the tendency toward cracking in a material is both a function of the intrinsic defect size and the applied stress, a more uniformly packed granular film having smaller inherent defects will be less susceptible to failure than one with higher particle packing inhomogeneities. This can also explain the observed increased in CCT for extremely slowly dried film in which particles had sufficient time to settle prior to

drying.

The observations presented here is also consistent with those obtained for sol-gel derived films in which film thicknesses greater than 0.5 μm were nearly impossible to dry without defects [15, 16]. Since sol-gel films have pore sizes approximately 2 orders of magnitude smaller that those of the granular films studied here, the capillary stress generated in those films must also be 2 orders of magnitude higher. Consequently, CCT of approximately 0.5 μm were observed for sol-gel derived films, which is two orders of magnitude smaller than those observed for granular films produced from submicrometer size particles.

Admittedly, the results presented in this study using CCT as a measure of tendency toward cracking cannot provide quantitative evidence to identify the origin of the stress developed in granular ceramic films during drying. Therefore, it would be informative to measure *in-situ* the stress experienced by the films during drying. In the next chapter, a substrate deflection method was employed to measure this stress during drying. The results confirmed that the stress generated during drying in these granular films is related to the capillary tension of the liquid. Estimates of the mechanical integrity of the dried green films were also obtained from the CCT and drying stress values.

3.5 Conclusions

The drying behavior binder-free granular ceramic films produced from submicrometer size alumina dispersions was studied. Large thickness variation

was found in the dried films due to the high contact angle that the slip makes with the substrate. High thickness uniformity can be obtained by allowing the particles to settle prior to drying and/or adding a surfactant to lower the contact angle between the slip and the substrate.

Cracks were found in films produced above a critical thickness, consistent with Garino's observations [1]. The processing variables thought to affect the cracking tendency of binder-free granular films are particle size, sedimentation time, dispersion stability (pH), liquid surface tension, and dry air velocity during convection drying. For the first time, a statistical experimental design methodology was applied to study these processing variables. Critical cracking thickness was used as a measure of cracking tendency in these films. The processing parameters identified to be important were particle size, dispersion stability, and sedimentation time. Cracking is less likely for green films produced from larger size particles, flocced films, and/or films that were allowed for the particles to settle. Interestingly, the drying rate has no effect on the drying behavior or these films. In fact, the benefit from using extremely slow drying rates may be an effect of sedimentation instead.

Typically, differential shrinkage leading to cracks in bulk green ceramic components is attributed to steep moisture gradient that is developed during drying. The small shrinkage observed during the drying of the green films was attributed to the collapse of the electrostatic repulsive layer between dispersed particles. A steep moisture gradient, however, is not expected to develop across the thickness of these films during drying. Theoretical calculations have shown that moisture

gradients are unlikely to develop under the present drying conditions for film thickness less than approximately 10^3 - 10^4 particle diameters. Also, the shape of the moisture gradients are a function of the external drying conditions. In this study, the cracking tendency was found to be insensitive to changes in the external drying conditions. Therefore, differential shrinkage corresponding to the moisture gradient is unlikely the mechanism leading to cracks in the films observed during drying.

The existence of a critical cracking thickness in the films during drying can be explained by a linear elastic fracture mechanics model [13]. Cracking can occur in a stressed thin film only if the strain energy released gained exceeds that invested in forming the crack. The critical cracking thickness is a function of the drying stress and the fracture resistance of the green film. Therefore, *in-situ* measurements of the drying stress can determine its origin as well as provide estimates on the film green strengths.

In this study, sedimentation or flocculation prior to drying were found to be effective in lowering the cracking tendency of ceramic granular films. The latter, however, lowers the dried film green density from 62 to 54 % of theoretical. The lower green density may present problems during sintering. The effect of drying on a nonconstraining substrate was investigated by producing films on a pool of Hg. Crack-free films thicker than 2 mm were produced. A nonconstraining substrate, however, may not provide such benefit in drying large articles. In those cases, self-constraining effects are more important. These can be a result of nonuniform external drying conditions, geometry, and article dimensions.

References

1. T.A. Garino, "Patterning, Drying, and Sintering of Particle Films on Rigid Substrates"; Ph.D. Thesis, Dept. Mat. Sci. Eng., MIT, pp. March 1987.

2. P. Nahass, R.L. Pober, and H.K. Bowen, "Semicontinuous Classification of Ceramic Powders," Ceramics Processing Research Laboratory Report #76, MIT, 1987.

3. T. Ford, Jr. and H.T. Patterson, "A Simple Method for Measuring Solid-Liquid Contact Angles," *J. Colloid Sci.*, **18** 217 (1963).

4. W.B. Haines, "Studies in the Physical Properties of Soils: IV. A Further Contribution to the Theory of Capillary Phenomena in Soil," *J. Agric. Sci.*, **17** 265-290 (1927).

5. T.K. Sherwood, "The Air Drying of Solids," *Trans. AICHE*, **32** [150] 150-168 (1936).

6. E. Beylier, R.L. Pober and M.J. Cima, "Centrifugal Casting of Ceramic Components'; pp.529-36 in Ceramic Powder Science III, Ceramic Transactions, Vol. 12. Edited by G. Messing, S. Hirano, and H. Hausner. American Ceramic Society, Westerville, OH, 1990.

7. R.J. Hunter, Zeta Potential in Colloid Science; pp.27. Academic Press, San Diego, CA (1980).

8. C.J. Brinker and G.W. Scherer, Sol-Gel Science; pp.506. Academic Press, San Diego, CA (1990).

9. A.R. Cooper, "Quantitative Theory of Cracking and Warping During the Drying of Clay Bodies"; pp. 261-76 in Ceramics Processing Before Firing, John Wiley and Sons, New York (1978).

10. E.W. Comings and T.K. Sherwood, "The Drying of Solids. VII Moisture Movement by Capillarity in Drying Granular Materials," *Ind. Eng. Chem.*, **26** 1096 (1934).

11. J.A. Lewis and M.J. Cima, "Diffusivity of Dialkyl Phthalates in Plasticized PVB: Impact on Binder Thermolysis," to be published in *J. Am. Ceram. Soc.*

12. T.M. Shaw, "Drying as an Immiscible Displacement Process with Fluid Counterflow," *Phys. Rev. Lett.*, **59** [15] 1671-1674 (1987).

13. D. Wilkinson and J. Willemsen, "Invasion Percolation: A New Form of Percolation Theory," *J. Phys. A* **16** 3365-3376 (1983).

14. M.S. Hu, M.D. Thoules, and A.G. Evans "Decohesion of Thin Films From Brittle Substrates," *Acta Metall.*, **36** [5] pp.1301-1307 (1988).

15. W. Pietsch, E. Hoffman, and H. Rumpf, "Tensile Strength of Moist Agglomerates," *I & E Prod. Res. and Dev.*, **8** [1] pp.58-62 (1969).

16. S. Sakka, K. Kamiya, K. Makita, and Y. Yamamoto, "Formation of Sheets and Coating Films from Alkoxide Solutions," *J. Noncryst. Solids*, **63** pp.223-235 (1984).

17. I. Strawbridge and P.F. James, "The Factors Affecting the Thickness of Sol-Gel Derived Silica Coatings Prepared by Dipping," *J. Noncryst. Solids*, **86** pp.381-93 (1986).

CHAPTER 4

DRYING STRESS IN GRANULAR CERAMIC FILMS

4.1 Introduction

In the previous chapter, it has been shown that a granular ceramic film will crack during drying when produced above a critical cracking thickness (CCT). This thickness is dependent on the mechanical integrity of the green film as well as the drying stress developed during drying. Measuring this stress will characterize the nature of the stress and the mechanical properties of the film. Various indirect method are possible to allow us to measure average stress in the films *in-situ* during drying. Film dimensions for which a uniform saturation can exist in the film during drying were established for green films in this study. 'Therefore, average stress could be determined as a function of moisture saturation in the film by simultaneously monitoring the weight loss during drying.

A common method for measuring average stress in a film involves measuring the curvature of a substrate on which a film is produced. Optical interference methods are typically used to measure the substrate curvature *in-situ*. The simplest of these methods involve counting and measuring the relative

positions of the interference rings (Newton's rings) generated by the displacement between the sample and an optical flat when viewed under a monochromatic light source [1]. Each interference ring represents an additional constant amount of displacement of one-half the wavelength of the light source. The curvature can be calculated form the displacement versus position data. This technique is valid as long as the number of interference fringes is less than approximately 20 [1]. From the curvature, the stress in the film can be determined by [2]

$$\sigma = \frac{E t_s^3}{6(1-\nu) R t_f^2 (1 - t_s/t_f)} \qquad 4.1$$

where E and υ are the Young's modulus and the Poisson ratio of the substrate, respectively, t_s is the substrate thickness, and R is the radius of curvature of the substrate. The above equation holds as long as the Young's modulus of the substrate is much greater than that of the film.

4.2 Experimental Procedure

The ceramic particulate films used in this study were made from aqueous dispersions of α-alumina and α-quartz. The average particle sizes of the Sumitomo alumina powders were 0.4 μm (AKP-30) and 0.65 μm (AKP15) as reported by the manufacturer. The particulate suspensions were stabilized by adjusting the pH of the dispersions to 3.7 with nitric acid followed by ultrasonication and readjustment of the pH to 3.5. Centrifugally classified Reynolds alumina having particle size between 0.3 - 0.5 μm were also used. The

silica powder were also centrifugally classified to obtain particles in the with average particle sizes of 0.8 μm and 1.1 μm. The average particle size and size distribution for all the powders were measured using a light scattering technique (Horiba CAPA 500). Transmission electron microscopy (TEM) was used to examine the AKP30 and classified Reynolds alumina powder.

Films were cast onto (001) silicon substrates of 100 or 130 μm thickness for stress measurements. As received, the Si substrates (Virgina Semiconductor, Fredricksburg, VA) were 2 in. in diameter and were flat to 3 μm. These were cut into rectangular pieces of various sizes. The appropriate substrate thickness was selected to maximize the sensitivity for the stress range measured. For instance, the appropriate substrate thickness would be the one which yields approximately 20 rings at the highest level of stress measured. The elastic constants for specific orientations of single crystal silicon can be calculated from known stiffnesses and compliances for the single crystal material. The (001) silicon substrate used in this study had a Young's modulus of 1.689×10^{11} Pa and a Poisson ratio of 0.064 [3].

A schematic of the experimental setup for stress measurement is shown in Figure 4.1. The film was cast onto a silicon substrate on an optical flat which was hung from an analytical balance (Mettler AE160). The weight loss during drying was recorded through an interface to a personal computer. Monochromatic light of 0.5461 μm was used to generate interference patterns between the reflective back side of the silicon substrate and the optical flat. Changes in the interference patterns during drying were captured in real time using a video camera and video recorder while simultaneously recording the weight. The desired frames of the

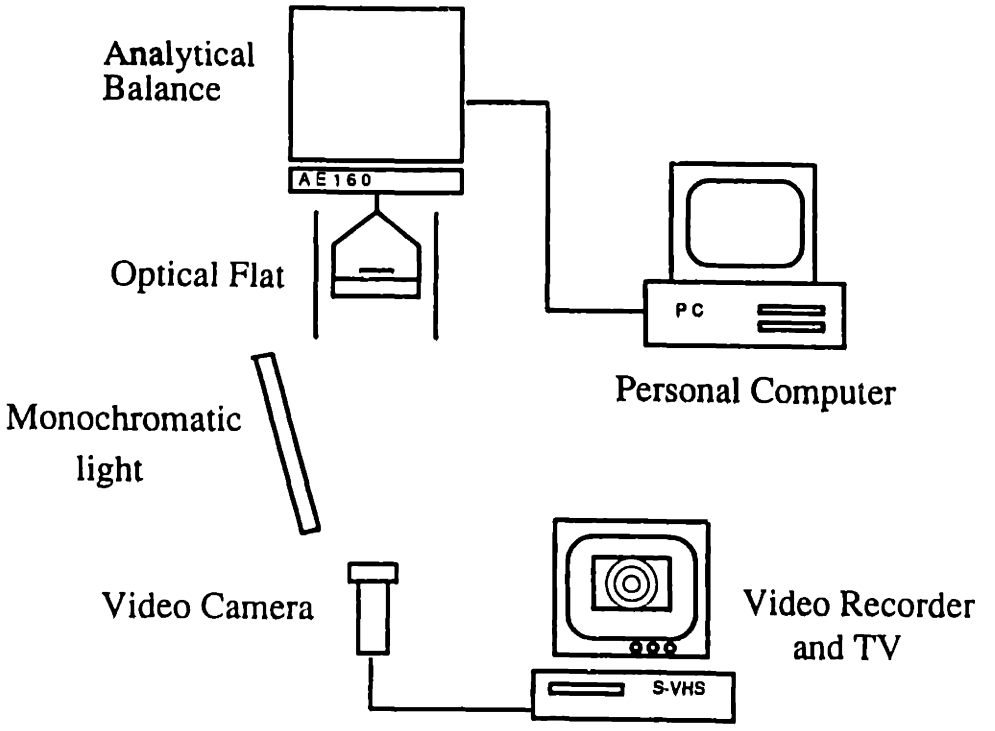

Figure 4.1. Schematic of experiment setup used for *in-situ* stress measurement.

video recording were captured by a video frame digitizer for processing after the completion of drying. The details on the computer program used to gather the fringe positions are given in Appendix 1.

The curvature of the substrate was determined at selected time intervals by analyzing the positions and number of fringes in the digitized image. The average stress in the film was calculated from the curvature at different times during drying. Since even a small air current could disrupt the mass measurements, a shield was placed around the setup to minimize disturbance. For the same reason, ambient conditions were not controlled but were monitored using a solid-state hygrometer and a thermocouple.

The green densities of the dried films were determined by mercury porosimetry. The samples were obtained by mechanically removing dried films cast onto glass substrates.

4.3 Results

Shown in Figures 4.2 a-d is a sequence of photos of a 40 μm film produced from 0.4 μm particle size AKP30 alumina slip on a 12 x 12 mm^2 glass substrate. Note that the supersaturated region retreats uniformly from the edges, leaving only the saturated region behind. Figure 4.3 shows a plot of the diameter of the super-saturated region as a function of time. In Figure 4.4, the weight loss data for a similar film dried under the same condition but was cast onto a 12 mm x 12 mm silicon substrate is plotted. The diamond indicated the time when the shrinking

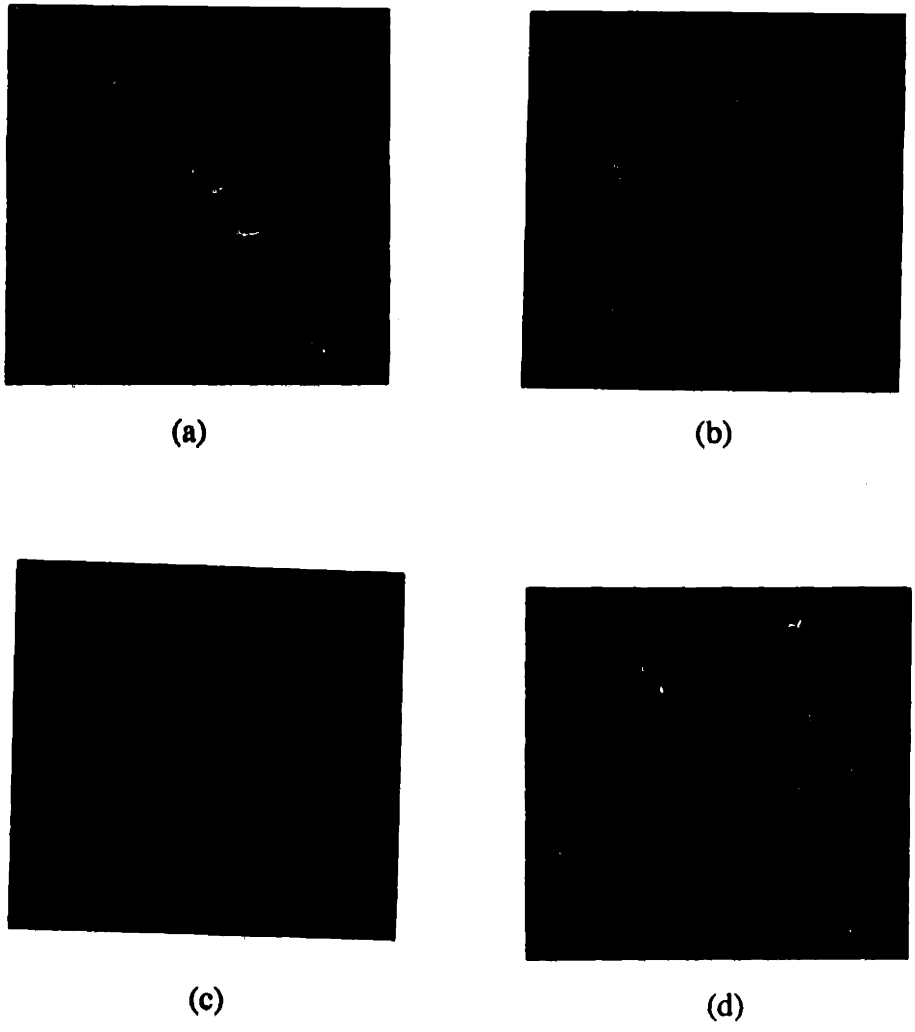

Figure 4.2. **Photographs of a drying film produced from 0.4 μm particles and cast onto 12 X 12 mm² glass substrate. Note that the supersaturated region shrunk symmetrically from the substrate edge.**

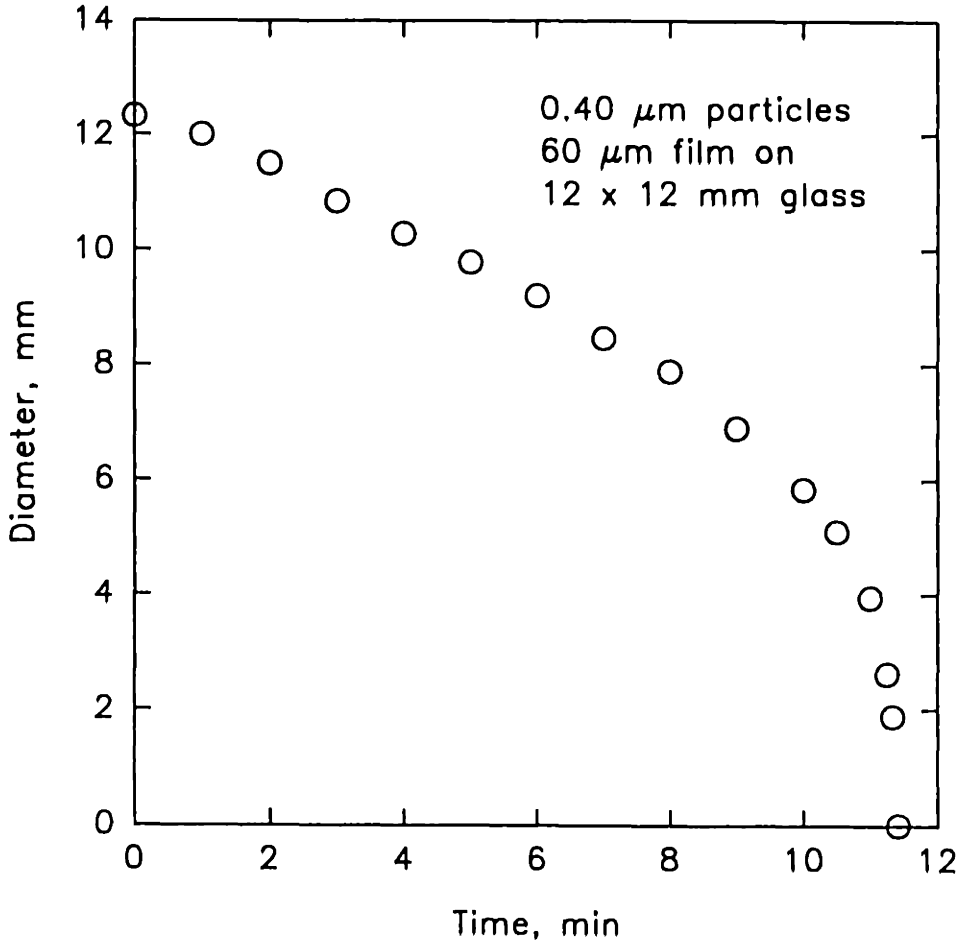

Figure 4.3. **Plot of the diameter of the supersaturated region as a function of time for the film shown in Figure 4.2.**

supersaturated region became extinct. Note that the rate of weight loss was approximately constant until only a small amount of liquid was left.

Shown in Figure 4.5 is the weight loss data for a 60 μm film produced from the 0.4 μm particle size AKP30 alumina slip and cast onto 12 x 12 mm^2, 130 μm Si substrate. The supersaturated region was observed to retreat symmetrically from the edges during drying, similar to the experiment on the glass substrate. The stress history for the same film as in Figure 4.5 is shown in Figure 4.6. The drying rate in this experiment was found to be 1.2 x 10^{-4} kg/m^2-s. Note that the tensile stress which developed in the film rapidly increased to nearly 1.3 MPa and decreased thereafter. The error in the stress measurements is approximately 50 kPa, which is largely from subtracting the initial curvature of the substrate. Also note that zero stress was detected until 2 minutes before the supersaturated region became extinct when the stress increased. The stress started to develop nearly 10 minutes before the extinction of the supersaturated region when a film of the same thickness was dried on a larger substrate, as shown in Figure 4.7. The drying film did not develop any stress until after the supersaturated region became extinct by slowing down the drying rate by a factor of ~20 and using a smaller substrate. The observed stress maximum is over 1.8 MPa (Figures 4.8 and 4.9). The shape of the stress history and the stress maximum was found to be independent of the film thickness. But a residual stress was found in some of the dried films.

In Figure 4.10, the stress history of a 40 μm thick film produced from 0.4 μm alumina particles dried under changing external evaporation rate is shown. The initial drying rate was 5 x 10^{-5} kg/m^2-s. The drying rate was reduced to 6 x 10^{-6}

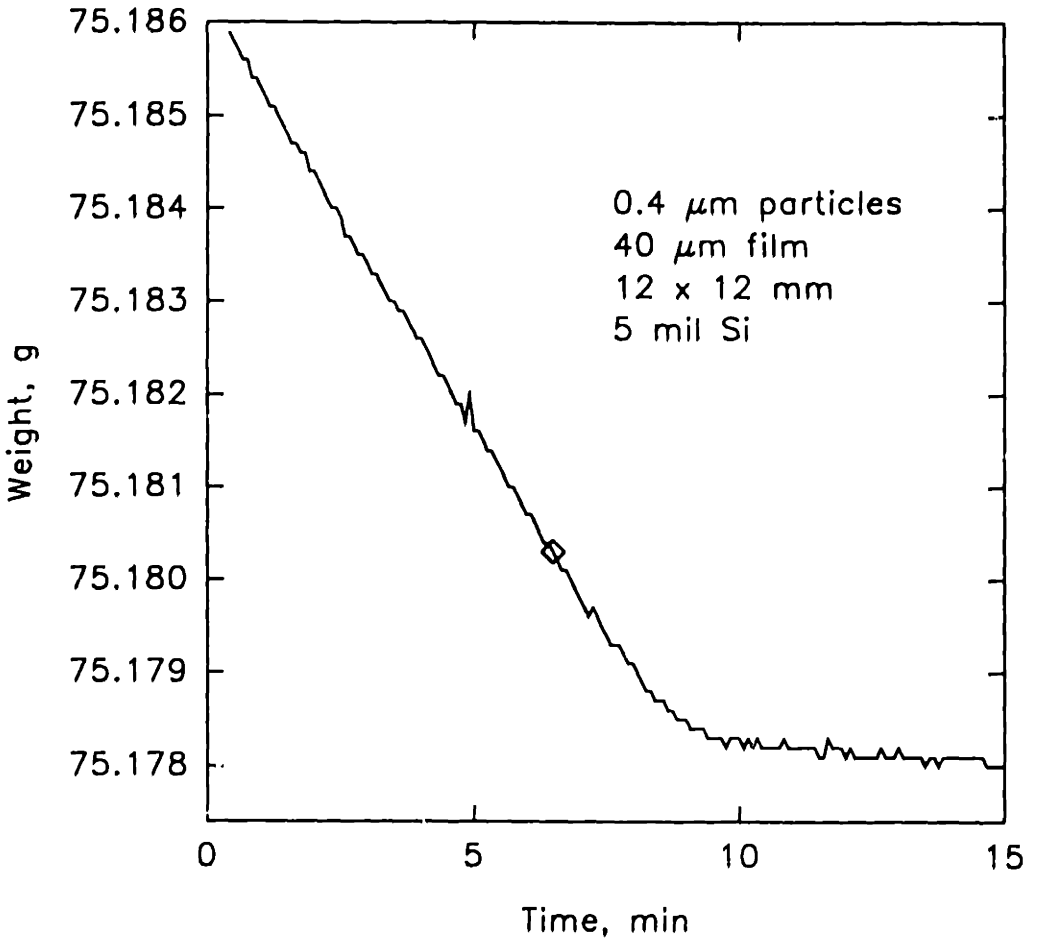

Figure 4.4. Weight loss data for a 40 μm thick film produced from 0.4 μm alumina particles cast onto a 12 X 12 mm^2 silicon substrate.

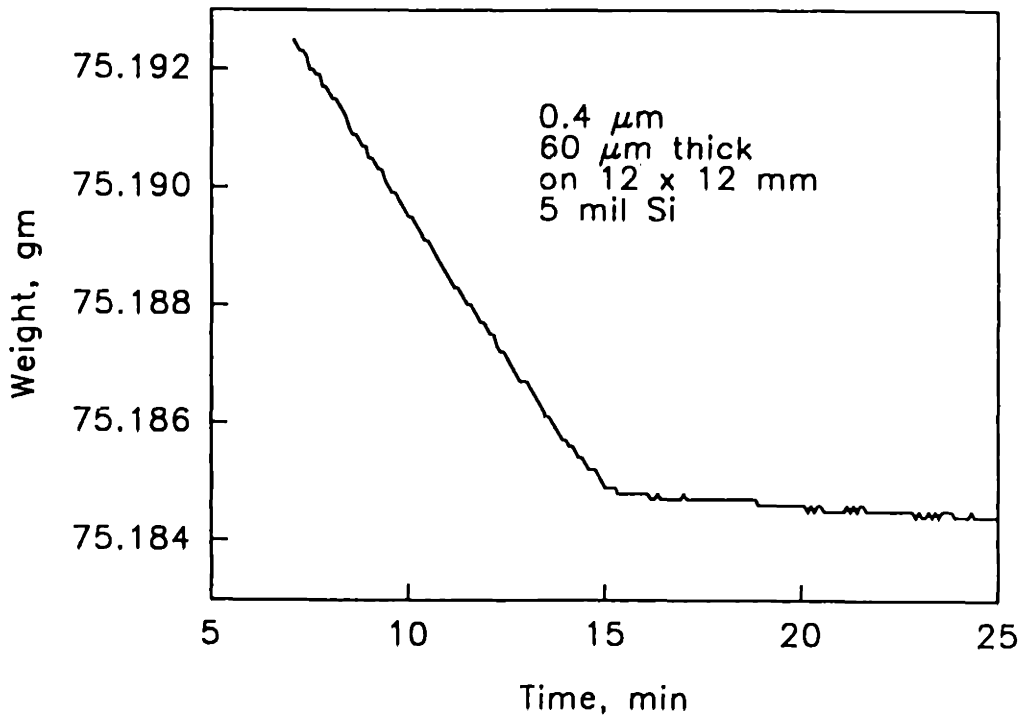

Figure 4.5. **Weight loss data for a 60 μm thick film produced from 0.4 μm alumina particles cast onto a 12 X 12 mm^2 silicon substrate. The drying rate was 1.2 x 10^{-4} kg/m^2-s.**

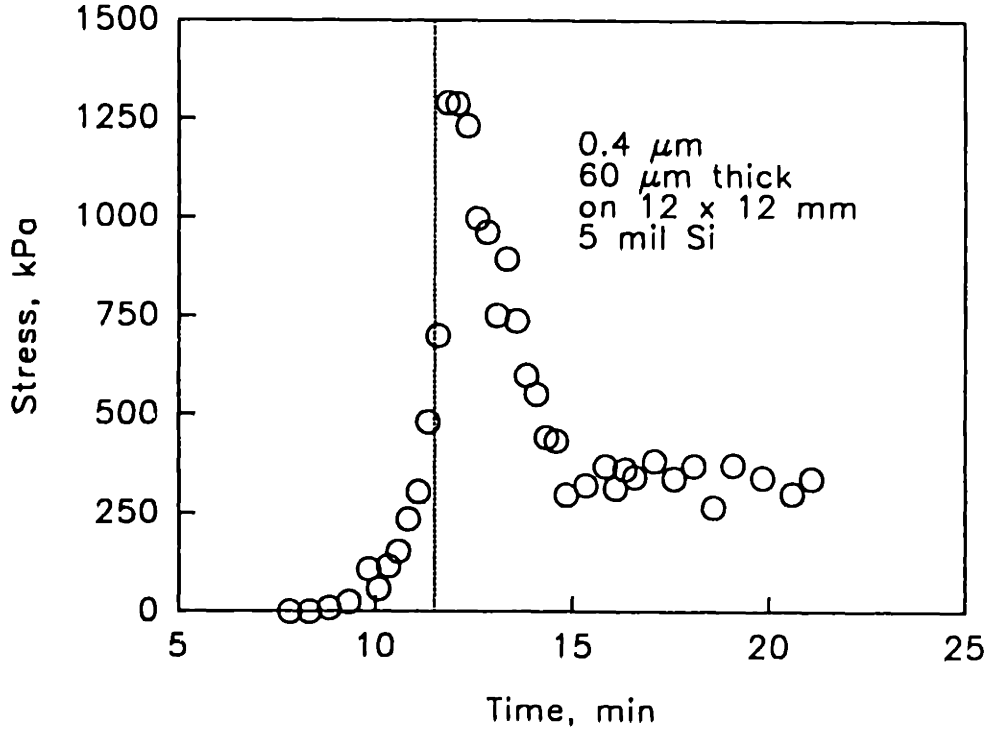

Figure 4.6. **Stress history of the same film described in Figure 4.5. The dashed vertical line indicates the moment when the supersaturated region became extinct.**

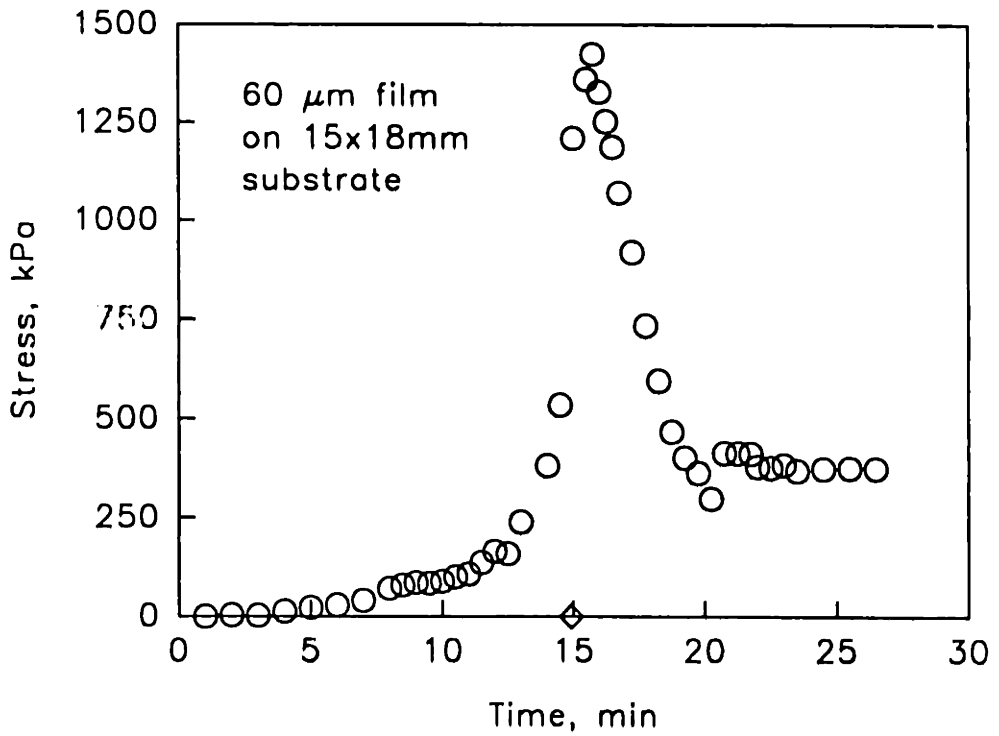

Figure 4.7. **Stress history of a 60 μm thick film produced from 0.4 μm alumina particles cast onto a 15 X 18 mm² silicon substrate. The drying rate was 1.2 x 10^{-4} kg/m²-s.**

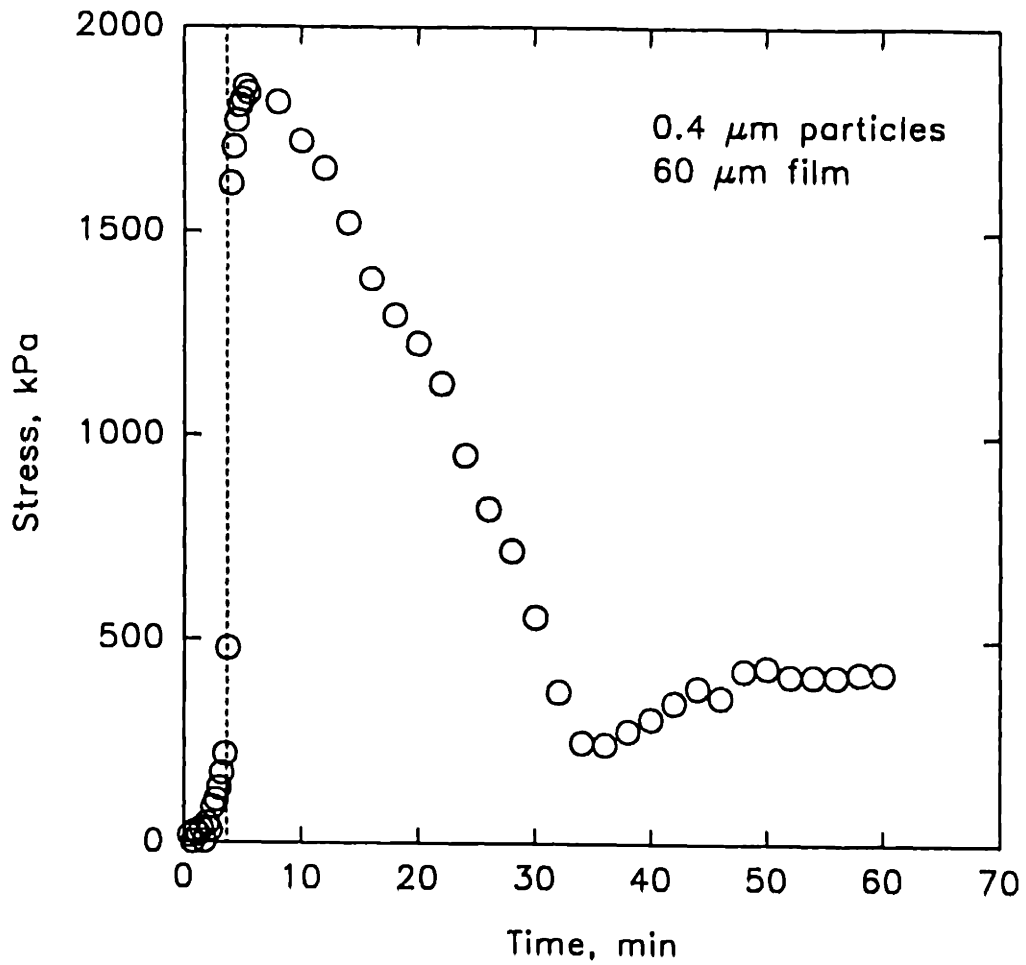

Figure 4.8. **Stress history of a 60 μm thick film produced from 0.4 μm AKP30 alumina particles cast onto a 9 X 9 mm² substrate. The drying rate was 7.2 x 10^{-6} kg/m²-s.**

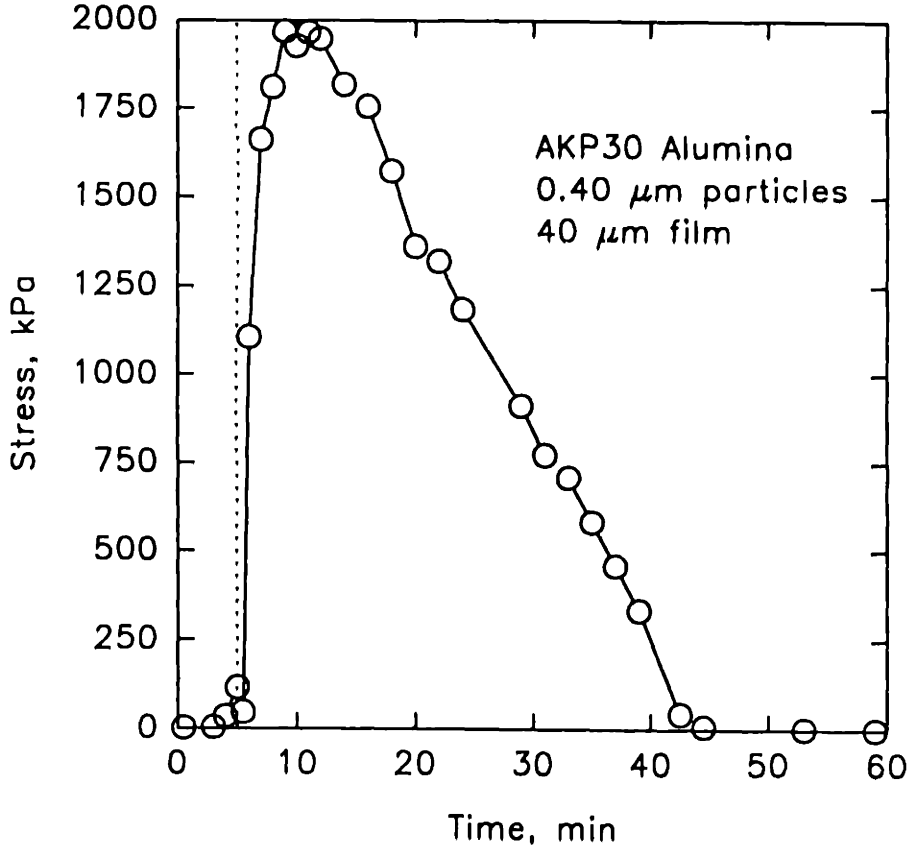

Figure 4.9. **Stress history of a 40 μm thick film produced from 0.4 μm AKP30 alumina particles cast onto a 9 x 9 mm^2 substrate. The drying rate was 7.2 x 10^{-6} kg/m^2-s. Note that the film does not have a residual stress.**

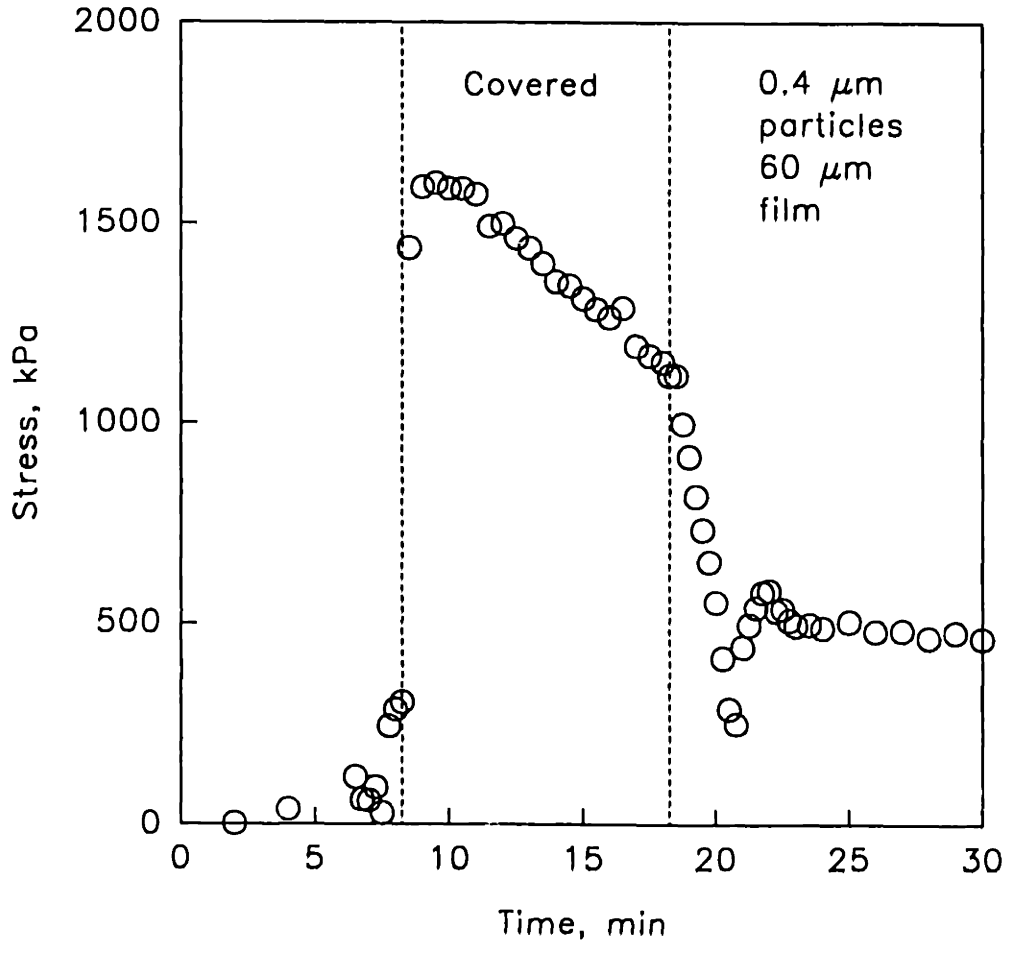

Figure 4.10. Stress history of a 40 μm thick film produced from 0.4 μm AKP30 alumina particles dried under changing external conditions. The drying rate was changed from 5 x 10^{-5} kg/m^2-s to 7.2 x 10^{-7} g/cm^2-s in the time between the two vertical dash lines.

kg/m^2-s immediately following the supersaturated region became extinct. At some later point, the rate was increased back to the initial value. Note the as soon as the drying rate was lowered the stress decreased less rapidly with time than when the drying rate was increased again.

The stress history of alumina films produced from 0.65 μm average particle size alumina at two different drying rates are shown in Figures 4.11 and 4.12. No stress was observed until the supersaturated region became extinct similar to the 0.4 μm particle size films. The maximum stress for the slow dried film was approximately 1.0 MPa.

In Figure 4.13, the stress history of a film produced from 0.4 μm particle size AKP30 alumina slip with 0.005 wt% surfactant added is shown. Note that the stress maximum is lowered to 0.9 MPa as compared to ones without surfactant addition. In Figure 4.14, the stress history of a 30 μm thick film produced from 0.4 μm particle size Reynolds alumina slip is shown. The behavior was similar to the ones produced from the AKP30 powder but the stress maximum was higher at 2.15 MPa. In Figure 4.15 and 4.16, stress history for films produced from 0.8 and 1.1 μm average particle size silica slips are shown, respectively. The 0.8 μm particle size silica film cracked during drying. The arrow indicated the point when cracking occurred.

On Table 4.1, a summary of the pertinent results are presented. The average particle sizes are determined by light scattering method. The dried green density is obtained from mercury porosimetry. The particle size distributions of the powders are shown in Figures 4.17 - 4.21. The green density of the films in

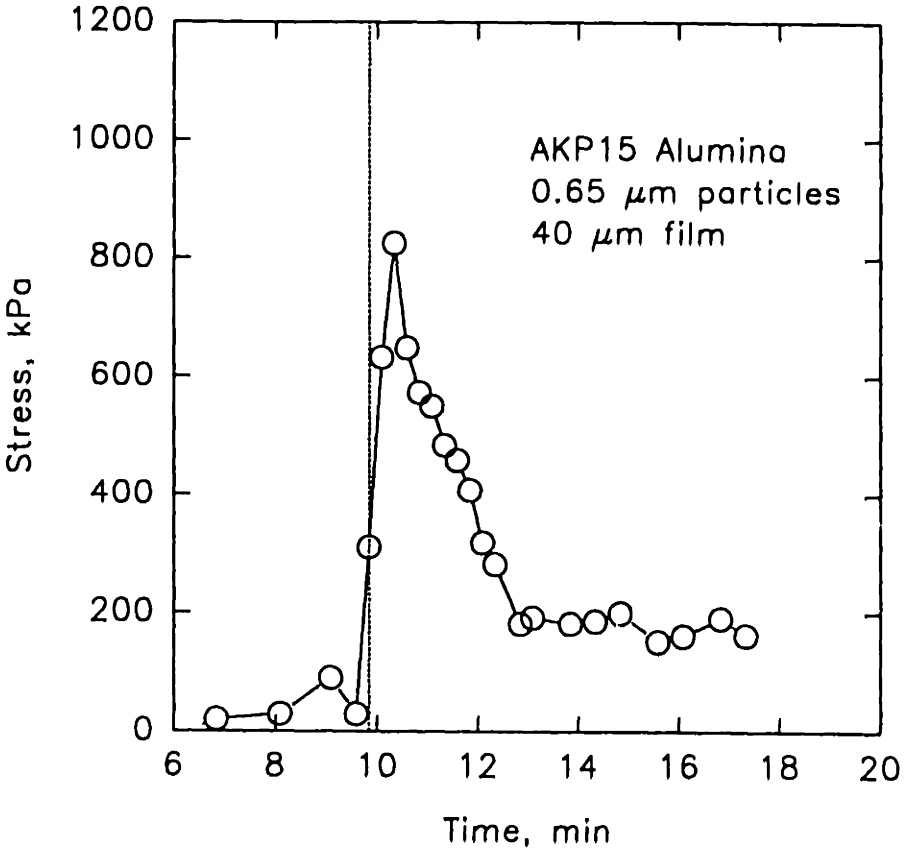

Figure 4.11. **Stress history of a 60 μm thick film produced from 0.65 μm AKP15 alumina particles cast onto a 9 x 9 mm² silicon substrate dried at a rate of 1.2 x 10^{-4} kg/m²-s.**

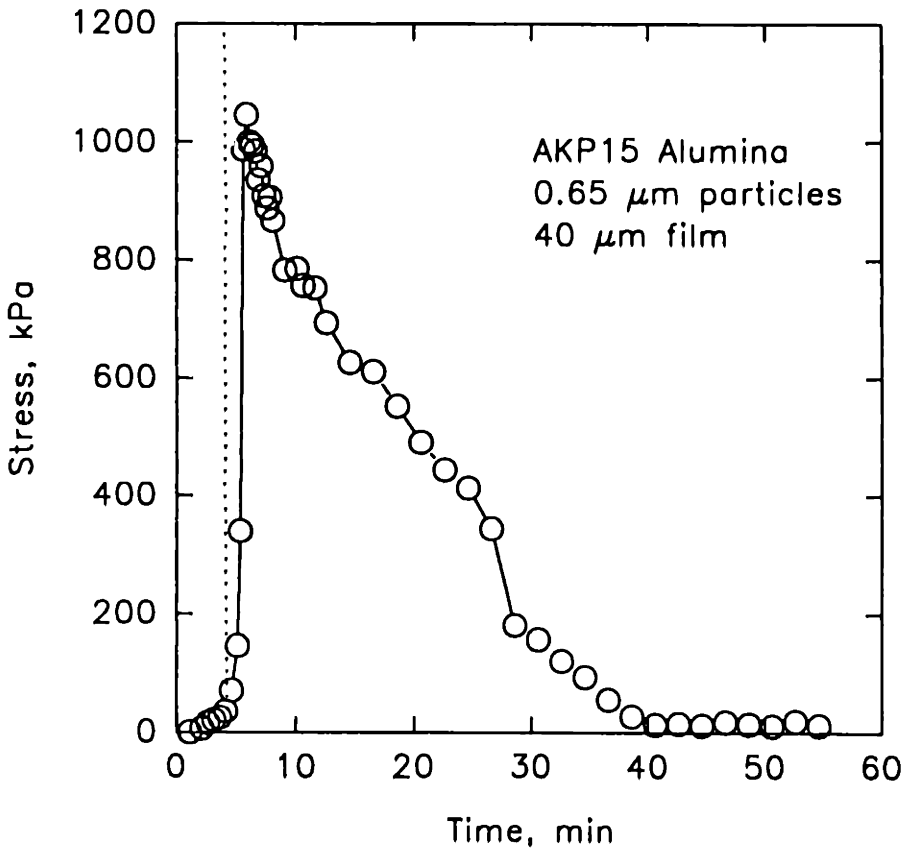

Figure 4.12. Stress history of a similar film as shown in Figure 4.10 but dried at 7.2 x 10^{-6} kg/m^2-s.

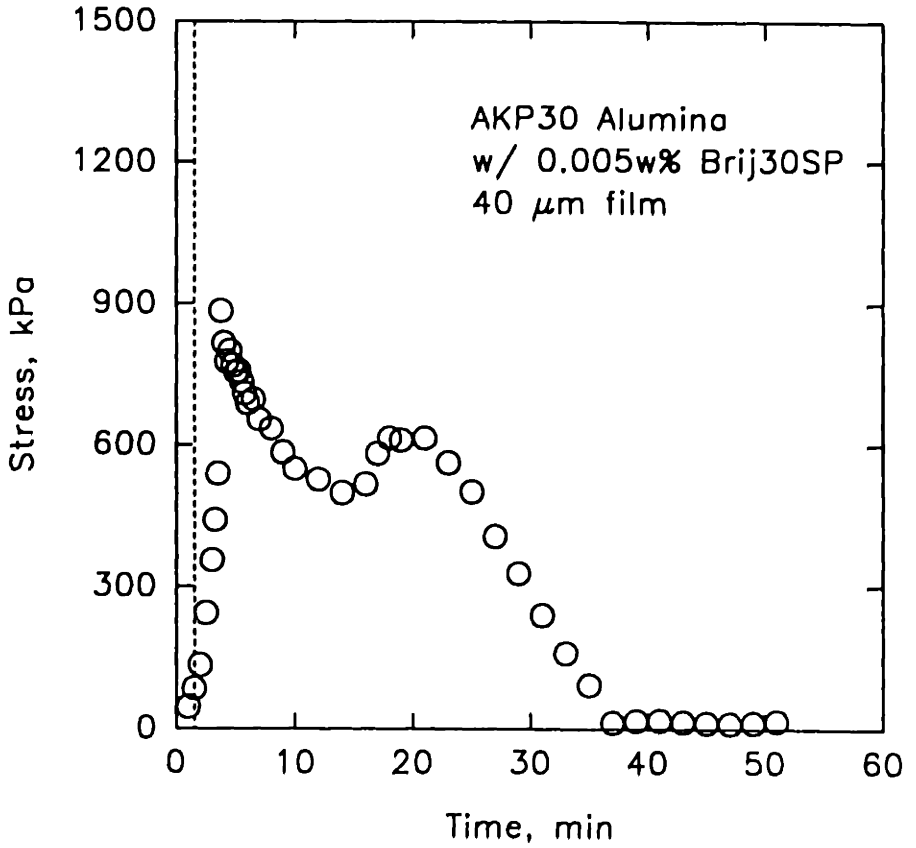

Figure 4.13. Stress history of a 40 μm thick film produced from 0.4 μm AKP30 alumina particles cast onto a 9 x 9 mm² silicon substrate. The surface tension of the water was lowered from 72 to 32 dyne/cm.

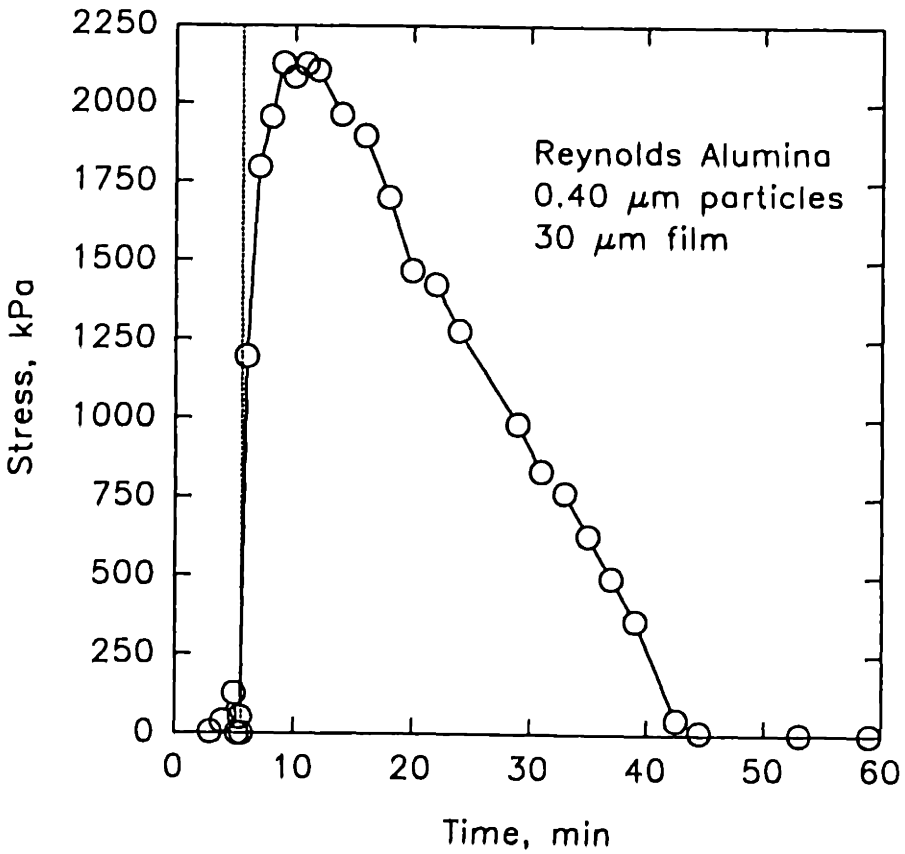

Figure 4.14. Stress history of a 30 μm thick film produced from 0.4 μm Reynolds alumina particles cast onto a 9 x 9 mm^2 silicon substrate. The drying rate was 7.2 x 10^{-6} kg/m^2-s.

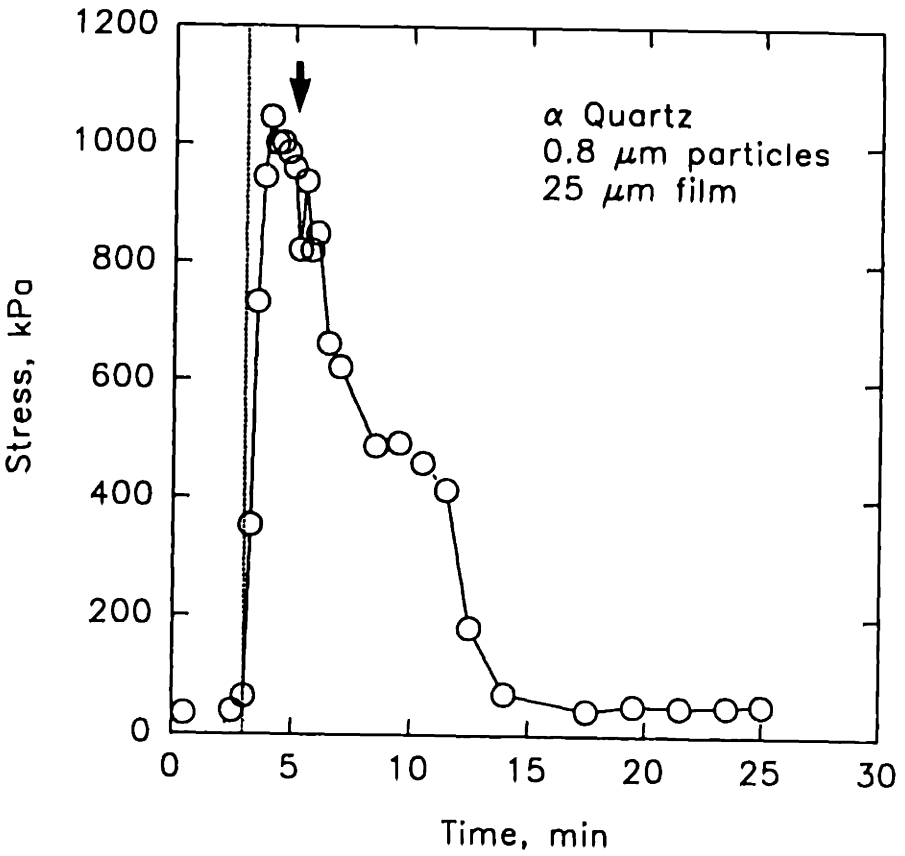

Figure 4.15. Stress history of a 40 μm thick film produced from 0.8 μm silica particles cast onto a 9 x 9 mm^2 silicon substrate. The drying rate was 7.2 x 10^{-6} kg/m^2-s. The arrow indicated the moment when the film cracked.

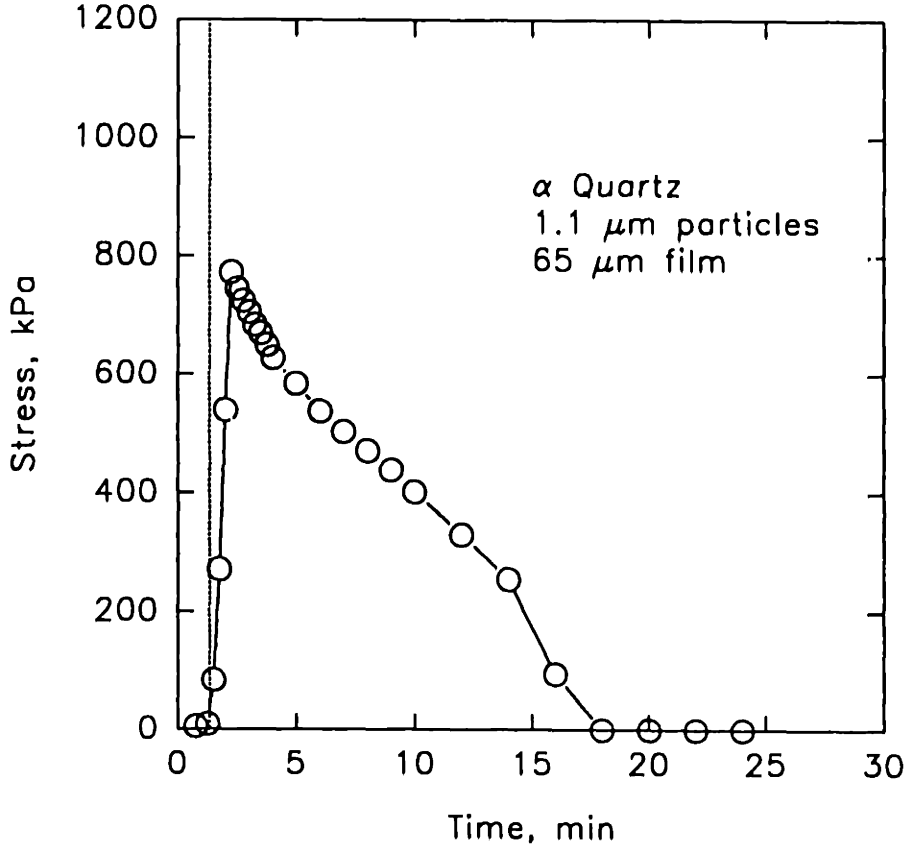

Figure 4.16. Stress history of a 40 μm thick film produced from 1.1 μm silica particles cast onto a 9 x 9 mm^2 silicon substrate. The drying rate was 7.2 x 10^{-6} kg/m^2-s.

Table 4.1 - Summary of results.

Powder	Particle Size (μm)	Film Thick. (μm)	Drying Rate (kg/m^2-s)	σ_{max} (MPa)	ρ_{dried} (%)	ρ_{wet} (%)	Rise Time(sec)	σ_{res} (MPa)
AKP30	0.35	40	$6x10^{-6}$	1.8	62	57	150	0
AKP30	0.35	40	$6x10^{-6}$	1.95	--	57	180	0.4
AKP30	0.35	60	$6x10^{-6}$	1.8	--	57	180	0.4
AKP30	0.35	40	$1.2x10^{-4}$	1.45	--	--	30	0.2
AKP30	0.35	60	$1.2x10^{-4}$	1.3	--	--	30	0.4
AKP30#	0.35	40	$6x10^{-6}$	0.9	--	--	120	0
AKP30#	0.35	60	$1.2x10^{-4}$	0.9	--	--	30	0.2
AKP15	0.68	40	$6x10^{-6}$	1.05	62	60	60	0
AKP15	0.68	40	$1.2x10^{-4}$	0.8	--	--	30	0.2
AKP15	0.68	60	$1.2x10^{-4}$	0.8	--	--	30	0.2
AKP15	0.68	90	$1.2x10^{-4}$	0.8	--	--	60	0.2
Reynolds	0.35	30	$6x10^{-6}$	2.15	66	60	210	0
α-Quartz	0.8	25	$3x10^{-5}$	1.05	--	--	60	0
α-Quartz	1.1	65	$3x10^{-5}$	0.8	--	52	60	0

- liquid surface tension lowered to 32 dyne/cm by adding 0.005 wt% Brij 30SP.

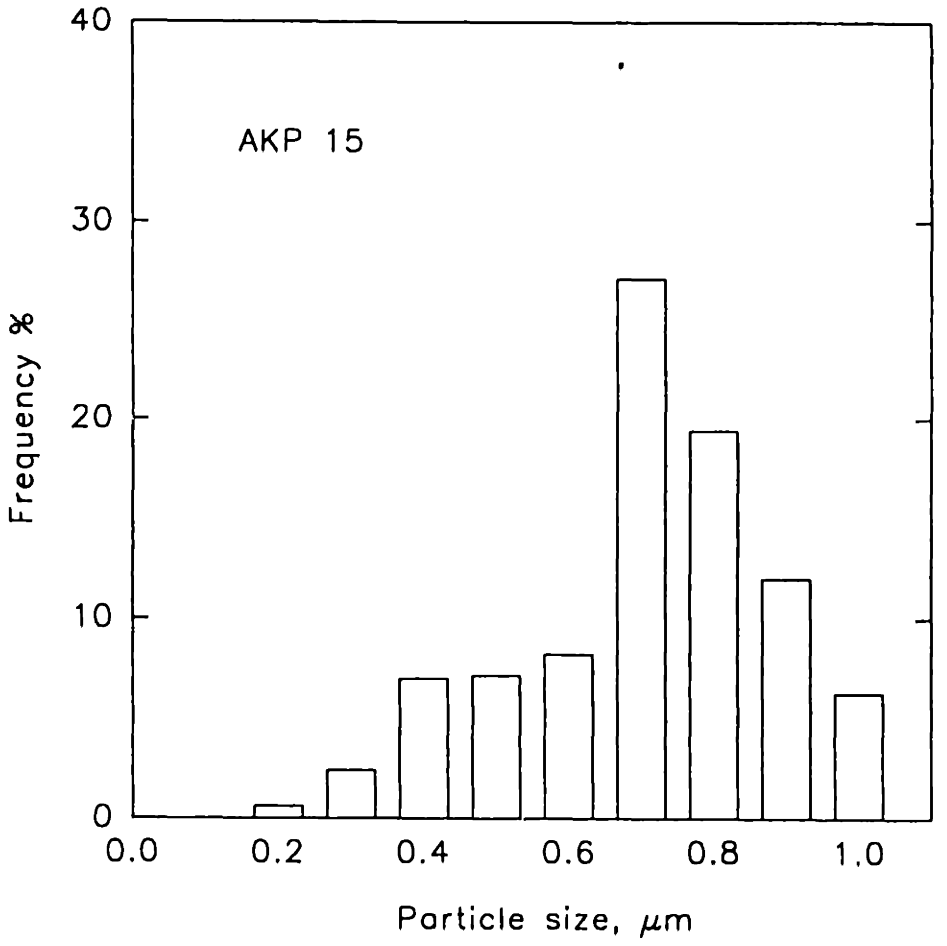

Figure 4.17. Particle size distribution (calculated by area) of AKP15 alumina.

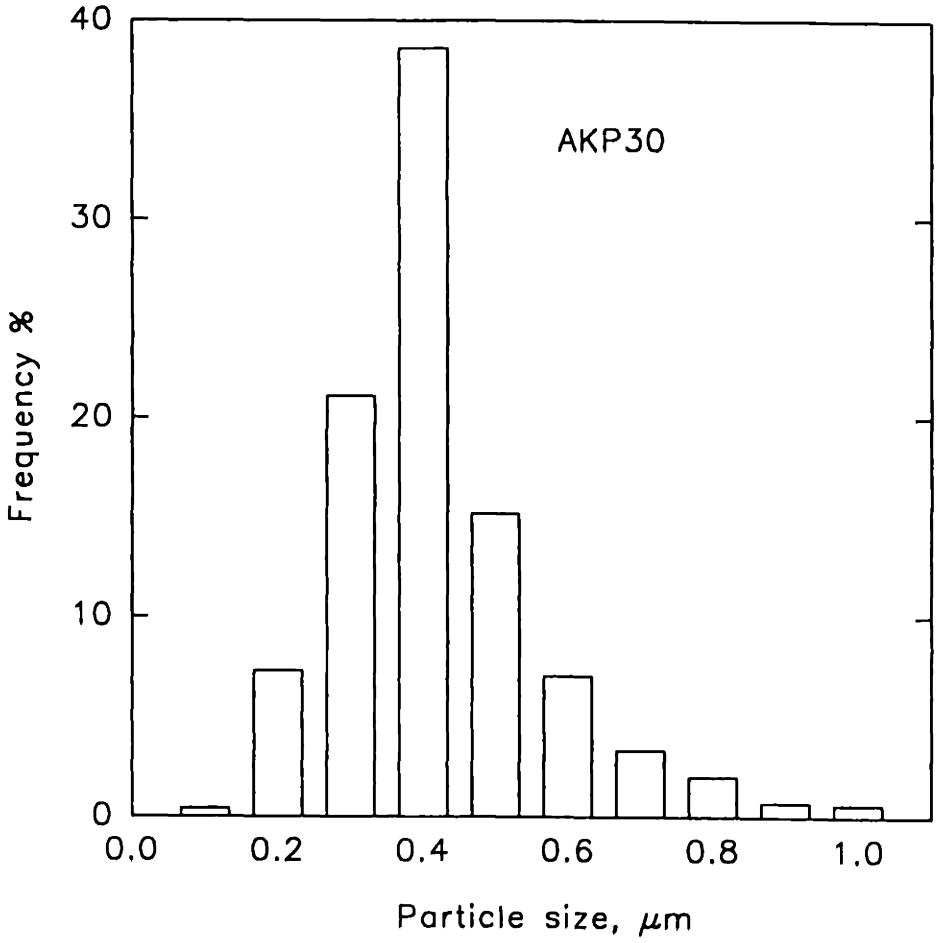

Figure 4.18. Particle size distribution (calculated by area) of AKP30 alumina.

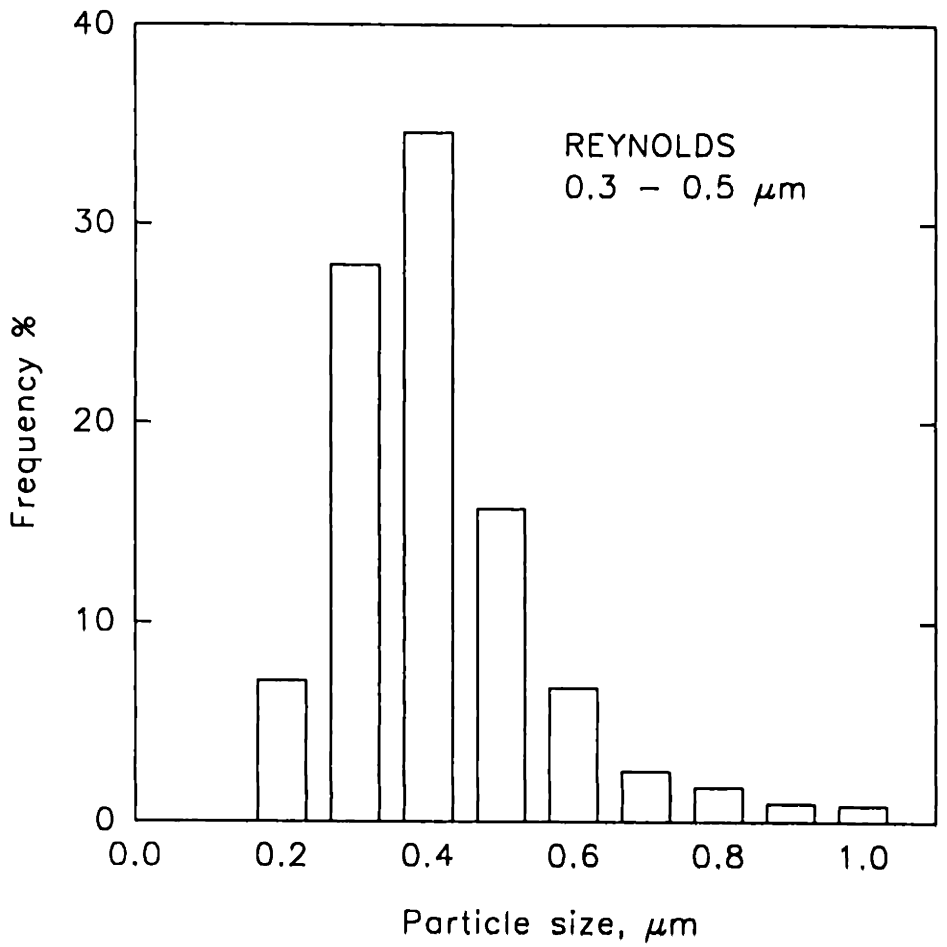

Figure 4.19. Particle size distribution (calculated by area) of the 0.3 - 0.5 μm cut of the classified Reynolds alumina.

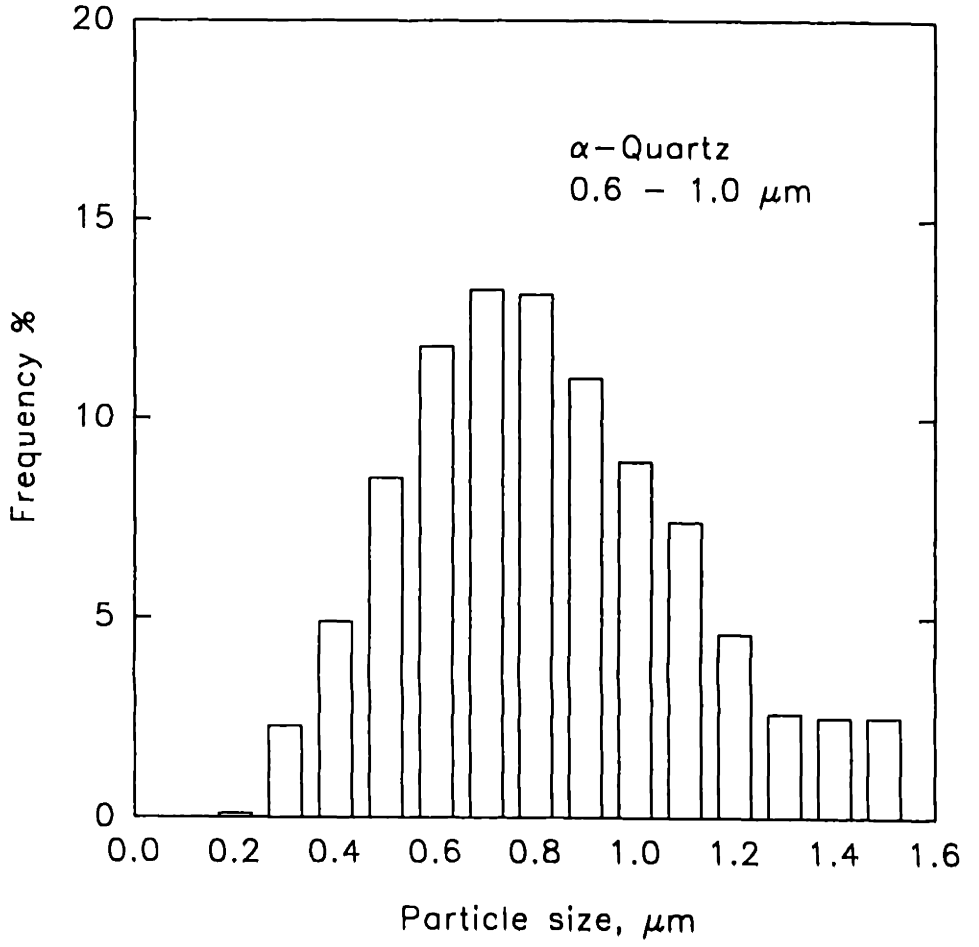

Figure 4.20. Particle size distribution (calculated by area) of the 0.6 - 1.0 μm cut of the classified α-quartz.

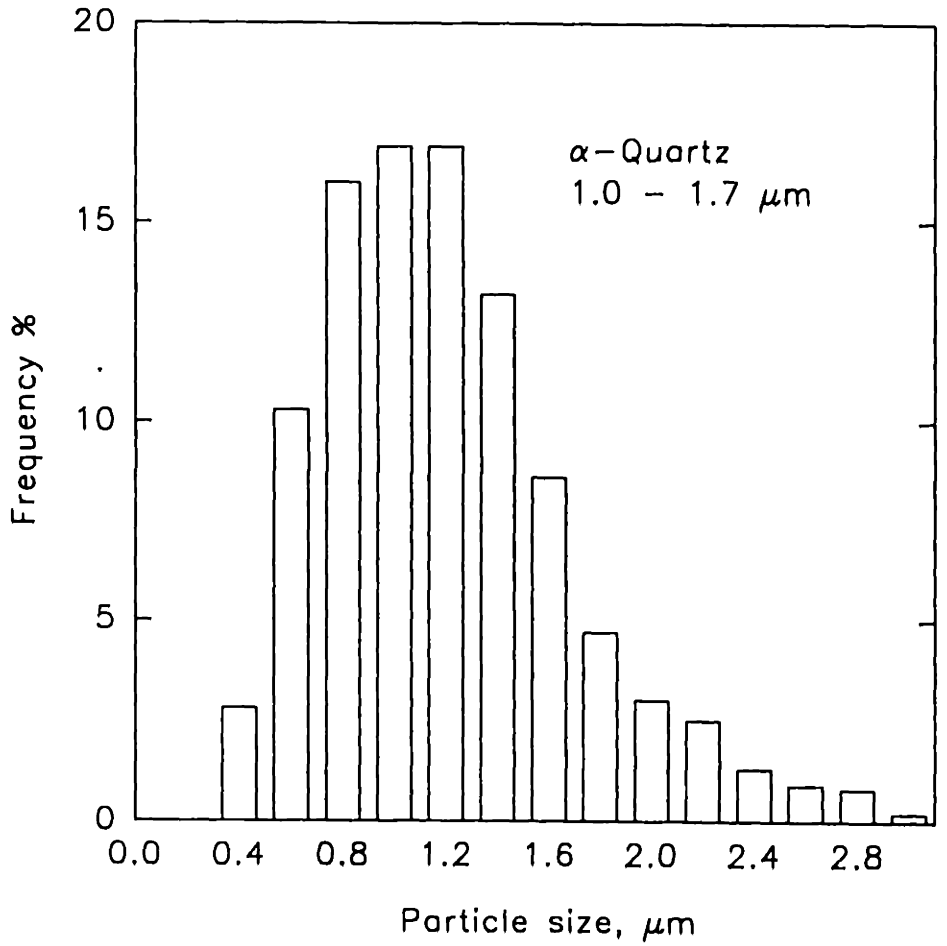

Figure 4.21. Particle size distribution (calculated by area) of the 1.0 - 1.7 μm cut of the classified α-quartz.

the saturated state is determined from the dried film weight and the weight loss from the moment when the supersaturated region became extinct to dryness. The stress rise time is the time elapsed between supersaturation extinction and the stress maximum.

Cracking occurred in the film when it is produced above the critical cracking thickness as described in the last chapter. The development of cracks could be detected by a sudden abnormal distortion of the optical interference pattern. The approximate saturation when cracking occurred was then obtained from the weight loss data. At drying rates greater than 1 x 10^{-4} kg/m^2-sec cracking always occurred just beyond the stress maximum. When the drying rate is drastically lowered to 6 x 10^{-6} kg/m^2-s, cracking occurred at approximately 20 - 30 % saturation for two out of the three films produced; one did not crack.

4.4 Discussion

4.4.1 Saturation Uniformity

During the drying of a granular film, the evaporative flux in the saturated region is supplied by liquid wicked from the supersaturated region. The length scale for which this wicking occurs can be estimated by Equation 3.1. If a film were produced with dimensions less than the predicted saturated region length, the film would be uniformly saturated when the supersaturated region disappears. In this study, the stress measurements were made with films having substrate dimensions less than 15 x 18 mm^2. A constant drying rate was typically observed

until only a small amount of liquid remained in a film, as shown in Figure 4.5. The predicted dimensions of the saturated region using Equation 3.1 is approximately 10 mm for the current drying conditions. Therefore, the films should be uniformly saturated from the time when the supersaturated region disappears. If we assume that a film is 100% saturated when the wet front became extinct, the weight loss data can be converted to saturation from the dried film weight. For example, the stress history for the film shown in Figure 4.8 is converted to plot versus saturation in Figure 4.22.

For films cast on a large substrate, the flow of liquid from the supersaturated region to the edge of the film will begin to cease before the supersaturated region disappears, as predicted by Equation 3.1. Pores in the edge will then begin to empty first. Stress can then develop in that region while the center of the film is still fluid. This is illustrated in the stress history of the drying film on the 15 x 18 mm^2 substrate as shown in Figure 4.7. High uniformity in moisture saturation of the film during drying can be ensure by reducing drying rate and substrate dimensions. In this case, no stress was found to develop until the wet front became extinct for a film made on a 9 x 9 mm^2 substrate as shown in Figure 4.9.

4.4.2 Origin of Stress

For all the stress history curves, the stress reached a maximum at some point early during drying and decreased monotonically thereafter. The stress maximums for films produced from various powders are listed. In all cases, the

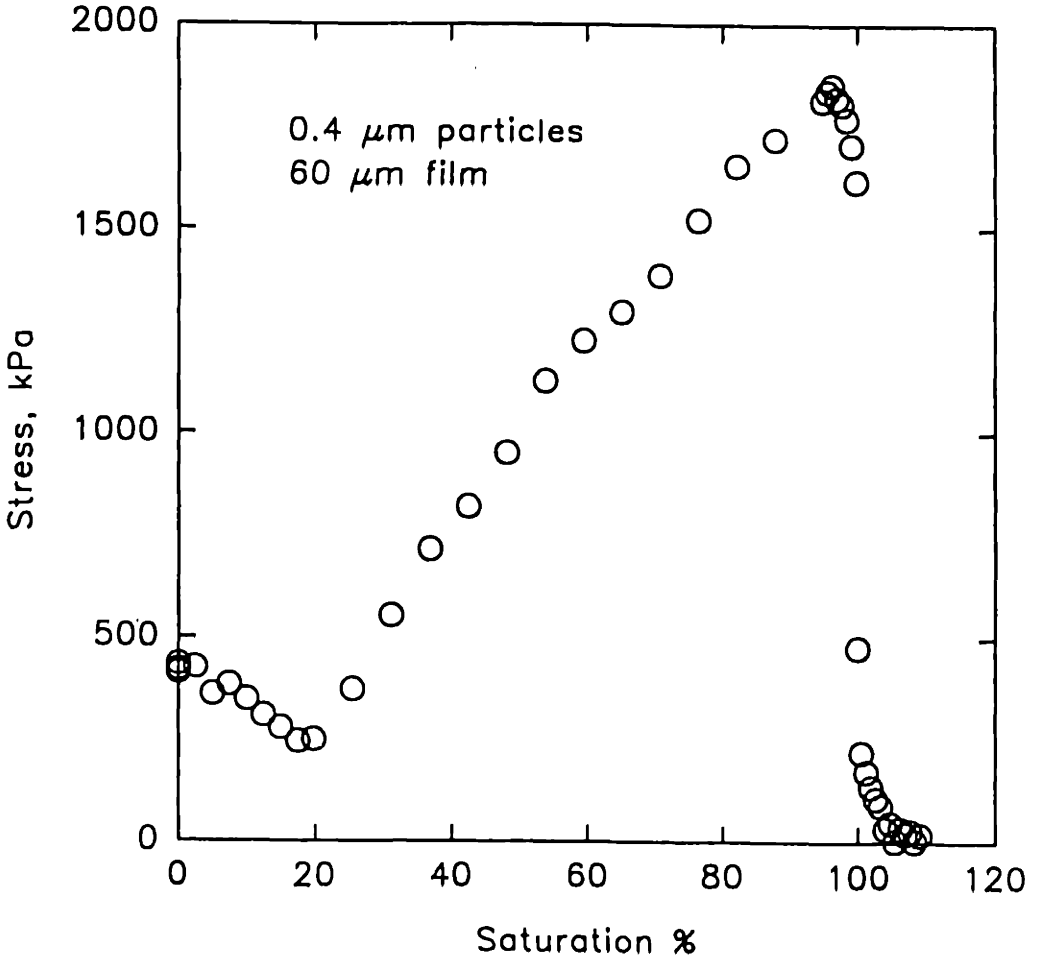

Figure 4.22. Stress history of a drying film as described in Figure 4.8, but plotted as a function of saturation.

stress maximum showed inversely proportional dependence on the particle size of the granular films, indicating a capillary pressure origin for the stress. For example, the ratio of the stress maximum values for the AKP30 and AKP15 alumina is 1.8 while the ratio of their particle size is 1.9. In the case of the films with surfactant addition, the surface tension of the liquid was lowered from 72 to 32 dyne/cm while the stress maximum was lowered from 1.85 to 0.9 MPa. This behavior was also consistent with the capillary nature of the stress.

For similar particle size and size distribution, films produced from the Reynolds powder were found to have a significantly higher maximum stress than those from the AKP30 powder. But since the green density of the Reynolds alumina film was also found to be higher than those of the AKP30 alumina (see previous chapter), this behavior was not surprising. This higher packing characteristics of the Reynolds powder was found to be a result of a high equiaxial geometry in particle morphology, as shown in the TEM micrographs of the two powders (Figures 4.23 and 4.24). To assure that particle size distribution and/or the classification procedure were not the source of the packing characteristics, a batch of the AKP30 powder was centrifugally classified using the same procedure for treating Reynolds powder. The resulting green films produced from the classified AKP30 powder, however, still had a lower dried green density than that from the Reynolds powder.

Prior to the point when the supersaturated region becomes extinct, the pores in the saturated region are completely filled with liquid and drying is maintained by wicking liquid from the supersaturated region. In this state, the particles

Figure 4.23. TEM micrograph of the 0.4 μm AKP30 alumina particles.

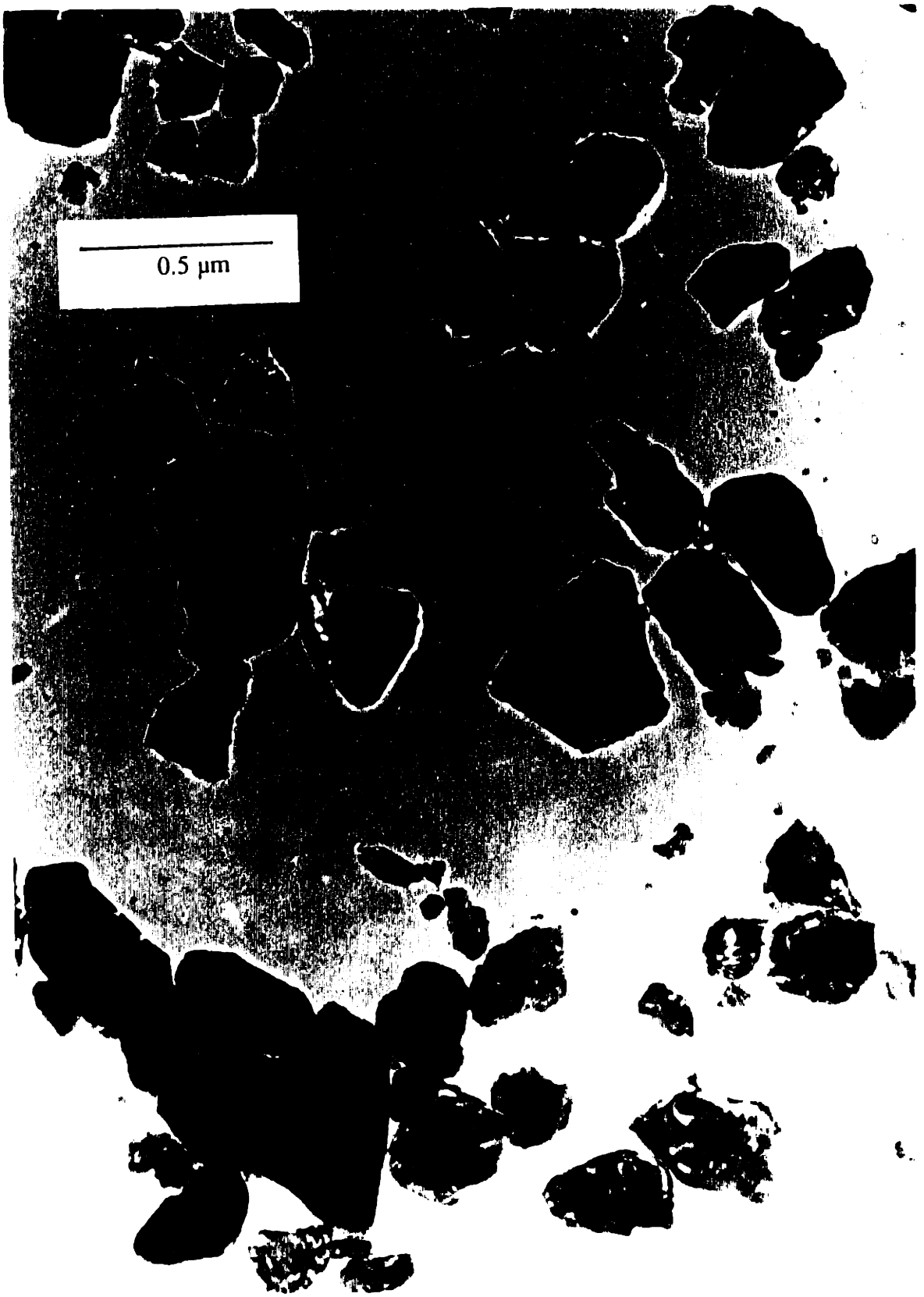

Figure 4.24. TEM micrograph of the 0.4 μm Reynolds alumina particles.

presumably were still separated by a repulsive electrostatic layer. When the supersaturated region becomes extinct, further removal of liquid requires the pores to drain or the liquid between the particles to be removed. Whether all the liquid between the particles will be removed prior to pores draining will depend on the relative magnitude of the force separating the particles and the capillary force. An equivalent situation would be looking at the amount of elastic deformation that occurs when an assembly of colloidal particles having some elastic properties determined by the interaction potential between the particles is subject to an externally applied stress having the same magnitude as the capillary stress.

Van Meeken and Snook [4] provided some estimates on elastic properties of model colloids in a FCC network consisting of electrostatically stabilized spherical particles. Their simulations are based on a statistical mechanical approach using the Monte carlo method. The particle-particle interaction used in the calculations are based on classical DLVO type pair potentials and assumed pairwise additivity. The surface potential and the Hamaker constant were kept constant at 60 mV and $1x10^{-20}$ J, respectively, for all the calculations. Their results are tabulated on Table 4.2 for various solid volume fractions, ϕ, and different electrolyte strengths, n. The electrostatic interaction potential is inversely proportion to particle separation. Thus, the colloidal network becomes more stiff as the solids content is increased. Increasing background electrolyte shortens the Debye layer thickness. In effect, the electrostatic interaction between the particles is lowered for the same particle separation. Correspondingly, lowering the electrolyte concentration makes a given volume fraction network more compliant.

Note that the value of the elastic moduli and shear moduli are typically less than 1 kPa. The magnitude of the elastic moduli are sufficiently small to suggest that the interparticle separation should collapse under the capillary stress of drying (> 1 MPa). Hence the rise time during drying should correspond to the time required to remove the liquid retained in the repulsive layer between dispersed particles. The experimental results is consistent with this reasoning. The rise time was between 120 to 180 sec for films produced from 0.35 μm particles and was 60 sec for 0.68 μm particles. This observation was consistent since the relative thickness of the repulsive layer is larger for smaller particles.

Shrinkage occurs when the repulsive layer is removed during drying. This amount of shrinkage can be estimated from the differences between the saturated and dried packing densities. For films produced from the AKP30 powder (0.35 μm), the volume shrinkage is 5 ± 2%. For ones produced from the AKP15 powder (0.68 μm), this shrinkage is 2 % which is the detection limit of our measurements. The films produced from the smaller particles shrank more. Since the films are constrained in the x-y direction by a rigid substrate, shrinkage can only occur in the thickness direction. Therefore, a 2 μm shrinkage should occur in the thickness direction for a 40 μm thick film produced from 0.4 μm particles during drying. This small amount of shrinkage was observed in a film between the saturated and the dried state under the optical microscope. An *in-situ* thickness measurement can confirm whether this shrinkage had in fact occurred during the rise time when the liquid between the particles was presumably removed.

When the shrinkage ceases, pores in the green film will begin to empty

Table 4.2 - Elastic (C_{ii}) and shear (G) moduli of a model colloid calculated by Van Megen *et al.* [4] for 0.6 μm spherical particles in a FCC network for three electrolyte concentrations.

n = 1 mM				
ϕ	C_{11} (Pa)	C_{12} (Pa)	C_{44} (Pa)	G (Pa)
70	9640	4730	4730	378
65	472	234	237	190
60	14.5	5.94	8.21	66.4
50	0.269	0.062	0.182	0.15
n = 0.1 mM				
70	2590	1290	1290	1030
65	1500	751	751	600
60	598	299	299	239
50	45.3	22.5	22.7	182
n = 0.01 mM				
70	--	--	--	--
65	296	147	147	118
60	255	127	127	102
50	147	73.1	73.1	59

during drying. With each pore being emptied, its contribution to the average stress measured by the deflection of the substrate will diminish. At a constant weight of weight loss, the stresses in the alumina films were found to decrease at a relatively constant rate. This suggest that each pore contribute equally to the stress and are approximately the same size. The alumina powders used in this study have very narrow particle size distributions. Hence the resulting pore size distribution of the green film are also narrow. The 1.1 μm α-quartz powder has a very broad particle size distribution. In this case, the stress seem to decrease at different rates during drying. Finally, at the end of the constant rate period (~20 % saturation), capillary redistribution ceased to operate and zero stress was detected (except in films where a residual stress was retained).

Examining the stress history data of the various films, it is evident that only the AKP30 and AKP15 alumina films exhibit residual stress when dried. In fact, the stress actually increases slightly toward the end of drying and the magnitude of that residual stress observed was as high as 500 kPa for films produced from 0.4 μm particles. Several explanations may account for this observation. First, background electrolyte can precipitate out as salt bridges between particles during drying [5]. This process can lead to residual shrinkage leading to the observed stress. Secondly, it has been well established that surface hydroxide species are present on alumina surface in an aqueous medium. If this layer is of sufficient thickness, shrinkage of this layer can occur during the final stage in drying can give rise to a significant amount of strain. Finally, residual strain may have occurred in all the films studied, but that only the AKP films prepared under a

certain condition can retain this strain whereas others were microcracked on a very fine scale. The residual strain may be an effect of the rigid constraint of the substrate in hindering shrinkage during the drying the films. Several characterization techniques were used and experiments were performed to evaluate these possibilities. These will be described in full detail in the next chapter. The results suggested that neither salt bridging nor surface hydroxides were formed to a large enough extent to account for the observed strain. Microcracking, however, may occur in such a fine scale that experimental observation was not possible. At this point, the microscale cracking seems to be a reasonable explanation. One possible method to confirm this is to test the mechanical integrity of the dried films; ones that are microcracked should be more fragile than ones intact.

4.4.3 Strength of the Granular Films

As discussed in the last chapter, from linear elastic fracture mechanics, the fracture resistance of a thin film on a rigid substrate is related to the critical cracking thickness and the tensile stress by Equation 3.8,

$$K_I = 1.4\sigma\sqrt{h_c} \qquad \textbf{3.8}$$

An estimate of the fracture resistance of the green films can be obtained using the stress maximums measured in the different granular films during drying and their critical cracking thicknesses. The results of these calculations are tabulated on Table 4.3. Note that for similar size particles, the granular alumina films are twice as tough as the silica ones. Films produced from smaller particle sizes also exhibit

Table 4.3. Fracture resistance values calculated from Equation 3.8 for granular films. The intrinsic flaw sizes are calculated using $a_c = (K_{IC}/\sigma)^2$.

Powder	Part. size (μm)	σ_{max} (MPa)	CCT (μm)	K_c (MPa-$m^{1/2}$)	Flaw size (μm)
AKP30	0.35	1.85	60	2.0×10^{-2}	29
AKP15	0.68	1.05	85	1.4×10^{-2}	44
Reynolds	0.35	2.15	40	1.9×10^{-2}	20
α-quartz	0.8	1.05	24	7.2×10^{-3}	12
α-quartz	1.1	0.77	44	7.2×10^{-3}	22

higher strength than those from larger particles. Whether these numbers are reasonable estimates is discussed below.

Theoretical estimates for strength of granular aggregates were investigated by Rumpf [5]. His theory is based on the van der Waal's attraction between spherical particles. For two spherical particles of diameter D, separated by a distance a, the attractive force H is given by

$$H = \frac{AD}{24a^2} \quad , \qquad 4.2$$

where H is the Hamaker constant. By summing these forces for a particle assembly of volume fraction ϕ, he obtained strength σ as

$$\sigma = \frac{1.1\phi}{(1-\phi)} \frac{A}{24a^2D} \quad . \qquad 4.3$$

Other than the arbitrary value assigned to a, the major setback of Rumpf's approach is that each particle contact make a similar contribution to the strength of the greenbody and that failure is assumed to occur simultaneously across the assembly of particles. It has been generally accepted, however, that materials fail by the propagation of cracks which may initial at some intrinsic flaw or defect.

Kendall *et al.* [6] have taken the approach of linear elastic fracture mechanics to determine the strength of granular ceramic bodies. Under Griffith's theory, fracture will occur in an elastic solid when the elastic energy that's released from extending a crack is greater than the surface energy required for the formation of new surfaces ahead of the crack tip. In another words, cracking is spontaneous only if the potential energy of the system is continually lowered. The energy associated with the new surface should be equivalent to the interfacial energy. But in reality, the fracture energy is greater than the surface energy due to other energy releasing effects such as microplastic deformation at the crack tip and heat dissipation. Assuming that an assembly of spherical particles held together by surface tension force acts as a continuum, Kendall derived expressions for the effective Young's modulus E^* and effective fracture energy G^* for the assembly,

$$E^* = 17\phi^4 \left(\frac{E^2\Gamma}{D}\right)^{1/3} \qquad 4.4$$

$$G^* = 56\phi^4 \left(\frac{\Gamma_c^5}{E^2D^2}\right)^{1/3} \qquad 4.5$$

where ϕ is the volume fraction of solids, Γ_c is the fracture surface energy, D is the particle diameter, E and Γ are the Young's modulus and surface tension of the solid, respectively. Experimentally, Kendall calculated Γ_c values for TiO_2 and Al_2O_3 from fracturing notched beams made from green powder compacts of the respective materials. The values he obtained were over an order of magnitude

Table 4.4. Equilibrium surface energy and measured fracture surface energy for alumina and titania from Kendall [5].

Material	Γ_c (J-m^{-2})	Γ (J-m^{-2})	Part. size (μm)
Al_2O_3	21	0.58	0.4
TiO_2	14	0.60	0.23

larger than the equilibrium surface tension values (Table 4.4).

By definition, $K_{IC} = (EG)^{1/2}$, therefore, the effective fracture toughness of the particle assembly is

$$K_{IC}^{*} = 31\phi^{4}\Gamma_c^{5/6}\Gamma^{1/6}D^{-1/2} \qquad 4.6$$

The K_{IC} value for alumina calculated from Kendall's equation using the fracture

energy value he obtained is 8.4 x 10^{-2} MPa-$m^{1/2}$ which is approximately four times higher than that obtained from our measurements. This difference in strength may be due to differences in sample preparation. The slips Kendall used to form his bend bars contained 33 wt% polyvinyl alcohol as a binder. The green bars were subsequently fired to 500°C to burn out the binder prior to mechanical testing. A small amount of carbon residue, however, can contribute to strengthen the green bar. Since organic additives were not used in preparing the films studied here, the fracture toughness values should be more representative of a binder-free assembly of granular particles.

Both approaches described above rely on the surface force between particles as the source of strength of the particle assembly. In fact, the Hamaker constant and interfacial energy are related [7]. We should see a consistent trend in the fracture resistance of the particle assembly to the magnitudes of the interfacial force binding the assembly for the different materials studied. From our measurements, we see that the fracture resistance of quartz is half of that of alumina. Correspondingly, we find that the Hamaker constant for quartz is approximately half of that of alumina in air, 8.8 x 10^{-20} J and 15.6 x 10^{-20} J, respectively. In general, we also observed a particle size effect in the fracture resistance values; the green films made from small particles were stronger.

From the fracture resistance and the measured stress values, we can estimate the size of the largest intrinsic defect in the green film. For an edge crack in a semi-infinite medium under an externally applied uniaxial stress σ, the critical flaw size is $a_c = 0.25\ (K_{IC}/\sigma)^2$. The critical defect sizes for the green films

studied were calculated are also tabulated on Table 4.3. Note that in all cases the defect sizes are almost two orders of magnitude larger than the particle size.

To account for the high fracture toughness values and the low strengths observed in his experiments, Kendall claims that agglomerates on the order of tens to hundreds of micrometers are the source of the natural defect in the green bodies he studied. By successively removing the agglomerates through milling, he found that the average strength of the greenbodies increased, suggesting that the increase in strength is due to the decrease in defect size. In this study, however, the granular particles were undoubtedly monodispersed in the process, free of any agglomerates with sizes as large as the defect size shown in Kendall's powder compacts. Furthermore, agglomerates were not observed in the dried films when examined under the optical and the scanning electron microscope. This raises questions on whether a simple continuum mechanics model is sufficient to describe the mechanical behavior of packed granular solids. Clearly, a mechanics model more representative of the physical picture of packed granular solids is needed. Nevertheless, the continuum approach does provide a relative measure of the strength of granular ceramic greenbodies.

4.5 Conclusions

The stresses that develop during the drying of granular ceramic films produced from alumina and silica powders were measured by a substrate deflection method using an optical interference technique. The moisture saturations in the

films were simultaneously monitored by weight loss measurements. A region of uniform saturation can be established in a drying film due to the wicking action of the fine capillaries in the green film during drying. According to equation 3.1, uniformly saturated film will be established during drying when the film dimensions are less than 1 x 1 cm. By monitoring the weight changes and the substrate curvature simultaneously during drying, the stresses developed at different saturations were measured. In all cases, stress does not develop in the drying film until the supersaturated region becomes extinct. The stress reaches a maximum just beyond this point and decreases monotonically thereafter. The measured stress maximum was near 2 MPa for films produced from 0.35 μm particles. The measured stress maximum was found to be inversely proportional to the particle size of the green film, and proportional to the liquid surface tension. These measurements represent the first evidence that the drying stress in a granular body is due to the capillary tension in the pore liquid.

The magnitude of the drying stress also provided some insight into the drying shrinkage behavior. At the moment when the supersaturated region becomes extinct, the particles in the film are still separated by an electrostatic repulsive layer. Upon further drying, the stresses developed around the fine capillaries act to draw the particles together. Van Megen *et al.* provided theoretical estimates of the compliances of a model colloid system. The drying stress is two orders of magnitude higher than the disjoining pressure between the particles. Therefore, shrinkages should occur prior to the time at which the pores have emptied. *In-situ* drying shrinkage measurements will be necessary to confirm

this hypothesis.

The green strengths of dried green films were also assessed in this study. From the measured stress maximum and the critical cracking thickness, the fracture resistances of the green films were calculated from a relationship derived from LEFM (Equation 3.8). The relative strengths of the green films were found to be proportional to the Hamaker constant of the film material. This is consistent with the assumption made by many researchers that van der Waals or surface forces are responsible for the strength of binder-free granular greenbodies. The intrinsic defect size calculated from the continuum fracture mechanics approach resulted in values on the order of 10 - 30 μm. Such large size defects, however, were not observed in the films produced in this study. This shortcoming maybe a result of applying continuum mechanics to a porous body.

References

1. J.D. Finegan and R.W. Hoffman, "Stress and Stress Anisotropy in Iron Films"; pp.935-42 in the Eighth National Symposium on Vacuum Technology Transactions. Pergamon Press, New York, NY, 1961.

2. R.W. Hoffman, "Mechanical Properties of Thin Condensed Films"; pp.211-73 in Physics of Thin Films. Edited by G. Hass and R.E. Thun. Academic Press, New York, NY, 1966.

3. W.A. Brantley, "Calculated Elastic Constants for Stress Problems Associated with Semiconductor Devices," *J. Appl. Phys.* **44** [1] 534-35 (1973).

4. W.J. Van Megen and I.K. Snook, "Elastic Properties of Model Colloids," *J. Colloid Interface Sci.* **77** [1] 131-37 (1980).

5. K. Kendall, "Agglomerate strength," *Powder Metallurgy* **31** [1] 28-31 (1988).

6. H. Rumpf, "Grundlagen und Methoden des Granulierens," *Chemie-Ing.-Techn.* **30** [3] 144-58 (1958).

7. P.C. Hiemenz, **Principles of colloid and surface chemistry, 2nd ed.**, pp.650-51, Marcel Dekker, Inc., New York, NY, 1986.

CHAPTER 5

RESIDUAL STRESS IN DRIED GRANULAR FILMS

5.1 Introduction

Residual stress was found in some of the dried granular films produced in this study. In fact, the stress in the film actually increased toward the end of drying. Since capillary stress had already ceased to operate at this point, this residual stress may be due to other shrinkage mechanisms. The occurrence of this residual stress, however, was not observed in films produced from all the slips made. Of the two alumina powders used, Sumitomo and Reynolds, only the Sumitomo powders produced films having residual stresses between 0.2 - 0.4 MPa. This suggests that there may be some subtle differences between the two alumina powders, although their phase and chemical purity were found to be nearly identical as reported by the manufacturers. Therefore, the purpose of this chapter is to address the origin of this stress and its implication on the drying of granular films.

There are several possibilities for the source of residual strain in the dried films. Foreign material may be present on the granular particle surface or in the supernatant solution. Examples include surface hydroxide species on the particle surface or dissolve electrolyte species in the supernatant solution. Alumina is

known to develop a surface hydroxide layer when exposed to water [1]. Since this layer may be gel-like, additional shrinkage can occur in the particle assembly when this layer dries. Similarly, shrinkage can also occur when small amounts of dissolved electrolyte precipitate out of the solution between aggregates of particles and slightly rearrange the particle network toward the end of drying.

Furthermore, the residual strain may be an effect of the rigid constraint on the shrinkage behavior of the film during drying. In this case, all the films studied should retain a residual stress. But the green strength of the films may differ. The films which exhibited residual stress may be have higher green strength than the ones which did not. The presence of surface hydroxides and/or salt bridging may provide strengthening in the green films.

To evaluate these possibilities, several surface characterization techniques were used to study the dried films. Fourier transform infrared spectroscopy (FTIR), transmission electron microscopy (TEM), and electron spectroscopy for chemical analysis (ESCA) were used to investigate whether electrolyte and surface hydroxide species were present. Electrokinetic measurements were also performed to characterize the powder surface and colloid stability. Thermogravemetric analysis (TGA) of the films and elemental analysis of slip supernatants by Inductive Coupled Plasma spectroscopy (ICP) were also performed. Finally, different slip formulations were prepared in an attempt to isolate the source of the residual stress.

5.2 Experimental Procedure

Several alumina slip formulations were used for this study. Eight of them were made from Sumitomo AKP30 alumina. The general procedure for stabilizing the dispersions were same as described in earlier chapters. Typically, 0.5 ml of 15.7 M HNO_3 acid were required to prepare 100 ml of slip containing 20 vol% alumina. Slip AKP2 was the control sample and was prepared with the normal procedure. In the case of slip AKP1, twice the normal amount of nitric acid was added. Slip AKP1' was the same slip used in the study presented in Chapter 4. Slip AKP1" was prepared with the same recipe as AKP1 to check for reproducibility. To provide a fair comparison between the Sumitomo and the Reynolds powders, sample AKP3 was centrifugally classified the exact same way as the Reynolds dispersions. AKP4 and AKP5 were slips prepared from AKP2 with $Al(NO_3)_3$ solution added to yield 2 mM and 10 mM background concentration of Al^{3+} ion, respectively.

Four different Reynolds alumina dispersions were prepared. R1 is the as classified dispersion and R2 is prepared from R1 with excess nitric acid added (0.5 ml 15.7 M HNO_3 to 100 ml of slip). R3 and R4 were prepared from R1 with $Al(NO_3)_3$ solution added to yield 2 mM and 10 mM background concentration of Al^{3+} ion, respectively. A summary of sample description is given in Table 5.1.

Fourier transform infrared spectroscopy of the samples was performed in transmission mode. This sampling technique is possible since the particle size of the powder used in this study is less than 1 μm and scattering of the infra-red radiation is not significant. Films having nominal thickness of approximately 60 μm were cast onto 2 mm thick 13 mm diameter silver chloride substrates. The

films were allowed to fully dry under ambient conditions prior to analysis.

Powders were examined using an ultrahigh resolution TEM (EM-002B TEM, Akashi Beam Technology Corp., Japan). Samples were prepared by dipping a TEM sample grid in a very dilute dispersion of alumina. Micrographs were taken in the bright field mode.

ESCA was also used for surface analysis of the alumina powders. This analysis involved the irradiation of the powder in high vacuum (10^{-8} - 10^{-9} torr) with monoenergetic soft X-ray (Mg Kα, 1253.6 eV) and the measurement of the energy of the electrons emitted from a surface layer of about 20 - 30 Å in depth. The ESCA samples were prepared by lightly dusting dried alumina powder onto a piece of double sticky tape which was mounted to a sample holder. The detection limit of this instrument is 1 - 2 atomic percent.

Thermal gravemetric analysis (TGA) were performed under 10 sccm flow of air with a heating rate of 10 °C/min to 950 °C. TGA samples were obtained by mechanically removing dried films that were cast onto glass substrates.

Zeta-potentials of the alumina dispersions were measured with an electrokinectic sonic amplitude (ESA) measurement apparatus (ESA 8000, Matec Applied Sciences, Inc., Hopkinton, MA). This device applies an alternating electric field to the dispersion, which creates relative movement between the ceramic particles and the surrounding liquid. In turn, this motion generates a sound wave at the same frequency as the applied electric field. The acoustic energy that's measured is proportional to the electrophoretic mobility. Therefore, zeta-potential values can be correlated to ESA measurements [2].

The standard procedure for ESA measurement involved preparing approximately 200 ml of a suspension containing 1- 10 vol% solids in deionized water. Since the slips used for producing films were typically 20 vol% solids, they were diluted to 3 vol% by adding DI water for ESA measurements. Potentiometric titrations of the suspensions were performed at three background electrolyte concentrations: 1 mM, 10 mM, and 100 mM KNO_3. From the zeta-potential versus pH curves at different ionic strengths, the point of zero charge (PZC) is determined by the common point of intersection of these curves. Finally, residual stress measurements were made using the same equipment and procedure as described in the last chapter.

5.3 Results

Stress measurements showed that only AKP1 and AKP1' can be used to produce films having residual stress. Although AKP1" was prepared with the same recipe as AKP1, no residual stress was found in the films produced from this slip even after aging for two weeks. The AKP1 slips and the slips having 10 mM Al^{3+} produced films having very rough surfaces. Examination of these dried films under the optical microscope revealed agglomerates, indicating that some flocculation had occurred during drying. All the pertinent results are summarized in Table 5.2.

Quantitative analyses of the impurities in the alumina powders were carried out using inductive coupled plasma (ICP) emission spectroscopy, and reported by

Table 5.2. Summary of results.

Sample	Age (days)	pH	$[Al^{3+}]$ (mM)	PZC	ζ (mV)	σ_{res} (MPa)
AKP1'	1 6 7 92	3.4	--	--	--	0.4 0.2 0.4 0.4
AKP1"	1 7 14	3.4	--	--	--	0 0 0
AKP1	1 3	3.4	7.0	--	32	0.2 0.45
AKP2	6 8 22	3.5	0.7	8.8	35	0 0 0
AKP3	1 7	3.3	--	8.8	42	0 0
AKP4	1 2	--	2.7	--	--	0 0
AKP5	1 2	--	10.7	--	--	0 0
R1	>3 yrs	3.3	1.6	8.8	42	0,0,0
R2	1 2 7	--	5.0	--	--	0 0 0
R3	1 2	--	3.6	--	--	0 0
R4	1 2	--	11.6	--	--	0 0

Table 5.3. Inductive coupled plasma emission spectrometric analysis results of Al and Si in suspension supernatants.

Sample	Al (mM)	Si
AKP1	7.0	0
AKP2	0.7	0
R1	1.6	0
R2	5.0	0

Rhine *et al.* [3]; both powders are of relative high purity. The major impurities in the Sumitomo powder were Si (23 ppm) and Zr (38 ppm); those in the Reynolds powder were Fe (84 ppm), Ga (92 ppm), Na (26 ppm), and Si (220 ppm). ICP analyses for Al and Si were also carried out on the supernatant from slip samples. Predominantly Al was found in the solutions and the results are listed on Table 5.3. Large amount of acid addition produced slips having higher concentrations of Al ionic species.

TGAs of the Sumitomo and Reynolds powders are shown in Figures 5.1 and 5.2, respectively. For the as received powder, the weight loss up to 100°C corresponds to the removal of bulk surface water. Surface hydroxyl groups were subsequently removed when heated to high temperatures [4]. TGAs showed that a

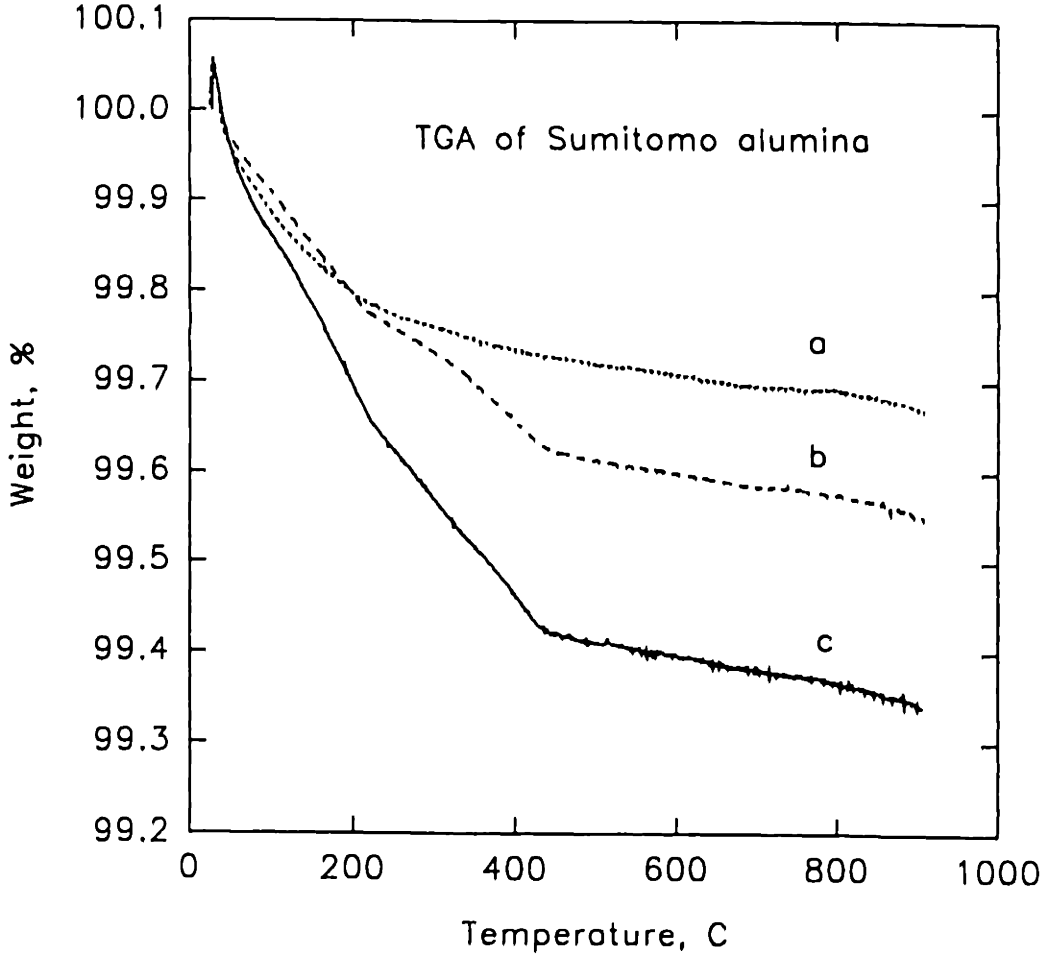

Figure 5.1. Thermogravemetric analysis of Sumitomo AKP30 powders: a) as-received, b) dried from slip AKP2, c) dried from slip AKP1 (excess acid). Experiments were performed in 10 sccm of air at 10°C/min.

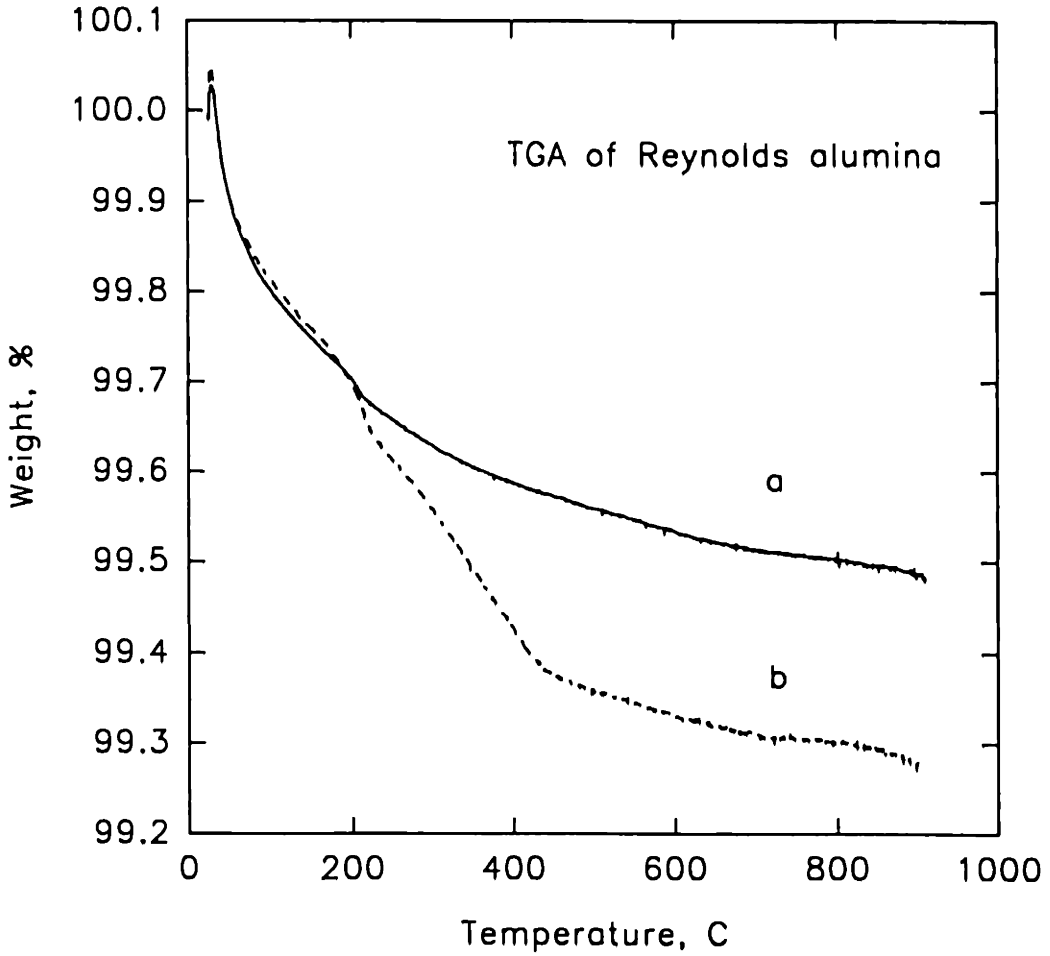

Figure 5.2. **Thermogravemetric analysis of Reynolds powders: a) as-received, b) dried from classified slip.**

separate decomposition reaction was occurring between 150 to 400°C in the dried powder from stable suspensions. The increase in weight loss in this temperature range can be attributed to the decomposition of $Al(NO_3)_3$ and an increased amount of surface hydroxyls. The TGA of $Al(NO_3)_3 \cdot 9H_2O$ is shown in Figure 5.3. With increasing acid addition, an increase in weight loss was observed. The supernatant from sample AKP1 was 7 times higher in Al concentration than that from AKP2 from ICP analysis results. If all the Al precipitated out as $Al(NO_3)_3 \cdot 9H_2O$, the TG weight loss of the dried film would have increased by 0.22 %. Correspondingly, the TGA data in Figure 5.2 showed an increase of 0.22 %.

Shown in Figures 5.4 and 5.5 are the IR spectra of films produced from slips AKP1 and AKP2. Note that although AKP1 had twice the amount of nitric acid added to it, its IR spectra is identical to that of AKP2. Shown in Figure 5.6 is the IR spectra of R1, note that the spectra also appear identical to the Sumitomo alumina slip shown earlier. In fact, IR spectra of all 11 samples appear the same. The peaks between 3300 cm^{-1} and 3600 cm^{-1} can be assigned to hydrogen bonding characteristics of surface hydroxyls on α-alumina surface [1]. The absorption band at 1350 cm^{-1} can be assigned to the presence of ionic nitrate.

Figures 5.7 and 5.8 are TEM micrographs of the powder particles from the AKP1 slip. Note that the lattice images were observed to the edge of the particles, indicating the absence of any amorphous species. Figures 5.9 and 5.10 are TEM micrographs of Reynolds powder taken from R1. Note that the particle shape is more equiaxed than that of the Sumitomo powder. Again, the particles appeared to have clean surfaces.

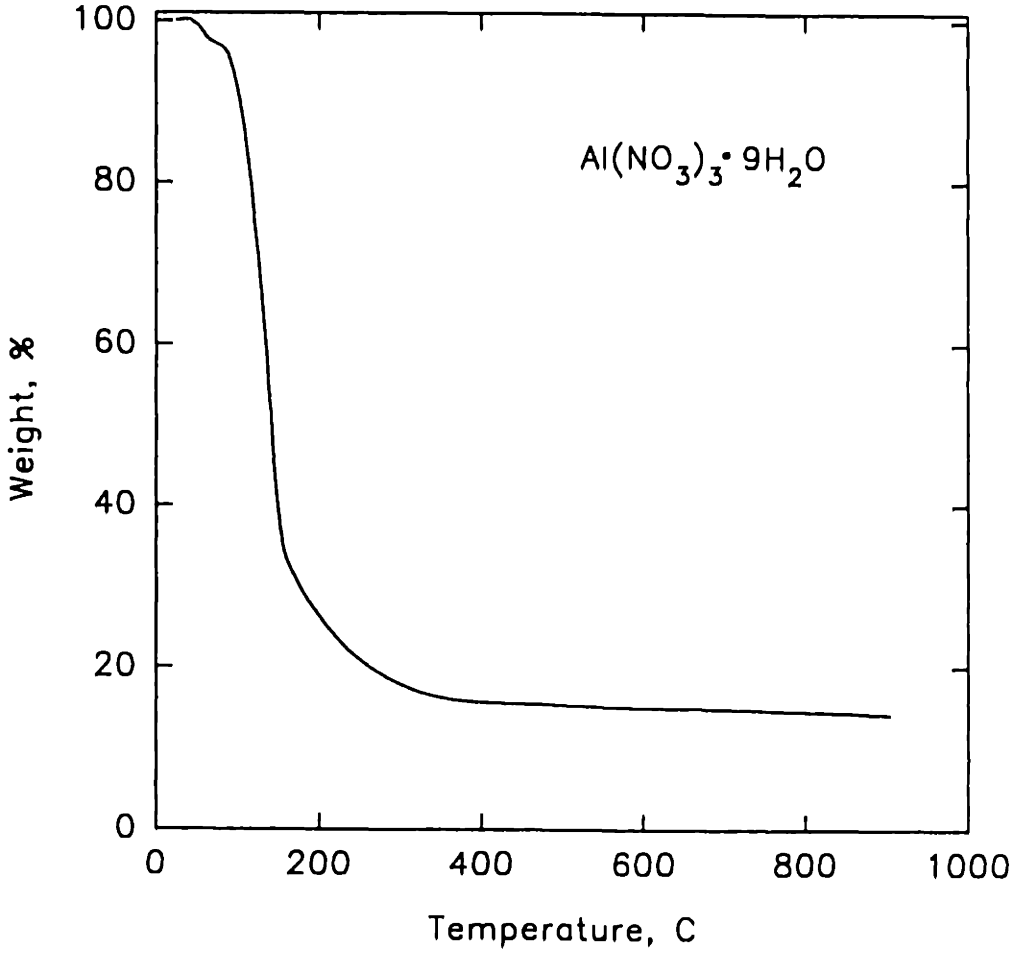

Figure 5.3. Thermogravemetric analysis of $Al(NO_3)_3 \cdot 9H_2O$.

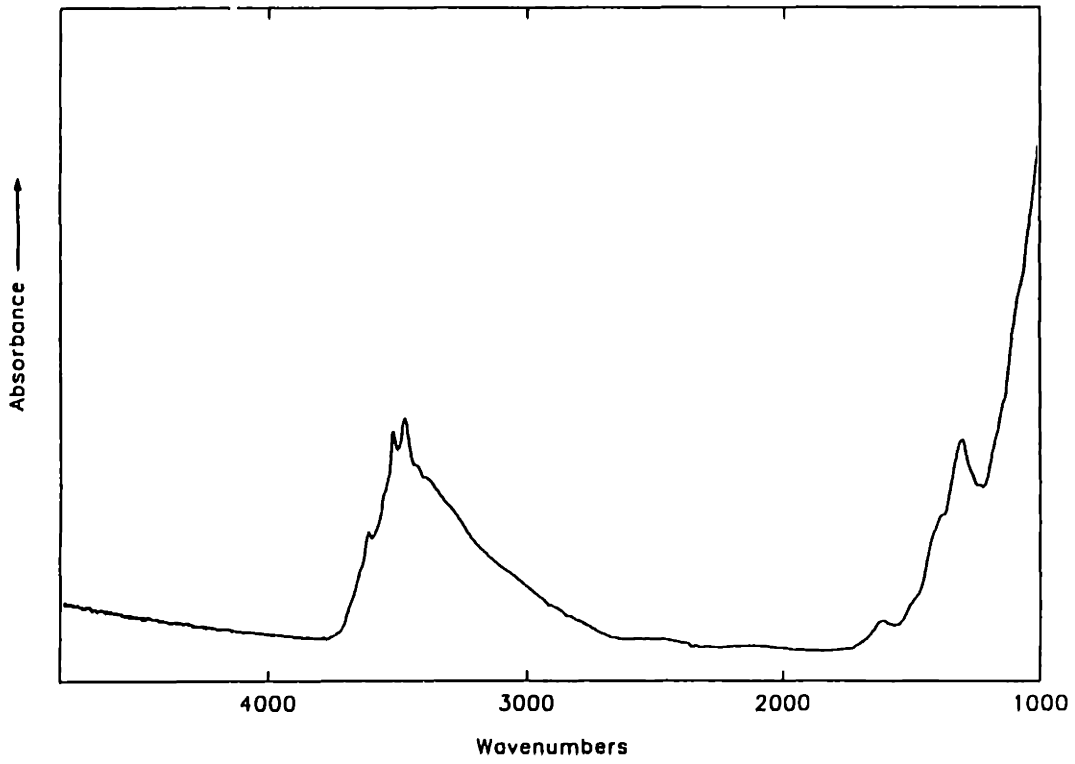

Figure 5.4. IR spectra of film produced from AKP1.

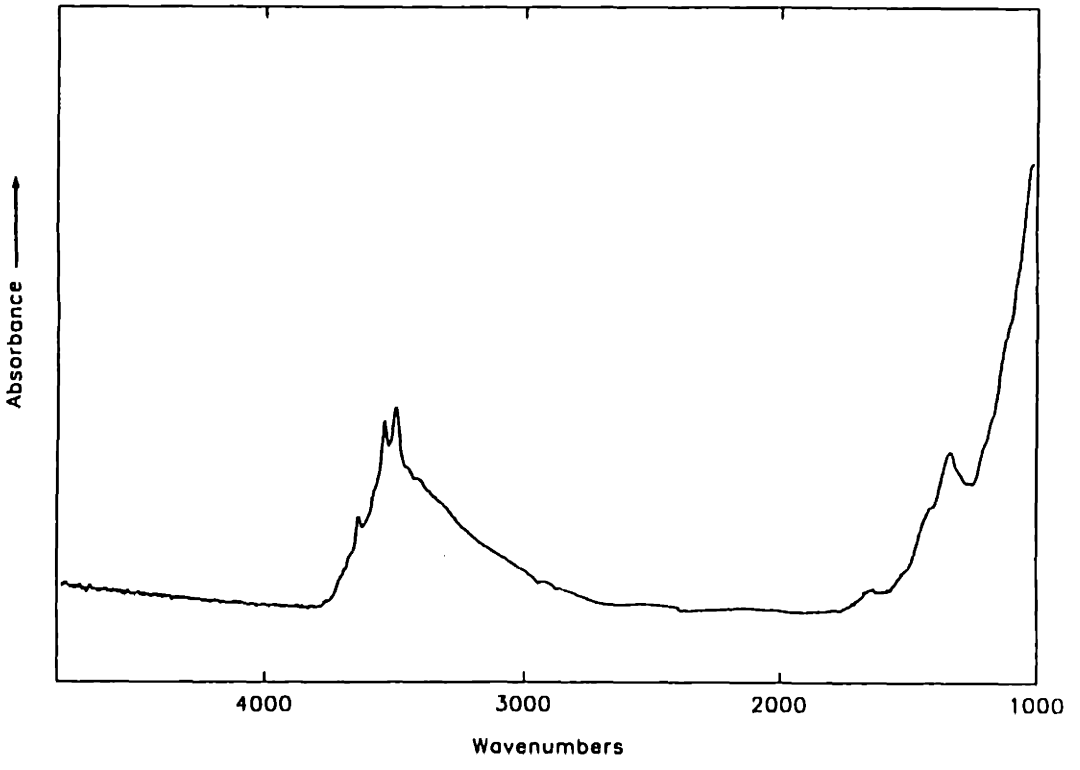

Figure 5.5. IR spectra of film produced from AKP2.

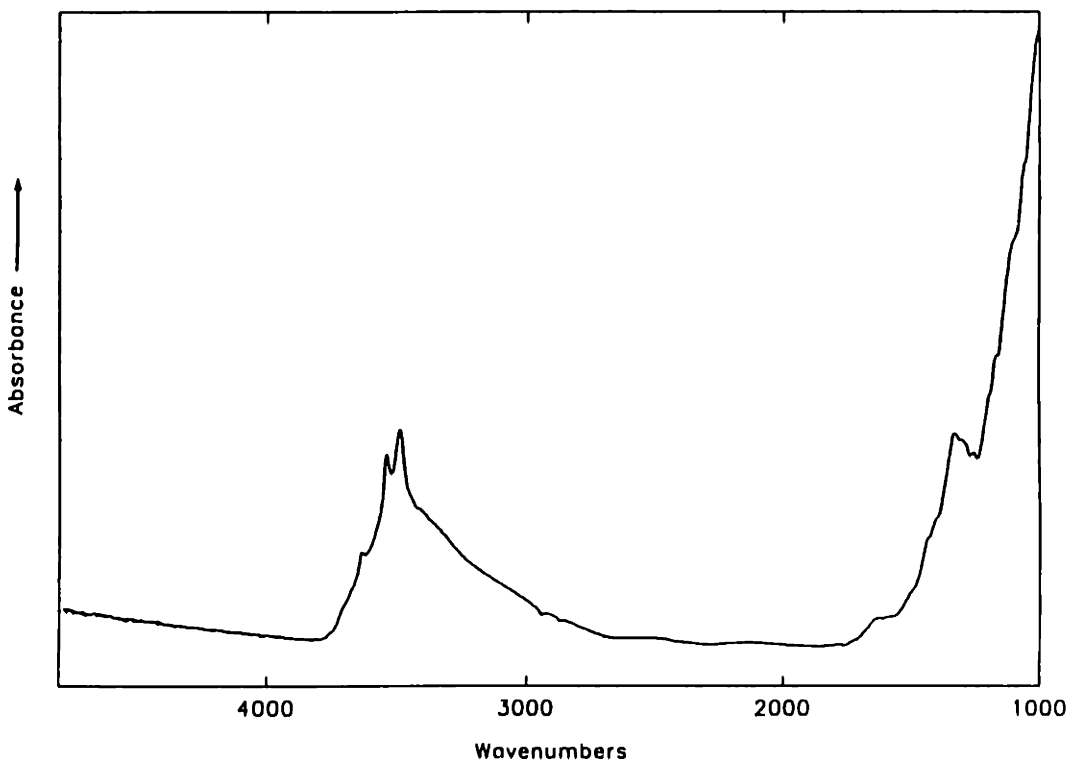

Figure 5.6. IR spectra of film produced from R1.

Figure 5.7. TEM micrograph of alumina particles from AKP1.

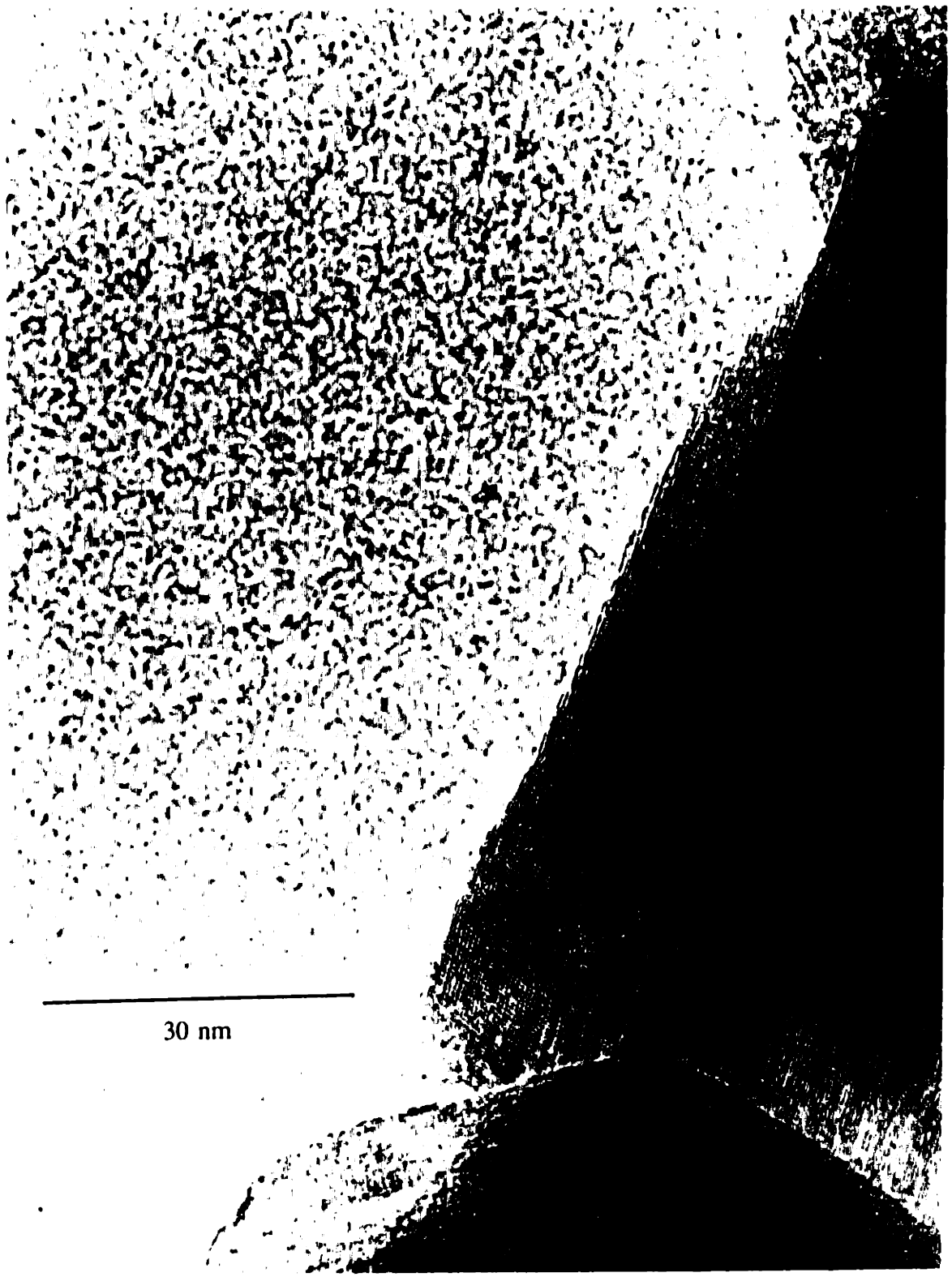

Figure. 5.8. **TEM micrograph of alumina particles from AKP1. Note that crystal lattice images extend to the particle surface.**

Figure 5.9. TEM micrograph of alumina particles from R1.

Figure 5.10. TEM micrograph of alumina particles from R1. Note that crystal lattice images extend to the particle surface.

Four samples were analyzed by ESCA: the two as received powders, AKP1, and AKP2. In all four cases, the ESCA results were identical (see Figure 5.11). The peaks identified in this spectrum are the oxygen auger, oxygen 1s, carbon 1s, aluminum 2s, aluminum 2p, and oxygen 2s. A carbon 1s peak is typically associated with adventitious hydrocarbon, always present on samples exposed to a laboratory environment [5], and is not associated with the double sticky tape used to mount the powder sample.

Figure 5.12 shows the zeta potential data of an aqueous suspension containing the as received Sumitomo powder. The point of zero charge is approximately 8.2 which is determined by the common point of intersection of the potentiometric titration curves at three different background electrolyte concentrations. Figure 5.13 and Figure 5.14 show the zeta potential data for aqueous suspension diluted from slips AKP1 and R1, respectively. Note that the points of zero charge were raised to approximately 8.8. The magnitude of the zeta potential of the Reynolds slip (42 mV) was typically higher than that of the Sumitomo slip (35 mV) at low background electrolyte at pH below 4.

5.4 Discussion

When exposed to water, α-alumina surface can slowly attain a surface hydroxide layer [1]. In fact, the IR absorption bands of hydrated alumina powder closely resembled that of α-alumina trihydrate. When heated to 150°C for 72 hr, hydroxyl coverage in excess 160 % of monolayer coverage was found [6]. In the

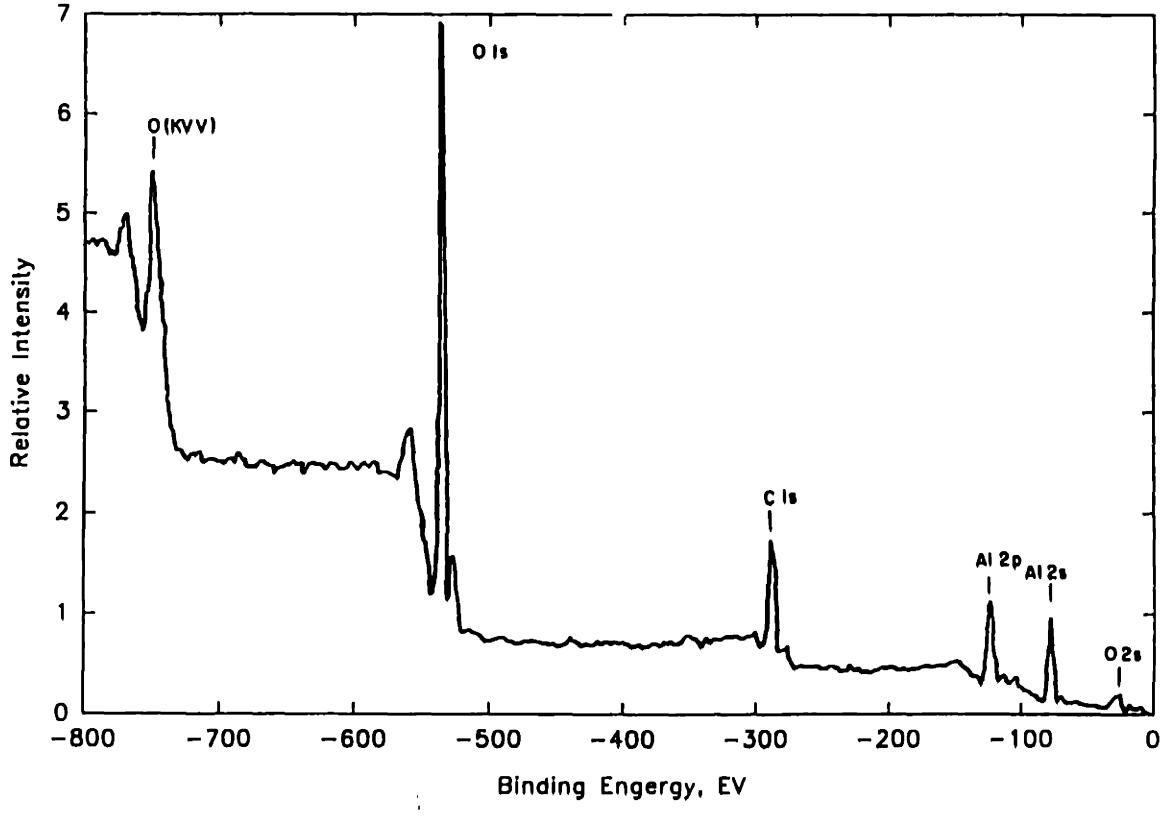

Figure 5.11. ESCA of dried powders from AKP1.

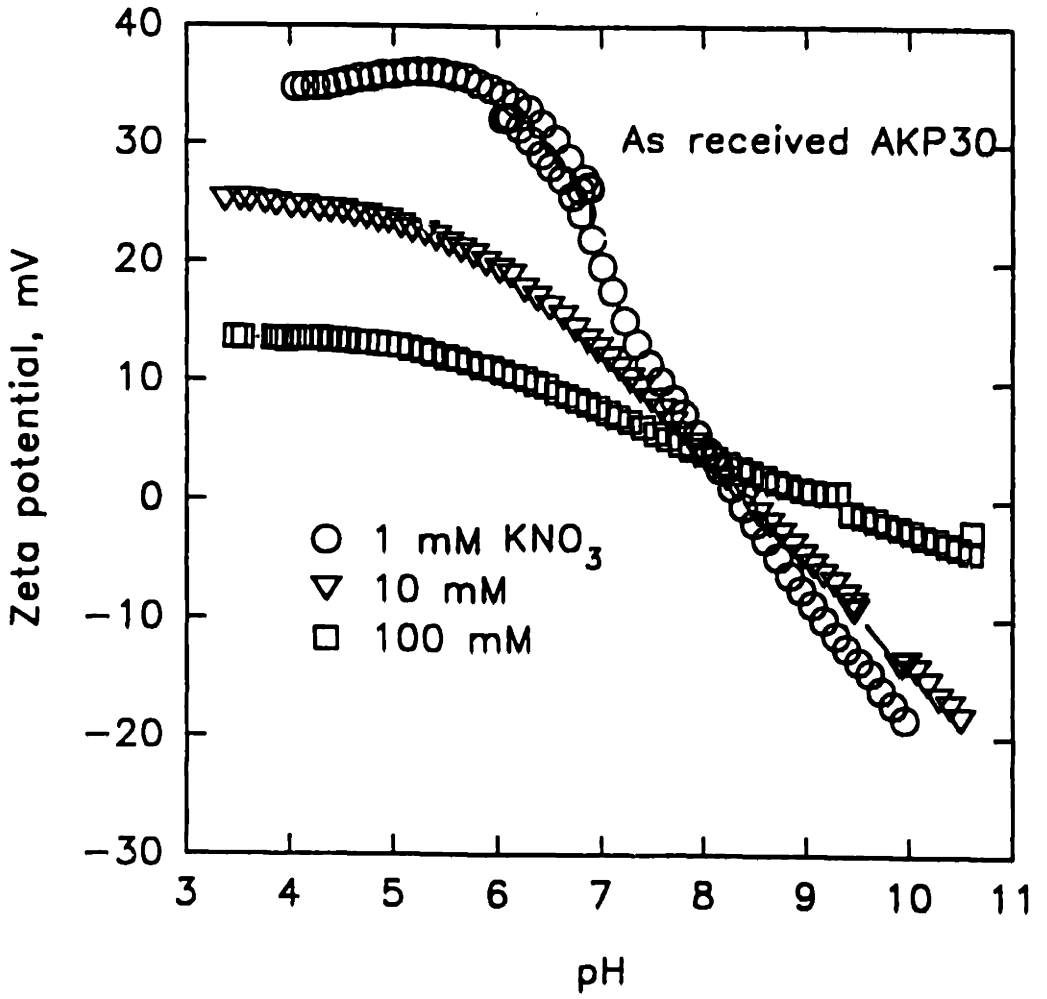

Figure 5.12. Zeta potential measurements of as-received Sumitomo AKP30 alumina during potentiometric titration at three different background KNO_3 concentrations: 1 mM, 10 mM, and 100 mM.

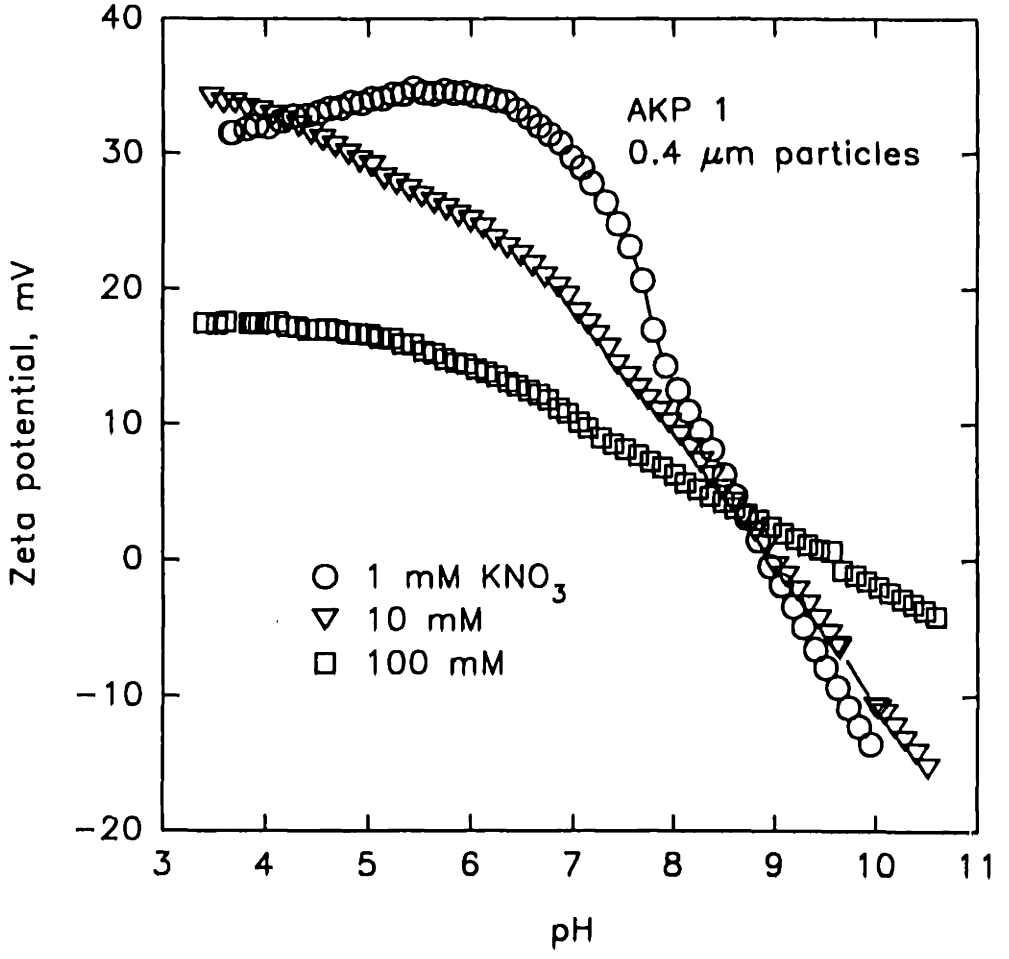

Figure 5.13. Zeta potential measurements of AKP1 during potentiometric titration at three different background electrolyte concentrations.

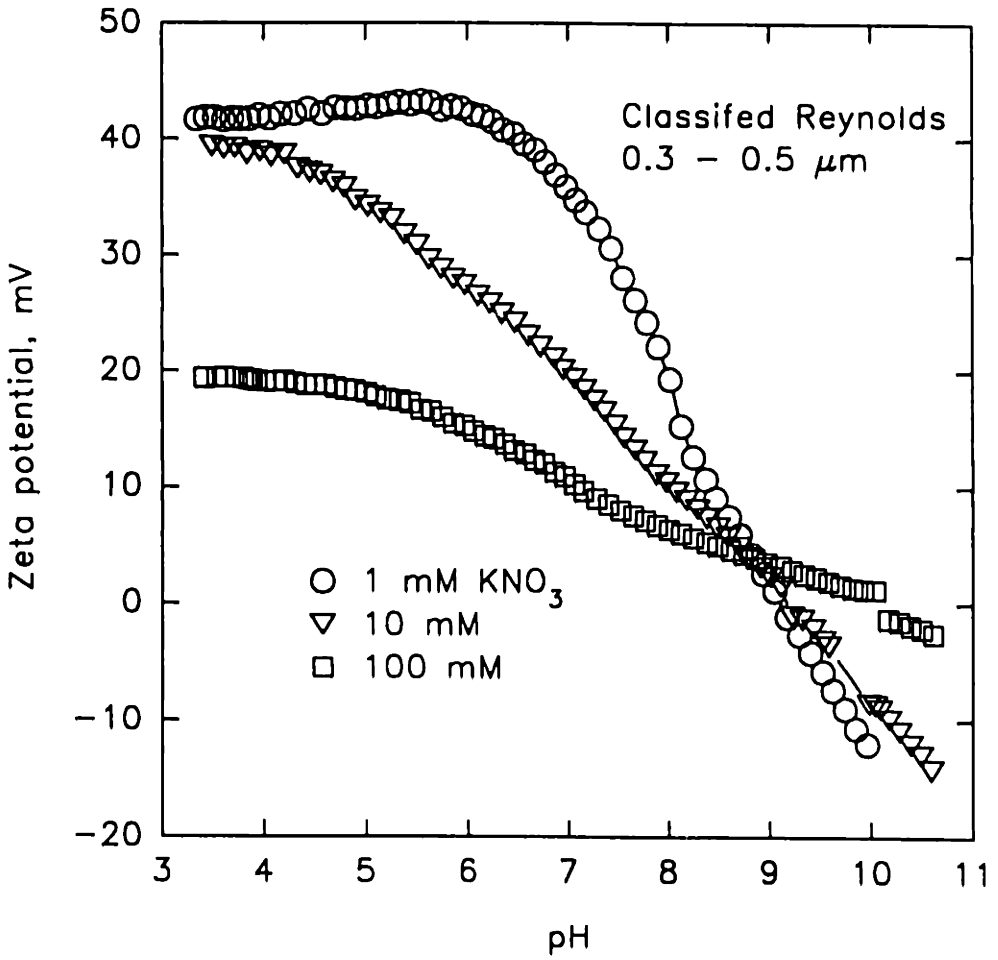

Figure 5.14. Zeta potential measurements of classified Reynold powder (R1) during potentiometric titrations at three different background electrolyte concentrations.

current study, the IR absorption band identified in the high frequency regime in the spectra of both aluminas occur at frequencies correspond to the vibrations of hydrogen bonded hydroxyls and molecularly bound water [7]. Contribution from isolated hydroxyl groups which typically occur between 3700 to 3800 cm^{-1} were also absent. Therefore, the IR results indicate the presence of a surface hydroxide layer.

The formation of this hydroxide layer at room temperature, however, is kinetically limited. This result is reflected in the wide scatter of point of zero charge measurements of α-alumina in water among the literature [8]. In general, the PZC of aged α-alumina is reported between 8.8 - 9.2 whereas freshly calcined α-alumina were found to have PZC as low as 6. The increase in the PZC is contributed to the higher surface charge density associated with the higher coverage of surface hydroxyl groups. Consistent with literature findings, the as received alumina powder had a higher PZC after aging for about a week, after which an equilibrium layer of hydroxide had formed.

Since the surface hydroxide layer developed on the alumina powder closely resembled that of gibbsite [1], its solubility in water should be similar to that of gibbsite. In Figure 5.15, the solubility of gibbsite as a function of pH is shown [9]. At pH below 4.5, gibbsite is slightly soluble to yield predominantly Al^{3+} ions (see Figure 5.16) [9]. Therefore, the alumina dispersion should contain approximately 10 mM of Al^{3+} in solution at pH of 3.5. Both the TGA of the dried powders and the ICP analysis of the corresponding supernatants confirmed this amount of Al^{3+} in the slips.

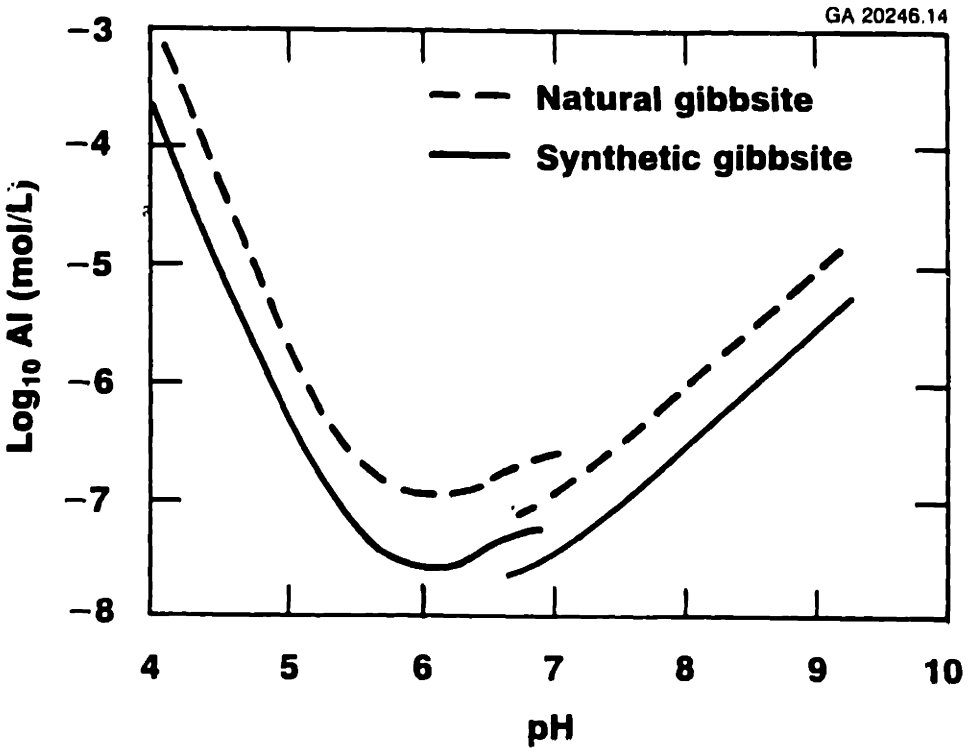

Figure 5.15. Solubility of gibbsite, $Al(OH)_3$, in water [9].

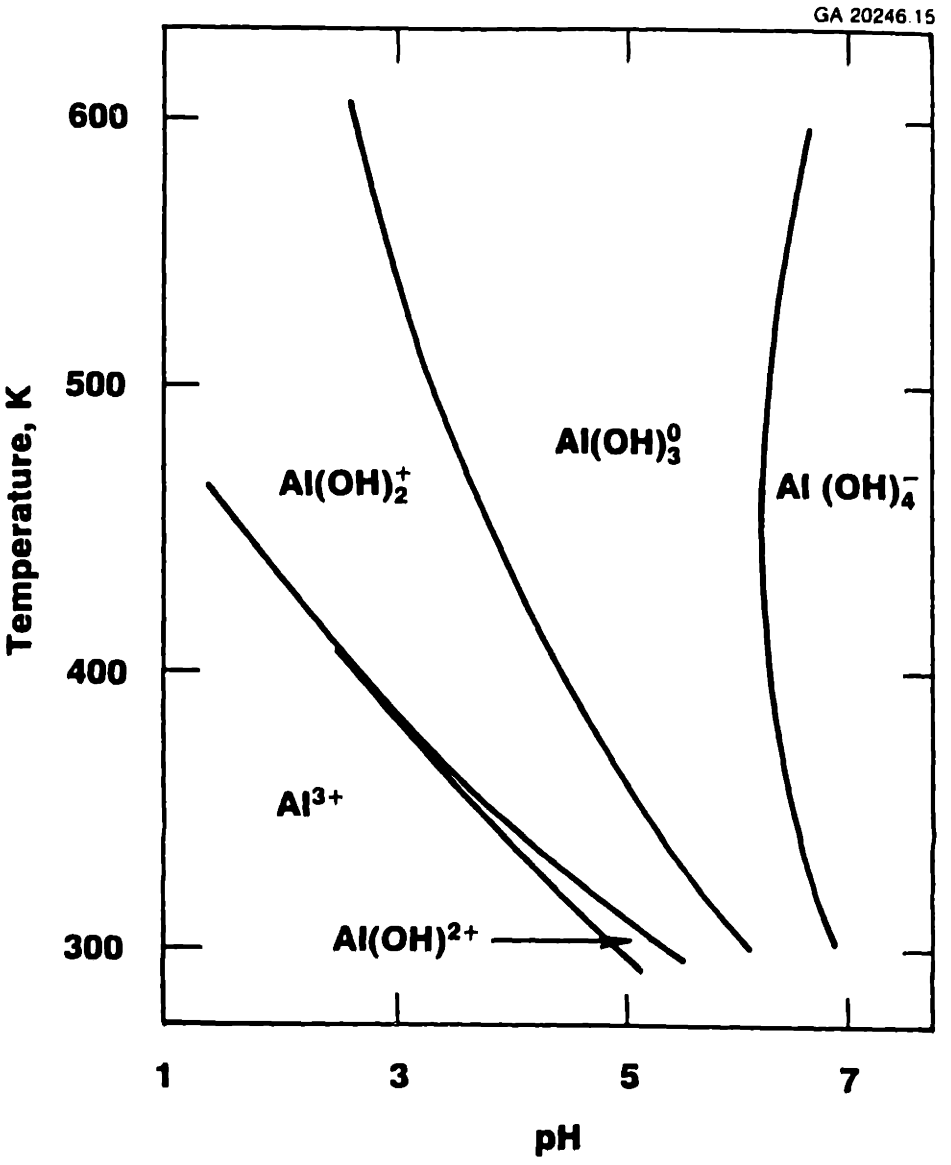

Figure 5.16. Stability ranges of aluminum hydroxyl complexes in water [9].

Although both surface hydroxide and dissolve electrolyte were detected on the powder surface and in the supernatant solution, respectively. TEM micrographs showed that the contacts between particles still appeared quite clean. Neither amorphous hydroxide layer nor salt bridges were evident from the TEM micrographs in either the AKP30 or the Reynolds powder. ESCA of the powder surfaces also confirm that foreign surface contaminants were not present in the two powders. Therefore, if the observed residual stress were a result of shrinkage relating to either the hydroxide layer or salt precipitates at particle contacts, that amount would be very small and all the films should exhibit residual stress behavior. The residual shrinkage model, however, is consistent with the fact that the measured drying stresses actually rises toward the end of drying.

The observed residual stress may also be an effect of the rigid constraint on the shrinkage behavior of the green films during drying. It has been established in the last chapter that shrinkage occurs in a drying film due to capillary forces. The presence of a rigid substrate, however, act to hinder shrinkage in the plane of the film, allowing shrinkage to occur only in the thickness direction. Therefore, stress can develop in a film due to the constrained shrinkage. Shear relaxation mechanism such as relative particle movements can relieve this stress. In this case, the relaxation time associated with this strain should be small since both the shear modulus (see Table 4.2) of a model colloidal network and the strain are quite small. But the relaxation time will be increased drastically as the network becomes more rigid when the particles are brought closer together. If all the strain is not relieved when the particles touch, a residual stress should remain in the

dried film. Although this model provide an explanation for the residual stress, it does not explain why the stress actually rises toward the end of drying. Again, all the films produced in this study should have residual stress according to this argument.

At this point, only AKP1' and AKP1 can produce films having residual stress. The concentration of Al^{3+} ion in these slip supernatants were increased by excess acid addition. But films produced from slips having aluminum nitrate solution intentionally added did not exhibit residual stress. The fact that AKP1" which is prepared with the same recipe as AKP1 did not produce films exhibiting residual stress is puzzling. Admittedly, we are able to draw any conclusion on the origin of the observed stress in the dried films based on the current experimental results. It is interesting, however, that only the AKP30 and AKP15 (see chapter 4) powders can produce films having residual stress. A possible explanation may be that most of the dried films produced in this study failed on a microscopic scale under the residual stress. The observation of residual stress in the AKP derived films, therefore, indicates higher green strength in these films. This also suggests that there may be some subtle differences between the AKP and Reynolds powder that our characterization techniques failed to identify.

From the magnitude of the residual stress, we can calculate the strain in the dried films provided that we know the Young's modulus of the dried film. Estimates, theoretical [10] or experimental [10,11,12], suggests that the Young's modulus for green granular bodies consisting of submicrometer size particles without binder addition should be between 1 - 10 GPa. Therefore, a strain on the

order of 1 x 10^{-4} will be produced for a residual stress on the order approximately 500 KPa. This is equivalent to having a 4Å shrinkage between 0.4 μm particles, which is approximately the thickness of 1 - 2 monolayer of surface hydroxyls. Apparently, the strain energy associated with this small amount of residual strain was not high enough to cause the films to spontaneously crack. However, this does not rule out the possibility of microcracking. Furthermore, the crack size and opening of these microcracks may be too fine to be experimentally observed under either the optical or the scanning electron microscope.

Obviously, more experiments are needed before we can make any conclusion on the validity of this proposal. Nevertheless, it is not theoretically unreasonable that residual strains exist in the dried green films. Since microcracked green films should be more fragile than ones intact, a possible way to experimentally confirm this theory would be to test the mechanical integrity of dried green films. At the same time, the results may lead to new understandings on strengthening mechanisms in granular bodies.

5.5 Conclusions

The origin of the residual stress observed in the dried alumina films was proposed and investigated. Several samples of alumina slips were prepared from the AKP30 and Reynolds powder. It was found that only the AKP30 powder prepared with excess acid can produce films having residual stress. From ICP analyses of slip supernatants and TGA of dried powders, the effect of excess acid

was an increase in $[Al^{3+}]$ in the slip. No residual stress, however, was found in the films produced from slip in which appropriate amounts of $Al(NO_3)_3$ was intentionally added to control slips to simulate excess acid conditions.

Surface characterization by FTIR and ESA measurements during potentiometric titration indicated that a surface hydroxide layer was present on the alumina surface in all the samples studied. ESCA results also indicated no surface impurities were present on the powder surface. TEM of the dried powders showed that the alumina surfaces exhibit high crystallinity. The only difference between the two powder is their shape.

The magnitude of the residual stress suggest that a small strain on the order of 1×10^{-4} may have occurred during the of drying. Shrinkages due 1 to 2 monolayer of surface hydroxyl can account for this small strain. The residual stress may also result from the constrained shrinkage behavior during drying. In either case, all the films produced in this study should contain residual stress. Microcracking is proposed to have occurred in some cases to relieve this stress. Such microcracks can be on a such a fine scale that experimental observations are not feasible. Mechanical testing of the dried green films may provide confirming evidence for this hypothesis.

In summary, the experimental results cannot confirm the exact origin of the residual stress. But the drying stress measurements suggest some differences between the two alumina powders. The difference in particle morphology may be responsible for the observed behavior.

References

1. C.D. Fredrickson, Jr., "Characterization of Hydrated Aluminas by Infrared Spectroscopy: Application to Study of Bauxite Ore," *Anal. Chem.*, **26** 1883 (1954).

2. A.J. Babchin, R.S. Chow, and R.P. Sawatzky, "Electrokinetic Measurements by Electroacoustical Methods," *Adv. Collid Interface Sci.*, **30** 111-51 (1989).

3. S. Sumita, W.E. Rhine, and H.K. Bowen, "Effects of Organic Dispersants on the Dispersion, Packing, and Sintering of Al_2O_3," Submitted to *J. Am. Ceram. Soc.*.

4. A.V. Uvarov, "Infra-red Investigation of the Interaction between Water and an Aluminum Oxide Surface," *Russ. J. Phys. Chem.*, **36** [6] 717-719 (1962).

5. C.D. Wagner *et al.*, **Handbook of X-ray Photoelectron Spectroscopy**. Perkin Elmer Corp. Pub., 1979.

6. B.A. Hendriksen, *J. Catalysis*, **24** 82 (1972).

7. C. Morterra *et al.*, *J. Chem. Soc., Far. Trans. I*, **72** 2722 (1976).

8. G.A. Parks, "The Isoelectric Points of Solid Oxides, Solid Hydroxides, and Aqueous Hydroxo Complex Systems," *Chem. Rev.*, **65** 177-98 (1965).

9. K. Wefers and C. Misra, "Oxides and Hydroxides of Aluminum," ALCOA Technical Paper No. 19, Revised ALCOA Laboratories, 1987.

10. K. Kendall, N. Mc N. Alford, and J.D. Birchall, "A New Method for Measuring the Surface Energy of Solids," *Nature*, **325** [26] 794-95 (1987).

11. K.Yamanaka, C.K. Jen, C. Neron, and J.F. Bussiere, "Improved Ultrasonic Evaluation of Green-state Ceramics with the Use of a Surface-Bonded Adhesive Tape," *Mat. Evaluation* **47** 828-834 (1989).

12. J.J. Gruber, J.M. Smith, and R.H. Brockelman, "Ultrasonic Velocity C-Scans for Ceramic and Composite Material Characterization," *Mat. Evaluation* **46** 90-96 (1988).

CHAPTER 6

CONCLUSIONS AND FUTURE WORK

The drying behavior of binder-free granular films was studied to gain a better understanding of the physical mechanisms leading to defect formation during drying. The processing parameters that affect the tendency toward cracking were identified, and the magnitude of drying stress was measured *in-situ* during drying. These results also provided quantitative estimates for the green strength of granular films. The important results are stated below.

(1) The thickness variation in the dried green films is due to the contact angle that the supersaturated slip makes with the substrate. This variation can be reduced by adding a surfactant to the slip lowering the contact angle and/or allowing the particles to settle prior to drying.

(2) The importance of five processing variables was studied using statistical experimental design. The processing parameters that significantly affect the tendency toward cracking (critical cracking thickness) were found to be particle size, effect of the electrostatic repulsive layer, and sedimentation time.

(3) The effect of substrate constraint was studied by producing films on glass, teflon, and a pool of mercury. The films produced on teflon warped and decohered from the substrate. Films as thick as 2 mm did not crack during drying when cast onto a pool of mercury. This result illustrates the benefit of

nonconstraining substrates for drying granular ceramic green films or sheets.

(4) The *in-situ* stress measurements indicated that the drying stress is due to the capillary tension in the pore liquid. The magnitude of the drying stress is as high as 2 MPa for films produced from 0.4 μm particles. Due to the capillary origin, the drying stress is lowered when the particle size is increased and/or the liquid surface tension is decreased.

(5) Cracking in the granular films typically occurred just below 100% saturation. Theoretical estimates showed that the magnitude of the drying stress is sufficiently large to collapse the dispersed particles in the green films prior to pores emptying. This suggests that the small shrinkages which are typically observed during the drying of granular bodies should occur near 100% saturation. Therefore, cracking in the films occurred as soon as shrinkages stop, similar to that in clay and gel bodies.

(6) The green strength of the granular films studied were estimated to have fracture toughness values on the order of 10^{-2} MPa-$m^{1/2}$. The relative magnitude of the green strength is proportional to the interfacial energy of the granular material.

(7) Residual stress was found to remain in films produced from AKP30 and AKP15 alumina. The magnitude of the residual stress (0.2 - 0.4 MPa) suggests that a residual shrinkage on the order of 10^{-4} in the green film occurred toward the end of drying. This residual stress may be an effect of the particle morphology. Furthermore, all the green films produced in this study dried with residual stresses; microcracking, however, may be responsible for relieving these stresses in some of the green films.

The experimental work here also indicated areas where future research would be helpful in exploring the next level of complexity in our understanding of defect formation in granular ceramic bodies during drying:

(1) The results in this study suggest that shrinkage in a granular body should occur near 100% saturation. An *in-situ* thickness measurement during drying of the granular films will provide details on the shrinkage behavior which can provide further understanding on the cracking mechanism.

(2) The experimental procedures developed in this study can be used to quantitatively evaluate the amount of strengthening organic binders provide for granular green bodies. This method will only work, however, when the volume fraction of binder is small enough so as not to affect the drying characteristics of the granular body.

(3) The results suggest that cracking in granular ceramic bodies occurs near 100% saturation just after shrinkages cease. Hence, there is a very narrow processing window for successful drying operations. Consequently, good control of the drying environment is mandatory in designing a successful drying schedule.

(4) Drying defects are difficult to detect in a green body. These defects, however, are easy to identify in sintering experiments. For instance, packing voids in a dried green films will become large pores during sintering. The effect also can be observed in sintering shrinkages and sintered densities. These results may provide a better understanding of the nature of drying defects. Sintering experiments also may be helpful to further investigate residual stresses in dried green films. For example, if microcracking had occurred in films to relieve the residual stress,

sintering characteristics would differ between films with and without residual stresses.

(5) Although the linear elastic fracture mechanics approach used in this study provided good relative measure of green strengths in granular bodies, the shortcomings of this approach was illustrated by the inconsistency between experimentally observed and calculated defect sizes. This suggests that a more complex fracture mechanics model, which takes into consideration all the physical characteristics of granular materials (granular particle packing, size, size distribution, and morphology), may be necessary to completely describe the mechanical behavior of granular materials.

Appendix 1

Image Processing Program for Diffraction Rings

This program was design to automate the tedious process of counting and measuring the relative positions of the optical diffraction rings in the stress measurements. The computer codes is written in C by Jared Wunsch. The main program to be aware of is called "FTRINGS." The rings were identified by the differences in pixel intensities. FTRINGS scans at a specified time intervals between two specified points on the video screeen. The program then smooths the data using a fourier-transform method prior to selecting the brightness minima as the position of the diffraction rings.

FTRINGS prompts the user for several sets of information. First, it requests the name of the data file to generate. The user is then asked to calibrate the distance between two points on the screen. Next, the user has to define the two points between which the program will scan for diffraction rings and the time interval for data collection. Lastly, the user has to select the smoothing factor and the parameter which is the minimum difference in brightness levels that one require between bightness maxima and minima. I recommend a value of 4 for both parameters.

The main part of the program is listed in "ftrings.c." Other modules are plot.c, min.c, ringstuff.c, and msefns.c. The subroutines for data smoothing is taken from Numerical Recipes in C [1], which include four1.obj, realt.obj, and smooft.obj. The source codes are listed in the following pages.

References

1. W.H. Press, B.P. Flannery, S.A. Teukolsky, and W.T. Vetterling, **Numerical Recipes in C: The Art of Scientific Computing**, Cambridge Univerity Press, New York, 1988.

Ftrings.C

```
/*  FTRINGS - a program to evaluate diffraction rings using the DT2851
        frame grabber.  version 1.00

        Copyright Jared Wunsch 1990                    */


#include "diffract.h"

main() {

FILE *fp;
int error, err;
int row, col, i, j, k, minno, temp, c, diff;
int array[1000];
float ftarray[2000];
int len;
int row1, row2, col1, col2;
float length, a, min[200];  /* sets aside space for 200 minima */
float r_length;  /* real length of measuring interval, calculated from
                                                    user-inputed calibration */
float pts;
float r_min;
time_t tme, t0, told;
long int timeint;
long int hours, minutes, seconds, total;
char d;
int pauseflag, mouseflag;
float (* cal)( void );
int (* end)( int *, int *, int *, int * );

mouseflag = chkdrv();
if (mouseflag == 1)
        {
        cal = mouse_get_calibration;
        end = mouse_get_endpoints;
        }
else
        {
        cal = get_calibration;
        end = get_endpoints;
        }
fp = get_file();

is_initialize();

if (( error = get_frame( 0 ) ) != 0)
        {
        printf("Error getting frame!!\n\n");
        exit(0);
        }

is_display(1);
```

```
is_select_output_frame(0);

while ( ( a=(*cal)() ) == -1)
        {
        printf("Calibration error!\n hit any key to continue...\n");
        while (!kbhit());
        getch();
        _clearscreen(_GCLEARSCREEN);
        }

while (err = (*end)( &row1, &col1, &row2, &col2 ) != 0)
        {
        printf("Error in setting endpoints!\n hit any key to continue...\n");
        while (!kbhit());
        getch();
        _clearscreen(_GCLEARSCREEN);
        }

length =  (float) sqrt( pow((double) (row2-row1),2) + pow((double) (col2-col1),2) );
/* "length" is length in units of # of pixels - gives a reasonable number
        of pixels to acquire even when direction isn't horizontal or vertical */

r_length = a * ((float) sqrt( 0.64 * pow((double) (row2-row1),2) + pow((double) (col2-col1),2) ));
/* gives length in units of user-specified length */

len = (int) length;

_clearscreen(_GCLEARSCREEN);

printf("\nInput the window-size parameter for the smoothing function.\n(the parameter needn't be a
whole number.)\n\n");
while (scanf("%f", &pts) != 1)
        {
        fflush(stdin);
        printf("Input error.  Please try again.\n\n");
        }

printf("\nInput the required brightness difference between maxima and minima.\n(an integer value
between 1 and 10 is suggested.)\n\n");
while (scanf("%i", &diff) != 1)
        {
        fflush(stdin);
        printf("Input error.  Please try again.\n\n");
        }

_clearscreen(_GCLEARSCREEN);

printf("\nInput time interval in seconds.\n\n");
while ( scanf("%li", &timeint) != 1 || timeint < 1 || timeint > 100000)
        {
        fflush(stdin);
        printf("Input error.  Please try again.\n\n");
        }
```

```
printf("\nInput length of time for which to measure (format is hours:minutes:seconds).\n\n");
while ( scanf("%li:%li:%li", &hours, &minutes, &seconds) != 3 )
        {
        fflush(stdin);
        printf("Input error.  Please try again.\n");
        }

total = hours * 3600 + minutes * 60 + seconds;

_clearscreen(_GCLEARSCREEN);

printf("\nPause 1 sec after graphing? (y/n)\n");
while ( (d=getch()) != 'y' && d != 'Y' && d != 'n' && d != 'N');
        {
        fflush(stdin);
        printf("Input error.  Please try again.\n");
        }

if ( d == 'y' || d == 'Y' )
        pauseflag = 1;
else
        pauseflag = 0;

_clearscreen(_GCLEARSCREEN);

printf("\n\nHit any key to start program execution.\n\n");
while (!kbhit());
getch();
printf("\nProgram running.\n\n");

told = time( &t0 );
while ( time(&tme) <= t0 + total )
        {
        if ( (time(&tme)) >= told + timeint )
                {
                told = tme;

                fprintf( fp, "%li ", tme - t0 );

                if (( error = get_frame( 0 ) ) != 0)
                        {
                        printf("Error getting frame!!\n\n");
                        exit(0);
                        }

                for (i=0; i<len; i++)
                        {
                        error = is_get_pixel( 0, row1 + (int) ( i*((row2-row1)/length) ), col1 +
(int) ( i*((col2-col1)/length)), 1, array + i);
                        if (error != 0)
                                {
                                _clearscreen(_GCLEARSCREEN);
                                printf("Error # %i getting pixel.\n\n",error);
                                exit(0);
```

```
                        }
                }

        for (i=0; i<len; i++)
                {
                bright[i] = array[i];
                ftarray[i] = (float) array[i];
                }

        if (error != 0)
                printf("\a\a\a\nAn error has occurred!!!\n\n\n");

        for(k=0; k<len; k++)
                xaxis[k] = r_length * ( ((float) k)/((float) len) );

        if ((k = plot(len)) != 1)
                {
                _setvideomode(_DEFAULTMODE);
                printf("plot routine failed\n");
                }

        if (pauseflag == 1)
                wait((short) 1);

        smooft(ftarray, len, pts);
        for (i=0; i<len; i++)
                bright[i] = ftarray[i];

        if ((k = plot(len)) != 1)
                {
                _setvideomode(_DEFAULTMODE);
                printf("plot routine failed.\n");
                }

        if (pauseflag == 1)
                wait((short) 1);

        minno = minimize( ftarray, len, min, diff);
        _setvideomode(_DEFAULTMODE);
        printf( "minima occur at:\n\n" );

        for (j=0; j<minno; j++)
                {
                r_min = (r_length * min[j])/((float) len);
                printf( "%f\n", r_min );
                fprintf( fp, "%f ", r_min );
                }
        fprintf( fp, "\n" );

        }
}

is_end();
fclose( fp );
```

```
}
```

Diffract.h

```
#include <graph.h>
#include <pgchart.h>
#include <stdio.h>
#include <math.h>
#include <time.h>
#include <dos.h>

#include <isdefs.c>
#include <nr.h>

#define MOUSE 0x33

#define _ENTER 0xD

/* the following are preceded by NULL */
#define _UP 0x48
#define _DOWN 0x50
#define _LEFT 0x4B
#define _RIGHT 0x4D

float _far bright[1000];    /* need far arrays for presentation graphics */
float _far xaxis[1000];     /* routines                                  */

int plot(unsigned int length);
int minimize(float *data, int length, float *min, int diff);
float get_calibration(void);
float mouse_get_calibration(void);
void get_point(int *row, int *col);
FILE *get_file(void);
int get_endpoints(int *row1, int *col1, int *row2, int *col2);
int mouse_get_endpoints(int *row1, int *col1, int *row2, int *col2);
int get_frame(int buffer);
int restore_test_frame(int buffer);
void wait(int tm);
int put_cross( int row, int col, int rsize, int csize, int buffer);
int chkdrv( void );
void mouse_get_point( int *r, int *c );
```

Plot.C

```
/* ------------------------------------------------------ */

#include "diffract.h"

int plot(unsigned int length) {

palettetype palette_struct;
chartenv env;
int mode = _VRES16COLOR;
int i,k;


/* now, graph it */
_setvideomode(mode);
_pg_initchart();
_pg_getpalette( palette_struct );
palette_struct[1].plotchar='.';
_pg_setpalette( palette_struct );
_pg_defaultchart( &env, _PG_SCATTERCHART, _PG_POINTONLY);

if(_pg_chartscatter(&env, xaxis, bright, (short) length))
        {
        _setvideomode(_DEFAULTMODE);
        _outtext("Error: can't draw chart.\n\n");
        return(0);
        }
else
        {
        return(1);
        }
}
```

Min.C

```
/* ---------------------------------------------------------- */

#include "diffract.h"

int minimize(float *data, int length, float *min, int diff) {

/* finds relative minima of the string "data," (whose length is "length")
and outputs these minima in the string "min."  The number of relative minima
recorded is given by the return value.                          */

int pixel, first, i;
float bnew, bold, max, mn;

first = 0;
pixel = 0;
i=0;
max=512;
mn=0;

while (pixel < length -1 && i < 190)   /* allow only 190 minima */
        {
        for ( ; (bold=data[pixel]) >= (bnew=data[pixel+1]) && pixel < length - 1; pixel++ )
                {
                if (bold == bnew && first == -1)
                        first = pixel - 1;
                if (bold != bnew)
                        first = -1;
                }

        if (pixel < length - 1)
                {
                if ( first != 0 && bold <= max - diff )
                /* diff is a fudge-factor to prevent interpreting noise as minima.
                        Note also that a minimum or flat spot occurs exactly at the
                        beginning of the interval, it will be discarded, since we
                        can't be sure it's really a minimum                     */

                        {
                        if (first == -1)
                                {
                                min[i] = (float) (pixel - 1);
                                i++;
                                }
                        else
                                {
                                min[i] = ( (float) pixel - 1 + (float) first )/2;
                                i++;
                                }
                        }
                }

        for ( ; (bold=data[pixel])<=(data[pixel+1]) && pixel<length-1; pixel++)
```

```
                ;
        if (bold >= mn + diff)
                max=bold;


        }

return(i);

}
```

Ringstuf.C

```
#include "diffract.h"

/* ------------------------------------------------------------ */

float get_calibration(void) {

int row1, col1, row2, col2;
float dist, rowdist, coldist, factor;

_clearscreen(_GCLEARSCREEN);
printf("Make sure number lock is off!\n\n");
printf("Manipulate cursor using arrow keys, and shift key.\n\n");

printf("Select first calibration point on output screen:\n hit <CR> when ready.\n\n");

get_point( &row1, &col1 );

_clearscreen(_GCLEARSCREEN);
printf("Select second calibration point on output screen:\n hit <CR> when ready.\n\n");

get_point( &row2, &col2 );

_clearscreen(_GCLEARSCREEN);

printf("Input distance between two points.\n\n");
while (scanf("%f", &dist) != 1)
        {
        fflush(stdin);
        printf("No good.  Try again.\n");
        }

if (dist <= 0)
        {
        printf("Error: distance can't be negative or zero.\n\n");
        return( -1 );
        }

rowdist = (float) abs( row2 - row1 );
coldist = (float) abs( col2 - col1 );

if ( rowdist==0 && coldist==0 )
        {
        printf("Error: you must move the cursor a nonzero distance.\n");
        return( -1 );
        }

factor = sqrt(pow(dist,2)/(0.64 * pow(rowdist,2) + pow(coldist,2)));
/*
        This "factor" is the ratio of (distance in the x direction) to (# of pixels
        difference in the x-direction).  The 0.64 comes from the 5/4 ratio in the
        xlength of a pixel to the ylength of a pixel.
*/
```

```
return(factor);
}

/* ------------------------------------------------------------ */

int get_endpoints( int *r1, int *c1, int *r2, int *c2 ) {

_clearscreen(_GCLEARSCREEN);
printf("Set first endpoint with arrow and shift keys.\n  Hit return when you're satisfied.\n\n");
printf("(Make sure num lock is off!!)\n\n");

get_point(r1, c1);

_clearscreen(_GCLEARSCREEN);

printf("Now set second endpoint.\n\n");

get_point(r2, c2);

if (r1==r2 && c1==c2)
        return( -1 );
else
        return( 0 );
}

/* ------------------------------------------------------------ */

void get_point( int *rowptr, int *colptr) {

struct rccoord pos;
char c;

is_cursor(1);

pos = _gettextposition();
is_report_cursor_position( rowptr, colptr );
_settextposition( 20, 5 );
printf("row = %i,  column = %i\n",*rowptr,*colptr);

while ((c = getch()) != _ENTER)
        {
        if ( c == 0 )
                c = getch();

        switch(c)
                {
                case '8':
                        *rowptr -= 30;
                        break;
                case '2':
                        *rowptr += 30;
                        break;
                case '4':
                        *colptr -= 30;
```

```
                        break;
                case '6':
                        *colptr += 30;
                        break;
                case 0x48:
                        *rowptr -= 1;
                        break;
                case 0x50:
                        *rowptr += 1;
                        break;
                case 0x4b:
                        *colptr -= 1;
                        break;
                case 0x4d:
                        *colptr += 1;
                        break;
                case 0xd:
                        break;
                default:
                        printf("\a");
                        break;
                }

        is_set_cursor_position( *rowptr, *colptr );
        _settextposition(  20, 5 );
        printf("row = %i,  column = %i\n",*rowptr,*colptr);
        }
        _settextposition( pos.row, pos.col );
}

/*  ------------------------------------------------------- */

int get_frame( int buffer ) {

int err1, err2;

err1 = is_set_sync_source(1);
err2 = is_acquire(buffer,1);

if (err1 != 0 || err2 != 0)
        return(-1);
else
        return(0);

}

/* ------------------------------------------------------------ */

int restore_test_frame( int buffer ) {

int err1, err2;

err1 = is_set_sync_source( 0 );
err2 = is_restore(buffer,0,0,"c:\\frame\\images\\rings3.img");
```

```
if (err1 != 0 || err2 != 0)
        return(-1);
else
        return(0);

}

/* ------------------------------------------------------ */

FILE *get_file( void ) {

char c, filename[30];
char *filerr;
FILE *ptr;

filerr = "Enter filename for data output.\n\n";

_clearscreen(_GCLEARSCREEN);

while (filerr != NULL)
        {
        printf( filerr );

        filerr = NULL;

        if (gets(filename) == NULL)
                filerr = "\nError reading string.\n Please try again.\n\n";

        else if (access(filename,0)==0)
                {
                printf("\nFile exists!!  Overwrite? (y/n)\n\n");
                while ((c = getch()) != 'y' && c != 'Y' && c != 'n' && c != 'N')
                        printf("\a");
                if (c == 'y' || c == 'Y')
                        filerr = NULL;
                if (c == 'n' || c == 'N')
                        filerr = "\nPlease enter new filename\n\n";
                }

        if ((ptr=fopen(filename,"w"))==NULL)
                {
                filerr = "\nUnable to open file.\n Please enter new filename.\n\n";
                }
        }
return(ptr);
}

/* ------------------------------------------------------ */

void wait( int t ) {

time_t t0, t1;

time(&t0);
```

```
while (time(&t1) <= t0 + (time_t) t)
        ;
}


/* ------------------------------------------------------------ */

int put_cross( int row, int col, int rsize, int csize, int buffer) {

int e1, e2, e3, e4;
int ptarray[2];

ptarray[0] = row+rsize;
ptarray[1] = col;
e1 = is_set_graphic_position( row - rsize, col );
e2 = is_draw_lines( buffer, 1, ptarray );
ptarray[0] = row;
ptarray[1] = col + csize;
e3 = is_set_graphic_position( row, col - csize );
e4 = is_draw_lines( buffer, 1, ptarray );

if (e1==0 || e2==0 || e3==0 || e4==0)
        return(-1);
else
        return(0);
}

/* ------------------------------------------------------------ */

float mouse_get_calibration(void) {

int row1, col1, row2, col2;
float dist, rowdist, coldist, factor;

_setvideomode(_VRES16COLOR);
printf("Manipulate cursor using trackball.\n");
printf("Holding down left button speeds trackball motion.\n\n");

printf("Select first calibration point on output screen:\n hit right or center trackball button when
ready.\n\n");

mouse_get_point( &row1, &col1 );

_clearscreen(_GCLEARSCREEN);
printf("Select second calibration point on output screen:\n hit right or center trackball button when
ready.\n\n");

mouse_get_point( &row2, &col2 );

_clearscreen(_GCLEARSCREEN);

printf("Input distance between two points.\n\n");
while (scanf("%f", &dist) != 1)
        {
```

```
        fflush(stdin);
        printf("No good.  Try again.\n");
        }

if (dist <= 0)
        {
        _setvideomode(_DEFAULTMODE);
        return( -1 );
        }

rowdist = (float) abs( row2 - row1 );
coldist = (float) abs( col2 - col1 );

if ( rowdist==0 && coldist==0 )
        {
        _setvideomode(_DEFAULTMODE);
        return( -1 );
        }

factor = sqrt(pow(dist,2)/(0.64 * pow(rowdist,2) + pow(coldist,2)));
/*
        This "factor" is the ratio of (distance in the x direction) to (# of pixels
        difference in the x-direction).  The 0.64 comes from the 5/4 ratio in the
        xlength of a pixel to the ylength of a pixel.
*/
_setvideomode(_DEFAULTMODE);
return(factor);
}


/* ------------------------------------------------------- */

int mouse_get_endpoints( int *r1, int *c1, int *r2, int *c2 ){

_setvideomode(_VRES16COLOR);
printf("Set first endpoint with trackball.\n  Hit center or right button when you're satisfied.\n\n");

mouse_get_point(r1, c1);

_clearscreen(_GCLEARSCREEN);

printf("Now set second endpoint.\n\n");

mouse_get_point(r2, c2);

if (r1==r2 && c1==c2)
        {
        _setvideomode(_DEFAULTMODE);
        return( -1 );
        }
else
        {
        _setvideomode(_DEFAULTMODE);
        return( 0 );
```

```
        }
}
/* ---------------------------------------------------------- */
```

Msefns.C

```
#include "diffract.h"


/* CHKDRV returns 1 if mouse driver installed, 0 if not */

int chkdrv ()
{
        union REGS inregs, outregs;
        struct SREGS segregs;
        unsigned long address;
        unsigned char first_byte;

        inregs.x.ax = 0x3533;           /* Get interrupt vector for 0x33 */
        intdosx ( &inregs, &outregs, &segregs);
        address = (((long) segregs.es) << 16) + (long) outregs.x.bx ;
        first_byte = (unsigned char) * (long far *) address;

        /* Be sure vector isn't 0 and first instruction isn't iret */
        if ((address == 0L) || (first_byte == 0xCF))
                return(0);
        else
                return(1);
}

/* Note: the following function only works in graphics mode */

void mouse_get_point( int *rowptr, int *colptr ) {

struct rccoord pos;
unsigned short m1, m2, m3, m4, a1, sen1, sen2, threshold;
int fast = 0;
sen1 = 1;
sen2 = 40;
threshold = 20;
a1 = 26;

is_cursor(1);

/* set mouse sensitivity */
cmousel( &a1, &sen1, &sen1, &threshold );

        /*  Set Vertical Limits  */
        m1 = 7;
        m3 = 0;
        m4 = 511;
        cmousel ( &m1, &m2, &m3, &m4);

        /*  Set Horizontal Limits  */
        m1 = 8;
        m3 = 0;
        m4 = 479;
        cmousel ( &m1, &m2, &m3, &m4);
```

```
pos = _gettextposition();
is_report_cursor_position( rowptr, colptr );

        do
        {
                m1 = 3;
                a1 = 26;
                cmousel ( &m1, &m2, colptr, rowptr);
                is_set_cursor_position( *rowptr, *colptr );
                _settextposition ( 20, 5 );
                printf ("row = %i,  column = %i   \n", *rowptr, *colptr);
                if ( m2 == 1 && fast == 0 )
                        {
                        cmousel( &a1, &sen2, &sen2, &threshold );
                        fast = 1;
                        }
                else if ( m2 != 1 && fast == 1 )
                        {
                        cmousei( &a1, &sen1, &sen1, &threshold );
                        fast = 0;
                        }
        } while (m2 != 2 && m2 != 3);  /*  Loop until button pressed  */

}
```